Multiple Covers with Balls

by

Mabel Iglesias Ham

June, 2018

A thesis presented to the
Graduate School
of the
Institute of Science and Technology Austria, Klosterneuburg, Austria
in partial fulfillment of the requirements
for the degree of
Doctor of Philosophy

The thesis of Mabel Iglesias Ham, titled *Multiple Covers with Balls*, is approved by:

Supervisor: Herbert Edelsbrunner, IST Austria, Klosterneuburg, Austria

Signature: _____

Committee Member: Uli Wagner, IST Austria, Klosterneuburg, Austria

Signature: _____

Committee Member: Mohammad Saadatfar, ANU, Canberra, Australia

Signature: _____

Defense Chair: Chris Wojtan, IST Austria, Klosterneuburg, Austria

Signature: _____

I hereby declare that this thesis is my own work and that it does not contain other people's work without this being so stated; this thesis does not contain my previous work without this being stated, and the bibliography contains all the literature that I used in writing the dissertation.

I declare that this is a true copy of my thesis, including any final revisions, as approved by my thesis committee, and that this thesis has not been submitted for a higher degree to any other university or institution.

I certify that any republication of materials presented in this thesis has been approved by the relevant publishers and co-authors.

Signature: _____

Mabel Iglesias Ham
June, 2018

Abstract

We describe arrangements of three-dimensional spheres from a geometrical and topological point of view. Real data (fitting this setup) often consist of soft spheres which show certain degree of deformation while strongly packing against each other. In this context, we answer the following questions: If we model a soft packing of spheres by hard spheres that are allowed to overlap, can we measure the volume in the overlapped areas? Can we be more specific about the overlap volume, i.e. quantify how much volume is there covered exactly twice, three times, or k times? What would be a good optimization criteria that rule the arrangement of soft spheres while making a *good* use of the available space? Fixing a particular criterion, what would be the optimal sphere configuration?

The first result of this thesis are short formulas for the computation of volumes covered by at least k of the balls. The formulas exploit information contained in the order-k Voronoi diagrams and its closely related Level-k complex. The used complexes lead to a natural generalization into *poset diagrams*, a theoretical formalism that contains the order-k and degree-k diagrams as special cases. In parallel, we define different criteria to determine what could be considered an optimal arrangement from a geometrical point of view. Fixing a criterion, we find optimal soft packing configurations in 2D and 3D where the ball centers lie on a lattice. As a last step, we use tools from computational topology on real physical data, to show the potentials of higher-order diagrams in the description of melting crystals. The results of the experiments leaves us with an open window to apply the theories developed in this thesis in real applications.

Acknowledgments

I would like to thank IST Austria and its Grad School for providing the conditions for this thesis to be developed. Special thanks to my supervisor Herbert Edelsbrunner, for trusting me and accepting me in his group, for the many hours of motivating research discussions and guidance that contributed to my professional development, for the opportunity to see at close distance his talent and learn from his academic example, and for the pleasure to meet him as an extraordinary person. Likewise, I am very grateful to his well selected group members, old and new, which contributed to a pleasant working environment and fruitful seminars. Furthermore, I thank my mother, Jacqueline, for taking care of my sweet daughter Sophia while I finish my thesis, and to my loving partner Michael for his support, fruitful discussions and encouragement.

About the Author

Mabel Iglesias Ham completed the MSc in Computer Science at University of Havanna, Cuba, in 2005. From 2005 to 2011 she joined the Pattern Recognition Department at the Advanced Technologies Application Center (CENATAV), Cuba, where she became Associate Researcher. During this period she collaborated as Research Assistant with the Pattern Recognition and Image Processing Group (PRIP) at Vienna University of Technology, in 2008 and 2009. She contributed to theoretical and applied projects in the areas of Fingerprint, Palmprint, Video Surveillance and Homology/Cohomology generators in images. In September 2012 she joined the Grad School Program at the Institute of Science and Technology, IST Austria, and in 2013 joined the Algorithms, Computational Geometry and Topology Group. Her PhD research has focused on theoretical results in the area of Soft Sphere Packings, Voronoi diagrams and k-fold volume computations. Additionally, she has used tools from computational topology to describe the potentials of the developed theory in applications.

List of Publications

1. Herbert Edelsbrunner and Mabel Iglesias-Ham: On the Optimality of the FCC Lattice for Soft Sphere Packing. SIAM Journal on Discrete Mathematics, vol. 32 (1), pp. 750-782, 2018.

2. Herbert Edelsbrunner and Mabel Iglesias-Ham: Multiple Covers with Balls II: Weighted Averages. Electronic Notes in Discrete Mathematics, vol. 54, pp.169-174, 2016.

3. Herbert Edelsbrunner, Mabel Iglesias-Ham and Vitaliy Kurlin: Relaxed Disk Packing. Proceedings of the 27th Canadian Conference on Computational Geometry, pp. 128-135, CCCG 2015.

4. Herbert Edelsbrunner and Mabel Iglesias-Ham: Multiple Covers with Balls I: Inclusion-Exclusion. Special Issue in Memoriam: Ferran Hurtado, Journal of Computational Geometry: Theory and Applications, vol. 68, pp.119-133, 2018.

5. Mabel Iglesias-Ham, Michael Kerber and Caroline Uhler: Sphere Packing with Limited Overlap. Proceedings of the 26th Canadian Conference on Computational Geometry, pp. 155-161, CCCG 2014.

Table of Contents

List of Tables

List of Figures

List of Abbreviations

SCD Spherical 1 Mega-base-pairs Chromatin Domain

FCC Face-centered cubic

BCC Body-centered cubic

HCP Hexagonal close-packed

WC Weighted circumcenter

WKC Weighted k-folds circumcenter

1 Introduction

The motivation of this thesis comes from modeling in the biological sciences. High-resolution microscopic observations of the DNA organization inside the nucleus of a human cell support the *Spherical Mega-base-pairs Chromatin Domain model* (SCD) [Cremer *et al.*, 2000; Kreth *et al.*, 2001]. It proposes that inside the chromosome territories of eukaryotic cells, DNA is compartmentalized into sequences of highly interacting segments of about the same length [Dixon *et al.*, 2012]. Each segment consists of roughly a million base pairs and is rolled up to resemble a round ball. The balls are tightly arranged within the available space, tighter than a packing since the balls deform when pressed against each other, and less tight than a covering so that protein machines can find access to the DNA needed for gene expression and replication. These models result in overlapping spheres which do not fill the whole space. Other examples are the spatial organization of chromosomes in the cell nucleus [Cremer and Cremer, 2010; Uhler and Wright., 2013], the spatial organization of neurons [Raj and Chen, 2011; Rivera-Alba *et al.*, 2011], or the arrangement of ganglion cell receptive fields on the retinal surface [DeVries and Baylor, 1997; Karklin and Simoncelli, 2011].

The density of an arrangement of balls can be computed as the sum of its volumes divided by the volume of the container. The traditional packing problem aims for an arrangement of equal size balls that maximizes its density while no overlap is allowed. On the other hand, the covering problem aims for an arrangement of overlapping balls that covers the whole space while minimizing its density. We refer to the book by Conway and Sloane [Conway and Sloane, 1999], for a representative text in the rich mathematical literature on the traditional packings and coverings with balls. In this thesis we consider configurations that lie between these two extremes: the balls are allowed to overlap and they do not necessarily cover the entire space; see also

[Schürmann and Vallentin, 2006]. The mentioned models in biology lie in this *relaxed packing* or *soft packing* category. The wide applicability is also based on the fact that soft spheres can be modeled as hard spheres with limited overlap.

Given a soft packing configuration, we are interested in quantifications. For packings and coverings, it is customary to compute the *density*, which is the expected number of balls that contain a random point. This measure can also be used for more general configurations. Alternatively, we may be interested in the set of points each covered by exactly one ball; its volume is the difference between the volume of the union and of the 2-fold cover of the balls. It requires the ability to measure the set of points covered by at least two balls, which is a special case of the question addressed in Chapter 2 of this thesis. In short, we provide formulas to compute the volume covered by at least k of the balls.

Closely related to this question are the concepts of order-k and degree-k Voronoi diagrams, as well as its dual structures. Consider a set of sites or ball centers in $\mathbb{R}^n$. Intuitively, the order-k Voronoi diagram partitions the space into regions such that every point inside one region has the same k closest neighbors. The degree-k diagram can be obtained by subdividing the order-k regions depending on which of its k balls maximizes the distance. In Chapter 3, we introduce a generalization to *poset diagrams* and *poset complexes*, which contain such diagrams as special cases. Extending a result of Aurenhammer from 1990 [Aurenhammer, 1990], we show how to construct them as weighted Voronoi diagrams of average balls.

In Chapter 4, we address the *soft packing* problem considering a couple of the many possible optimality approaches. First, we maximize the density while using a threshold to control the amount of allowed overlap in Section 4.2. Next, we expand on a non-parameterized setting by maximizing the area covered exactly once in Section 4.3. The previous measure can be understood as the probability of a random point to be covered exactly once. Maximizing given probability naturally favors configurations lying between the traditional packing and covering problems. In Section 4.4 we extend to 3D but using a variation of the previous measure. The optimal lattice is found to maximize a soft density function which penalizes multiple overlaps. Additionally, in Chapter 5 we use experimental tools from Computational Topology and data from physics to test the potential uses of the theories developed in this thesis. Final considerations are

summarized in Chapter 6.

Main contributions. A summary of the main contributions of the thesis is listed here.

1. Two short inclusion-exclusion formulas for the volume in $\mathbb{R}^n$ covered by at least k balls in a finite set [Edelsbrunner and Iglesias-Ham, 2018a].

2. A generalization of Voronoi diagrams to *poset diagrams*, which contain order-k and degree-k Voronoi diagrams as special cases [Edelsbrunner and Iglesias-Ham, 2016].

3. Proposal of two overlap measures to find within the 1-parameter family of lattices, the optimal soft packings while limiting the amount of overlap by a threshold [Iglesias-Ham *et al.*, 2014].

4. Proof that among all lattice configurations in $\mathbb{R}^2$, the regular hexagonal grid maximizes the probability that a random point lies in exactly one disc [Edelsbrunner *et al.*, 2015] .

5. Proof that within the 1-parameter family of lattices in $\mathbb{R}^3$, the FCC lattice maximizes a soft density measure, which penalizes multiple overlaps [Edelsbrunner and Iglesias-Ham, 2018b].

6. First steps in the description of relevant information stored in higher-order Voronoi diagrams using Persistence Homology.

2 Inclusion-Exclusion

Inclusion-exclusion is an effective method for computing the volume of a union of measurable sets. In this chapter we present its extension to multiple coverings, proving short inclusion-exclusion formulas for the subset of $\mathbb{R}^n$ covered by at least k balls in a finite set. We implement two of the formulas in dimension $n = 3$ and report on results obtained with our software.

2.1 Prior work and results

An effective method for computing the volume of a union of balls, or possibly more general sets, is the principle of inclusion-exclusion. It has a long history in mathematics and is attributed to Abraham de Moivre (1667–1754) but appeared first in writings of Daniel da Silva (1854) and of James Joseph Sylvester (1883). Given a finite collection of measurable sets, $\mathcal{X}$, in $\mathbb{R}^n$, it asserts that the volume of the union is the alternating sum of the volumes of the common intersections of the sets in all subcollections $Q \subseteq \mathcal{X}$. The formula can be generalized to *k-fold covers*, which we define as the set $\mathbb{X}_k$ of points in $\mathbb{R}^n$ that belong to at least k of the sets:

$$\mathrm{vol}[\mathbb{X}_k] = \sum_{i \geq k} (-1)^{i-k} \binom{i-1}{k-1} \sum_{Q \in \binom{\mathcal{X}}{i}} \mathrm{vol}[\bigcap Q]; \tag{2.1}$$

in which $\binom{\mathcal{X}}{i}$ denotes the collection of subsets of size i, see for example Chapter IV of Feller's textbook on probability [Feller, 1968, page 110]. Since we need (2.1) in the proofs of the short inclusion-exclusion formulas, we give our own proof using the Pascal triangle and its alternating form. If the measurable sets are balls, we write $\mathcal{B}$ for the collection, and $\mathbb{B}_k$ for the k-fold cover. Using the power distance of a point to a ball, the *order-k Voronoi diagram* identifies all collections $Q \subseteq \mathcal{B}$ of size k for which there

are points so that the balls in Q are the k closest; see e.g. [Shamos and Hoey, 1975]. Restricting (2.1) to terms that correspond to cells of the order-k Voronoi diagram, we get a short inclusion-exclusion formula:

$$\mathrm{vol}[\mathbb{B}_k] = \sum_{\sigma \in \mathcal{V}_k} (-1)^{\mathrm{codim}\, \gamma(\sigma)} \mathrm{vol}[\bigcap Q_{\gamma(\sigma)}], \tag{2.2}$$

see the Order-k Pie Theorem in Section 2.4 for details. Every γ is a cell of the order-k Voronoi diagram, with at least k and at most $k+n$ balls in the corresponding collection $Q_\gamma \subseteq \mathcal{B}$. Relation (2.2) generalizes the inclusion-exclusion formula of Naiman and Wynn [Naiman and Wynn, 1992] from the union to more general k-fold covers. We also prove a slightly stronger version of (2.2) in which the sum ranges over the subcollection of cells that have a non-empty common intersection with the balls that define them. It generalizes the inclusion-exclusion formula based on alpha shapes given in [Edelsbrunner, 1995b]. To reduce the size of the terms, we use levels in hyperplane arrangements in $\mathbb{R}^{n+1}$ and inclusion-exclusion formulas for general polyhedra; see [Chen, 1996; Edelsbrunner, 1995a], and obtain another short inclusion-exclusion formula for the n-dimensional volume of the k-fold cover:

$$\mathrm{vol}[\mathbb{B}_k] = \sum_{Q \in \mathcal{L}_k} L_Q \cdot \mathrm{vol}[\bigcap Q]; \tag{2.3}$$

see the Level-k Pie Theorem in Section 2.5 for details. The collections $Q \subseteq \mathcal{B}$ correspond to affine subspaces of the arrangement, with size between 1 and $n+1$. For $k = 1$, the formulas (2.2) and (2.3) are the same. Importantly, we have a slightly stronger version of (2.3) in which all collections of balls are independent. Among other advantages, this additional property eliminates an otherwise necessary case analysis and thus simplifies computer implementations. As mentioned above, the short inclusion-exclusion formulas in (2.2) and (2.3) have applications in the study of the spatial organization of chromosomes. We have implemented the formulas in dimension $n = 3$, using software supporting exact arithmetic [CGAL; MAPLE] and volume formulas for the common intersection of 3-dimensional balls [Edelsbrunner and Fu, 1994].

Outline. Section 2.2 extends the principle of inclusion-exclusion from unions to k-fold covers. Section 2.3 provides background on Voronoi diagrams and hyperplane arrangements. Sections 2.4 and 2.5 prove short inclusion-exclusion formulas for k-fold covers with balls in $\mathbb{R}^n$. Section 2.6 presents results of computational experiments. Section 2.7 concludes the chapter.

2.2 Combinatorial formula

In this section, we explain how the inclusion-exclusion formula for the volume of a union of measurable sets can be extended to k-fold covers. In the context of probability theory, the same extension can be found in [Feller, 1968, page 110]. We begin with a combinatorial result on Pascal triangles.

Pascal triangles. Recall that the *Pascal triangle* is a 2-dimensional organization of the binomial coefficients, and the *alternating Pascal triangle* is the same except that the coefficients are listed with alternating sign; see Figure 2.1. We think of them as

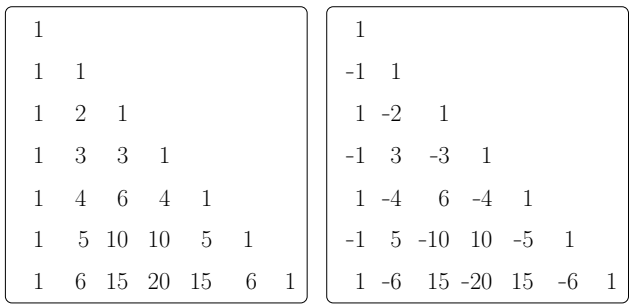

Figure 2.1: The first few non-zero rows of the Pascal triangle on the *left*, and of the alternating Pascal triangle on the *right*.

(infinitely large) matrices that can be multiplied. To talk about the product, we introduce notation for the u-th row of the Pascal triangle and the v-th column of the alternating Pascal triangle, $R_u, C_v \colon \mathbb{Z} \to \mathbb{Z}$ defined by

$$R_u(v) = \binom{u}{v}, \tag{2.4}$$

$$C_v(u) = (-1)^{u-v}\binom{u}{v}, \tag{2.5}$$

where $\binom{u}{v} = 0$ whenever $v < 0$ or $u < v$. In the Pascal triangle, each entry in the u-th row is obtained by adding two entries in the $(u-1)$-st row: $R_u(v) = R_{u-1}(v-1)+R_{u-1}(v)$, unless $u = v = 0$ in which case $R_0(0) = 1$. Similarly, in the alternating Pascal triangle, each entry of the v-th column is obtained by adding two entries in the $(v+1)$-st column: $C_v(u) = C_{v+1}(u) + C_{v+1}(u+1)$, unless $u = v = -1$ in which case $C_{-1}(-1) = 0$. Both rules can be reversed, generating a row from the next row and a column from the

previous column:

$$R_{u-1}(v) = \sum_{j\geq 0}(-1)^j R_u(v-j), \tag{2.6}$$

$$C_{v+1}(u) = \sum_{j\geq 0}(-1)^j C_v(u-j-1). \tag{2.7}$$

It is easy to prove both relations by induction, but note that (2.6) requires $u \neq 0$ or $v < 0$ and (2.7) requires $v \neq -1$ or $u < 0$. Observe that the rows of the Pascal triangle are symmetric: $R_u(v) = R_u(u-v)$ for all u and v. Accordingly, we can reverse the direction of the summation in (2.6), while the same cannot be done in (2.7).

Shifted multiplication. As usual in matrix multiplication, we define the product as the matrix whose entry in row u and column v is the scalar product of the u-th row on the left and the v-th column on the right. More generally, we introduce a *shift parameter*, $d \in \mathbb{Z}$, and define

$$M_d(u,v) = \sum_{j=-\infty}^{\infty} R_{u+d}(j) \cdot C_v(j-d). \tag{2.8}$$

For $d = 0$, this is the usual matrix product, and more generally, it is the product in which the rows of the first matrix are shifted up by d positions and the rows of the second matrix are shifted down by d positions. To get a feeling for the shifted matrix product, we fix a row u_0 in the left matrix and compute scalar products with shifted versions of all columns in the right matrix:

$$N_{u_0}(u,v) = \sum_{j=-\infty}^{\infty} R_{u_0}(j) \cdot C_v(j-u_0+u); \tag{2.9}$$

see Figure 2.2 which shows the result for $u_0 = 4$. Note that row R_{u_0} has $u_0 + 1$ non-zero elements which implies that the first non-zero row of N_{u_0} is obtained with shift parameter u_0. More generally, row u is obtained with $d = u_0 - u$, implying that N_{u_0} shares row $u_0 - d$ with M_d. We are particularly interested in row $u_0 - 1$, which N_{u_0} shares with M_1. It is obtained by multiplying row u_0 with all columns shifted down by 1 position.

Lemma 1 (Shift Lemma)**.** *With a shift by $d = 1$ position, we have*

$$M_1(u,v) = \begin{cases} 1 & \text{if } 0 \leq v \leq u, \\ 0 & \text{otherwise}, \end{cases} \tag{2.10}$$

for all u and v.

$$\begin{array}{|ccccccccc|}
\hline
1 & & & & & & & & \\
3 & 1 & & & & & & & \\
3 & 2 & 1 & & & & & & \\
1 & 1 & 1 & 1 & & & & & \\
 & & & & 1 & & & & \\
 & & & & -1 & 1 & & & \\
 & & & & 1 & -2 & 1 & & \\
\hline
\end{array}$$

Figure 2.2: The first few non-zero rows of the matrix N_4.

Proof. We note that row u of M_1 is equal to row u of N_{u+1}. It thus suffices to show that

$$N_{u_0}(u,v) = \begin{cases} 1 & \text{if } 0 \le v \le u, \\ 0 & \text{otherwise,} \end{cases} \tag{2.11}$$

for $u_0 = u + 1$. To see this, we construct the columns of N_{u_0} from left to right. Column 0 is obtained by multiplying R_{u_0} with shifted copies of C_0. Writing $d = u_0 - u$, we get

$$\begin{aligned}
N_{u_0}(u,0) &= \sum_{j=-\infty}^{\infty} R_{u_0}(j) \cdot C_0(j-d) && (2.12)\\
&= \sum_{j \ge d} (-1)^{j-d} R_{u_0}(j) && (2.13)\\
&= \sum_{j \ge 0} (-1)^{j} R_{u_0}(d+j) && (2.14)\\
&= \sum_{j \ge 0} (-1)^{j} R_{u_0}(u-j). && (2.15)
\end{aligned}$$

We get (2.13) because the non-zero entries of C_0 alternate between 1 and -1, we get (2.14) with an index transformation, and we get (2.15) using $R_{u_0}(v) = R_{u_0}(u_0 - v)$. Note that (2.15) is the same as the right hand side of (2.6) after substituting u_0 for u and u for v. We conclude that column 0 of N_{u_0} is the transpose of R_{u_0-1}. Next we show that column $v+1$ of N_{u_0} can be obtained from column v:

$$\begin{aligned}
N_{u_0}(u,v+1) &= \sum_{j=-\infty}^{\infty} R_{u_0}(j) \cdot C_{v+1}(j-d) && (2.16)\\
&= \sum_{j \ge d+v+1} R_{u_0}(j) \cdot \sum_{i \ge 0} (-1)^i C_v(i') && (2.17)\\
&= \sum_{i \ge 0} (-1)^i \sum_{j \ge d+v+1} R_{u_0}(j) \cdot C_v(i') && (2.18)\\
&= \sum_{i \ge 0} (-1)^i N_{u_0}(u-i-1, v), && (2.19)
\end{aligned}$$

where $i' = j - d - i - 1$. We get (2.17) using (2.7), we get (2.18) by exchanging sums, and we get (2.19) using (2.9) and noting that $j - u_0 + (u - i - 1) = i'$. Observe that (2.19) is but a rewriting of (2.7) for the columns of N_{u_0}. Applying (2.19) to column 0, which is R_{u_0-1} transposed, thus gives R_{u_0-2} transposed and shifted down by one position. Repeating the argument, we get transposed copies of R_{u_0-1} down to R_0, progressively shifting down so that their respective last non-zero entries populate row $u_0 - 1$ of N_{u_0}. We thus have $N_{u_0}(u_0 - 1, v) = 1$ for $0 \leq v \leq u_0 - 1$, while the other entries in this row are trivially 0. This implies (2.11) and therefore the claimed relation. □

Long inclusion-exclusion. We use the insight gained into the Pascal triangles to generalize the principle of inclusion-exclusion from unions to k-fold covers. To make this precise, let $\mathcal{X}$ be a finite collection of sets in $\mathbb{R}^n$. Let k be an integer, and write $\mathbb{X}_k$ for the set of points contained in k or more of the sets in $\mathcal{X}$. We write $\mathbb{X} = \mathbb{X}_1$. Standard inclusion-exclusion implies that the indicator function of the union is the alternating sum of the indicator functions of the common intersections:

$$\mathbf{1}_{\mathbb{X}}(x) = \sum_{i=1}^{\infty} (-1)^{i-1} \sum_{Q \in \binom{\mathcal{X}}{i}} \mathbf{1}_{\bigcap Q}(x). \tag{2.20}$$

To generalize (2.20) to k-fold covers, we introduce integer coefficients that depend on the size of the subcollections.

Theorem 1 (k-fold Pie Theorem)**.** *Let $\mathcal{X}$ be a finite collection of measurable sets in $\mathbb{R}^n$, and k a positive integer. Then*

$$\mathrm{vol}[\mathbb{X}_k] = \sum_{i=k}^{\infty} (-1)^{i-k} \binom{i-1}{k-1} \sum_{Q \in \binom{\mathcal{X}}{i}} \mathrm{vol}[\bigcap Q]. \tag{2.21}$$

Proof. We prove that the indicator function of the k-fold cover satisfies

$$\mathbf{1}_{\mathbb{X}_k}(x) = \sum_{i=k}^{\infty} (-1)^{i-k} \binom{i-1}{k-1} \sum_{Q \in \binom{\mathcal{X}}{i}} \mathbf{1}_{\bigcap Q}(x). \tag{2.22}$$

The claimed volume formula follows by integration. Let x be a point in $\mathbb{R}^n$, and let ℓ be the number of sets in $\mathcal{X}$ that contain x. Then x belongs to $\binom{\ell}{i}$ common intersections of i sets, for every $i \geq 1$. Each such common intersection is counted $(-1)^{i-k}\binom{i-1}{k-1} = C_{k-1}(i-1)$ times in (2.22). Hence, x is counted

$$\binom{\ell}{i} (-1)^{i-k} \binom{i-1}{k-1} = R_\ell(i) \cdot C_{k-1}(i-1) \tag{2.23}$$

times as a member of the common intersection of i sets. To have a correct indicator function, we need x to be counted once if $1 \leq k \leq \ell$ and zero times otherwise. Indeed,

$$\sum_{i=-\infty}^{\infty} R_\ell(i) \cdot C_{k-1}(i-1) = M_1(\ell - 1, k - 1), \tag{2.24}$$

which by the Shift Lemma is 1 if $1 \leq k \leq \ell$ and 0 otherwise, as required. □

2.3 Geometric background

This section provides background on Voronoi diagrams and hyperplane arrangements; see de Berg, van Kreveld, Overmars and Schwarzkopf [de Berg *et al.*, 1997] for computational aspects of these concepts.

Covers. Let $B(x, r)$ be the closed ball with center $x \in \mathbb{R}^n$ and radius $r \geq 0$. Writing $B_i = B(x_i, r_i)$, we let $\mathcal{B} = \{B_1, B_2, \ldots, B_m\}$ be a finite set of balls in $\mathbb{R}^n$. For each point $x \in \mathbb{R}^n$, let $\#\mathcal{B}(x)$ be the number of balls in $\mathcal{B}$ that contain x. For every integer k, the *k-fold cover* of $\mathcal{B}$ is

$$\mathbb{B}_k = \{x \in \mathbb{R}^n \mid \#\mathcal{B}(x) \geq k\}, \tag{2.25}$$

the set of points contained in at least k of the balls; see Figure 2.3. We write $\mathbb{B} = \mathbb{B}_1$ for the union of the balls. Note that $\mathbb{B}_k = \mathbb{R}^n$ for all $k \leq 0$, $\mathbb{B}_{k+1} \subseteq \mathbb{B}_k$ for all integers k, and $\mathbb{B}_k = \emptyset$ for all $k > m$.

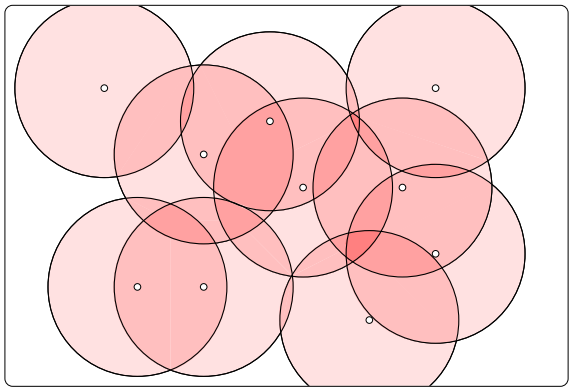

Figure 2.3: The ten disks have non-empty 1-fold, 2-fold, 3-fold, and 4-fold covers, while the 5-fold cover is empty.

Voronoi diagrams. The *weighted distance* from the ball B_i is defined by the function $\pi_i \colon \mathbb{R}^n \to \mathbb{R}$ that maps a point $x \in \mathbb{R}^n$ to $\pi_i(x) = \|x - x_i\|^2 - r_i^2$. For example if $r_i = 0$,

then $\pi_i(x)$ is the squared Euclidean distance from the center of B_i. Following [Shamos and Hoey, 1975], we define the *Voronoi domain* of a subset $Q \subseteq \mathcal{B}$ as the set of points $x \in \mathbb{R}^n$ for which $\pi_q(x) \leq \pi_\ell(x)$ for all $B_q \in Q$ and all $B_\ell \in \mathcal{B} \setminus Q$. Given an integer k, the *order-k Voronoi diagram* of $\mathcal{B}$ is the collection of Voronoi domains of sets Q of size k. As an example, the solid edges in Figure 2.4 show the order-2 Voronoi diagram of the disks in Figure 2.3. We find it convenient to generalize the concept by allowing for two parameters, $j < k$. The *Voronoi domain of a pair* $P \subset Q \subseteq \mathcal{B}$ is the set of points x whose weighted distance to the balls in Q is at least that to the balls in P and at most that to the other balls in $\mathcal{B}$:

$$\mathrm{Vor}(P, Q) = \{x \in \mathbb{R}^n \mid \pi_p(x) \leq \pi_q(x) \leq \pi_\ell(x)\}, \tag{2.26}$$

for all $B_p \in P$, all $B_q \in Q \setminus P$, and all $B_\ell \in \mathcal{B} \setminus Q$. Note that $\mathrm{Vor}(Q) = \mathrm{Vor}(\emptyset, Q)$ is the Voronoi domain of Q as defined above. Being the intersection of finitely many closed half-spaces, $\mathrm{Vor}(P, Q)$ is a possibly empty convex polyhedron. Collecting all Voronoi domains for pairs of sizes $j < k$, we get the (j, k)-*Voronoi diagram*:

$$V_{j,k}(\mathcal{B}) = \{\mathrm{Vor}(P, Q) \mid P \subset Q \subseteq \mathcal{B}\}, \tag{2.27}$$

where $\operatorname{card} P = j$ and $\operatorname{card} Q = k$; see Figure 2.4. We are primarily interested in the case $j = 0$, which is the order-k Voronoi diagram, and the case $j = k - 1$, which is the degree-k Voronoi diagram as defined in [Edelsbrunner, 1987, page 207]. We write $V_k(\mathcal{B}) = V_{0,k}(\mathcal{B})$ and $V(\mathcal{B}) = V_1(\mathcal{B}) = V_{0,1}(\mathcal{B})$.

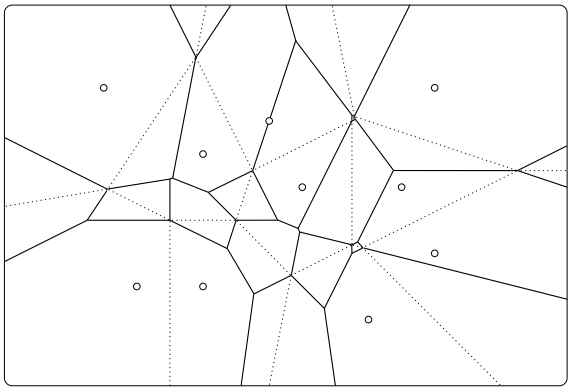

Figure 2.4: The solid lines show the $(0, 2)$-Voronoi diagram, and the solid together with the dotted lines show the $(1, 2)$-Voronoi diagram of the disks in Figure 2.3.

A *cell*, γ, of the (j, k)-Voronoi diagram is a non-empty common intersection of a collection of Voronoi domains. We call it an *i-cell* if its dimension is $\dim \gamma = i$ or,

equivalently, $\operatorname{codim}\gamma = n - i$. For example, the n-cells are the Voronoi domains, and the 0-cells are the vertices. The cells form a complex in the usual sense of the term: the cells have pairwise disjoint interiors and the boundary of every cell is a union of lower-dimensional cells. As a word of caution, we mention that this complex is not necessarily simple, not even if the balls in $\mathcal{B}$ satisfy reasonable general position requirements. For example, many vertices in the $(1,2)$-Voronoi diagram shown in Figure 2.4 belong to six rather than three domains as required for a simple complex in $\mathbb{R}^2$.

Affine functions. Important aspects of the Voronoi diagrams are easier to explain by first mapping the balls in $\mathbb{R}^n$ to non-vertical hyperplanes in $\mathbb{R}^{n+1}$. We therefore introduce the affine functions $A_i\colon \mathbb{R}^n \to \mathbb{R}$ defined by $A_i(x) = 2\langle x, x_i\rangle - \|x_i\|^2 + r_i^2$ for $1 \le i \le m$, writing $\mathcal{A} = \mathcal{A}(\mathcal{B})$ for the set of these functions. At each point $x \in \mathbb{R}^n$, we may sort the values of the m functions and form new functions by selecting the pieces where a single function is the k-largest. More formally, we introduce functions $f_k\colon \mathbb{R}^n \to \mathbb{R}$, for $1 \le k \le m$, defined by $f_k(x) = \xi$ such that $A_i(x) > \xi$ for at most $k-1$ indices, and $A_i(x) < \xi$ for at most $m-k$ indices. To explain the connection to the Voronoi diagrams of $\mathcal{B}$, we introduce $\varpi\colon \mathbb{R}^n \to \mathbb{R}$ defined by $\varpi(x) = \|x\|^2$. For each $x \in \mathbb{R}^n$, the difference between the values of A_i and ϖ at x is the weighted distance of x from B_i:

$$\varpi(x) - A_i(x) = \|x\|^2 - 2\langle x, x_i\rangle + \|x_i\|^2 - r_i^2 = \|x - x_i\|^2 - r_i^2, \tag{2.28}$$

for $1 \le i \le m$. We can therefore express the k-fold cover as well as the $(k-1,k)$-Voronoi diagram in terms of the arrangement.

Lemma 2 (Level Projection Lemma)**.** *Let $\mathcal{B}$ be a set of m balls in $\mathbb{R}^n$, and $\mathcal{A}$ the corresponding set of affine functions from $\mathbb{R}^n$ to $\mathbb{R}$. Then*

(i) $x \in \mathbb{B}_k$ iff $f_k(x) \ge \varpi(x)$, and

(ii) f_k is affine on every domain of the $(k-1,k)$-Voronoi diagram of $\mathcal{B}$.

Instead of giving a proof, which is not difficult, we illustrate the result in dimension $n = 1$; see Figure 2.5.

Hyperplane arrangements. The graphs of the A_i are n-planes that partition $\mathbb{R}^{n+1}$ into open convex cells of dimension 0 to $n+1$. We call this partition the *arrangement* of the n-planes. Each *cell* is characterized by a partition $\mathcal{A} = \mathcal{A}^+ \sqcup \mathcal{A}^0 \sqcup \mathcal{A}^-$, and consists of all

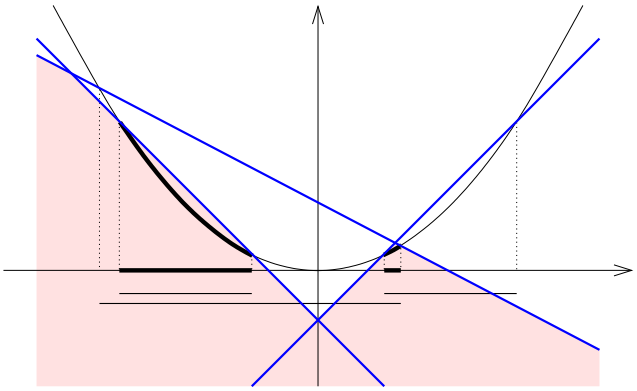

Figure 2.5: Three intervals in $\mathbb{R}^1$ and the corresponding lines in $\mathbb{R}^2$. The 2-nd level of the arrangement projects to the $(1,2)$-Voronoi diagram. The points of the parabola that lie on or below the 2-nd level project to the points of the 2-fold cover.

points $(x,\xi) \in \mathbb{R}^n \times \mathbb{R}$ such that ξ is smaller than, equal to, larger than $A_i(x)$ whenever $A_i \in \mathcal{A}^+, \mathcal{A}^0, \mathcal{A}^-$. The cells of dimension $n+1$ are referred to as *chambers*. Note that the graph of f_k is a union of cells of dimension 0 to n in the arrangement and does not include any chambers. We call this the *k-th level* of the arrangement. To simplify the exposition, we assume the n-planes are in *general position*. By this we mean that the common intersection of any p of the n-planes in $\mathcal{A}$ is a q-plane with $p+q = n+1$ in $\mathbb{R}^{n+1}$. In particular, if $p > n+1$, then the common intersection is empty. Assuming general position, the subset $\mathcal{A}^0 \subseteq \mathcal{A}$ in the partition that characterizes a q-cell has cardinality p. It follows that the q-cell belongs to exactly p levels of the arrangement.

It is perhaps surprising but not difficult to see that the number of q-cells in an arrangement of m n-planes in general position can be written as a function of m, n, and q and thus does not depend on the n-planes themselves:

$$\#\mathrm{Cells}_q^{n+1}(m) = \binom{m}{p} \cdot \sum_{i=0}^{q} \binom{m-p}{i}, \tag{2.29}$$

where $p+q = n+1$, as usual; see e.g. [Edelsbrunner, 1987, page 10]. For example, the number of chambers is $\#\mathrm{Cells}_{n+1}^{n+1}(m) = \sum_{i=0}^{n+1} \binom{m}{i}$. For other values of q, we get the number of q-cells by counting the (q-dimensional) chambers in the arrangements within the q-planes defined by the n-planes. We have $\binom{m}{p}$ such q-planes, with $\#\mathrm{Cells}_q^q(m-p)$ chambers each, which implies (2.29).

Cubes. In the analysis of local structures within the hyperplane arrangement, we will need a few combinatorial facts about the $(n+1)$-dimensional unit cube, $[0,1]^{n+1}$. For

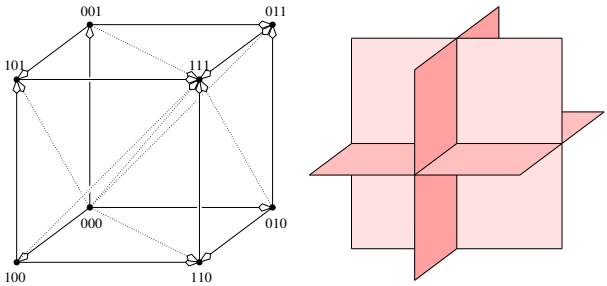

Figure 2.6: *Left*: the 3-dimensional unit cube with edges indicating the partial order on the vertices. *Right*: the dual vertex star in a 3-dimensional arrangement. The direction we call *vertical downward* in the text is given by the vector from vertex 000 to vertex 111.

$0 \leq p \leq n+1$, its number of p-faces is

$$\#\mathrm{Faces}_p^{n+1} = \binom{n+1}{p} \cdot 2^{n+1-p}. \tag{2.30}$$

To see (2.30), we select $q = n+1-p$ coordinate directions and intersect the $(n+1)$-cube with a q-plane parallel to these directions. There are $\binom{n+1}{q} = \binom{n+1}{p}$ choices, each producing a q-cube with $2^q = 2^{n+1-p}$ vertices. Each of these vertices lies on a p-face of the $(n+1)$-cube.

Each of the $n+1$ coordinates of a vertex u of the $(n+1)$-cube is either 0 or 1, and we write $\#u$ for the number of coordinates that are equal to 1. Directing the edges of the cube from smaller to larger numbers of 1s, we get a partial order of the vertices; see Figure 2.6. There is a bijection between the faces and the pairs $u \preceq v$ of the partial order, and we call u the *lower* and v the *upper bound* of the face. The dimension of the face is of course $p = \#v - \#u$. As noted in the proof of (2.30), the p-faces of the $(n+1)$-cube can be organized in $\binom{n+1}{p}$ sets, each the product of a p-face with the vertices of a q-cube. The number of vertices of the q-cube with $\#u = k$ is $\binom{q}{k}$. It follows that the number of p-faces of the $(n+1)$-cube whose lower and upper bounds satisfy $\#u = k$ and $\#v = k+p$ is

$$\#\mathrm{Faces}_{p,k}^{n+1} = \binom{n+1}{p}\binom{q}{k} = \frac{(n+1)!}{p! \cdot k! \cdot (q-k)!}. \tag{2.31}$$

Note that $\#\mathrm{Faces}_{p,k}^{n+1} = 0$ whenever $p \notin [0, n+1]$ or $k \notin [0, q]$.

2.4 Order-k formulas

In this section, we use the geometry of the problem to derive a first set of short inclusion-exclusion formulas that generalize the formulas in [Naiman and Wynn, 1992; Edelsbrunner, 1995b] from the union to the k-fold cover.

Star-convexity. As before, we let $\mathcal{B}$ be a finite set of balls in $\mathbb{R}^n$, and we write $\mathbb{B}_k$ for the set of points in $\mathbb{R}^n$ that are contained in at least k of the balls. Writing $V_k = V_{0,k}(\mathcal{B})$ for the order-k Voronoi diagram, we note that its domains decompose the k-fold cover into convex sets; see Figure 2.7. We need a structural property of the Voronoi domains

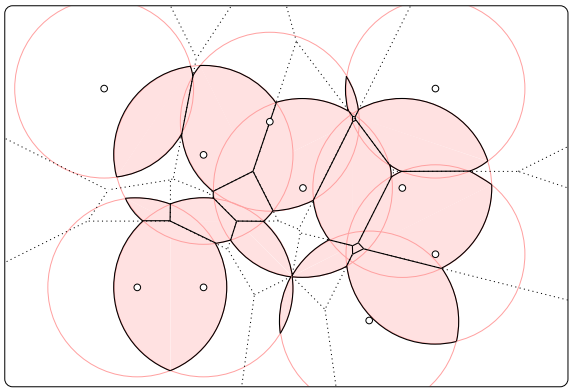

Figure 2.7: The 2-fold cover of the ten disks in Figure 2.3. The order-2 Voronoi diagram decomposes the cover into convex sets, each the intersection of a Voronoi domain with two disks.

and their restrictions to the k-fold cover. To state it, we recall that $\mathrm{Vor}(Q)$ is the Voronoi domain of Q, and we write $\mathrm{Res}(Q) = \bigcap Q \cap \mathrm{Vor}(Q)$ for its restriction to the common intersection of the balls. Given a point $x \in \mathbb{R}^n$, we let $\mathcal{Q}_k(x)$ be the system of collections $Q \subseteq \mathcal{B}$ of size k that satisfy $x \in \bigcap Q$ and $\mathrm{Vor}(Q) \neq \emptyset$. Clearly, if $x \notin \mathbb{B}_k$, then $\mathcal{Q}_k(x)$ is empty. If $x \in \mathbb{B}_k$, then $\mathcal{Q}_k(x)$ is necessarily non-empty as it contains all collections Q of size k with $x \in \mathrm{Vor}(Q)$, but there may be additional collections in the system. We are interested in the union of the restricted and unrestricted Voronoi domains whose balls contain the point x:

$$\mathbb{V}_k(x) = \bigcup_{Q \in \mathcal{Q}_k(x)} \mathrm{Vor}(Q), \tag{2.32}$$

$$\mathbb{R}_k(x) = \bigcup_{Q \in \mathcal{Q}_k(x)} \mathrm{Res}(Q). \tag{2.33}$$

To prepare the analysis of these sets, we recall a basic property of the weighted distance functions. If B_i and B_j are balls in $\mathbb{R}^n$, then $f\colon \mathbb{R}^n \to \mathbb{R}$ defined by $f(x) = \pi_i(x) - \pi_j(x)$ is an affine function:

$$\begin{aligned} f(x) &= \|x - x_i\|^2 - r_i^2 - \|x - x_j\|^2 + r_j^2 \\ &= 2\langle x, x_j - x_i\rangle + \|x_i\|^2 - \|x_j\|^2 - r_i^2 + r_j^2. \end{aligned} \tag{2.34}$$

It follows that the restriction of f to any line, L, in $\mathbb{R}^n$ is an affine function that is constant iff L is normal to $x_j - x_i$. The main property of interest is the *star-convexity* of $\mathbb{V}_k(x)$ and $\mathbb{R}_k(x)$. In particular, we will show that for every point y in $\mathbb{V}_k(x)$ or $\mathbb{R}_k(x)$, the entire line segment connecting x with y is contained in this set.

Lemma 3 (Star-convexity Lemma)**.** *Let $\mathcal{B}$ be a finite set of balls in $\mathbb{R}^n$, k an integer, and x a point in $\mathbb{R}^n$. Then $\mathbb{V}_k(x)$ is either empty or star-convex, and so is $\mathbb{R}_k(x)$.*

Proof. We first consider $\mathbb{V}_k(x)$. Assuming $x \in \mathbb{B}_k$, we let y be a point in $\mathbb{V}_k(x)$, and we let Q be a collection of k balls in $\mathcal{B}$ such that $y \in \mathrm{Vor}(Q)$. By construction, the balls in Q minimize the weighted distance for y, and the weighted distance of x to any of these balls is non-positive. Let L be the line that passes through x and y, and let $u \in L$ be strictly between x and y. To derive a contradiction, assume $u \notin \mathbb{V}_k(x)$. Then there exists a ball $B_0 \in \mathcal{B}$ that is among the k closest for u such that $\pi_0(x) > 0$. It can therefore not be in Q. Hence, there is a ball $B_1 \in Q$ with $\pi_0(u) \leq \pi_1(u)$. But we also have $\pi_1(y) \leq \pi_0(y)$ and $\pi_1(x) < \pi_0(x)$, which contradicts that $\pi_1 - \pi_0$ restricts to an affine function on L. We conclude that $u \in \mathbb{V}_k(x)$, which implies that $\mathbb{V}_k(x)$ is star-convex, as claimed.

The argument for the restricted Voronoi domains is similar, implying that $\mathbb{R}_k(x)$ is star-convex as well. □

Short inclusion-exclusion. The formulas we prove have at most one term for each cell in the order-k Voronoi diagram. For constant dimension, the number of such cells is bounded from above by a polynomial in the number of balls, which is much smaller than the number of subsets of the balls. This is our justification for calling the formulas *short*. To state them, we associate each cell γ of V_k with the subset $Q_\gamma \subseteq \mathcal{B}$ of balls

that are among the k closest for at least one Voronoi domain containing γ. Assuming general position, we have

$$k \leq \operatorname{card} Q_\gamma \leq k + n. \tag{2.35}$$

To prove these inequalities, we set $q = n - \dim \gamma$ and observe that $k = \operatorname{card} Q_\gamma$ iff $q = 0$. To prove the upper bound, we assume $q > 0$ and let x be an interior point of γ. By assumption of general position, x has equal weighted distance to $q + 1$ balls. Let ℓ be the number of balls to which x has smaller weighted distance than to these $q + 1$ balls. We have $\ell < k$, else γ would not be a face of the Voronoi domains. The k balls defining a Voronoi domain that contains γ include the ℓ balls as well as $k - \ell$ of the $q + 1$ balls. It follows that Q_γ contains the ℓ balls together with the $q + 1$ balls. But $\ell < k$ and $q \leq n$, which implies $\operatorname{card} Q_\gamma \leq \ell + q + 1 \leq k + n$, as claimed.

To state the main result of this section, we introduce two subsystems of the nerve of $V_k(\mathcal{B})$, which is an abstract simplicial complex. Recall that every simplex in the nerve is a collection of Voronoi domains that intersect in a non-empty cell of the order-k Voronoi diagram. We call a simplex *maximal* if it is not a proper face of a simplex whose domains intersect in the same cell. The first subsystem, $\mathcal{V}_k$, consists of all maximal simplices in the nerve of $V_k(\mathcal{B})$. Making use of the bijection between the simplices in $\mathcal{V}_k$ and the cells in V_k we write $\gamma(\sigma)$ for the common intersection of the Voronoi domains in $\sigma \in \mathcal{V}_k$. The second subsystem, $\mathcal{R}_k$, is defined similarly, except that it is limited to simplices whose corresponding cells have non-empty intersection with $\mathbb{B}_k$. As before, we pick only maximal simplices from this smaller system.

Theorem 2 (Order-k Pie Theorem)**.** *Let $\mathcal{B}$ be a finite set of balls in $\mathbb{R}^n$, and k an integer. Then the volume of the k-fold cover is*

$$\operatorname{vol}[\mathbb{B}_k] = \sum_{\sigma \in \mathcal{V}_k} (-1)^{\operatorname{codim} \gamma(\sigma)} \operatorname{vol}[\bigcap Q_{\gamma(\sigma)}], \tag{2.36}$$

$$= \sum_{\sigma \in \mathcal{R}_k} (-1)^{\operatorname{codim} \gamma(\sigma)} \operatorname{vol}[\bigcap Q_{\gamma(\sigma)}]. \tag{2.37}$$

Proof. We first prove (2.36). Recall that $\mathbb{V}_k(x)$ is the union of the order-k Voronoi domains, $\operatorname{Vor}(Q)$, such that $x \in \bigcap Q$. Each such domain is a vertex in $\mathcal{V}_k$, and we write $\mathcal{V}_k(x) \subseteq \mathcal{V}_k$ for the simplices these vertices span. We introduce $\chi \colon \mathbb{R}^n \to \mathbb{R}$ defined by mapping x to the Euler characteristic of $\mathbb{V}_k(x)$. To avoid any ambiguity arising for

unbounded sets, we clip $\mathbb{R}^n$ to within a sufficiently large n-dimensional box and take the Euler characteristic of $\mathbb{V}_k(x)$ intersected with this box. Recall that $\mathbb{V}_k(x)$ is either empty or star-convex. In the former case, the Euler characteristic is 0, and in the latter case, it is 1. Hence, χ is the indicator function of the k-fold cover:

$$\chi(x) = \begin{cases} 1 & \text{if } x \in \mathbb{B}_k, \\ 0 & \text{if } x \notin \mathbb{B}_k. \end{cases} \tag{2.38}$$

It follows that $\mathrm{vol}[\mathbb{B}_k] = \int_{x\in\mathbb{R}^n} \chi(x)\,\mathrm{d}x$. By the Nerve Theorem[Leray, 1945; Borsuk, 1948], $\chi(x)$ is the alternating sum of simplices in the nerve of the Voronoi domains whose union is $\mathbb{V}_k(x)$. If the Voronoi diagram is simple, then $\mathcal{V}_k(x)$ contains all and exactly these simplices and we are done. In the general case however, $\mathcal{V}_k(x)$ may contain fewer simplices, and our task is to show that they suffice to compute the Euler characteristic of $\mathbb{V}_k(x)$.

To explain this, let γ be a cell of V_k, and let $\ell + 1 \geq n + 1 - \dim\gamma$ be the number of Voronoi domains that contain γ. The corresponding ℓ-simplex in the nerve of V_k is maximal, but if $\ell + 1 > n + 1 - \dim\gamma$, then this ℓ-simplex has faces that are not maximal. We continue the proof assuming γ is a vertex. Indeed, if $\dim\gamma > 0$ then we may intersect the local configuration with an orthogonal $(n - \dim\gamma)$-plane, which intersects γ in a point. The remainder of the argument would then be worded within this $(n - \dim\gamma)$-dimensional plane.

Thus assuming $\dim\gamma = 0$, we distinguish between the maximal and non-maximal faces by drawing a sufficiently small $(n-1)$-sphere with center at γ. Denote this sphere as S and the n-ball bounded by S as B (Figure 2.8, left). The Voronoi domains intersect B in $\ell + 1$ cones and S in $\ell + 1$ $(n - 1)$-dimensional caps, which are the bases of the cones. The nerve of the cones is isomorphic to the nerve of the Voronoi domains. To relate the nerve of the caps to the nerve of the Voronoi domains, we map each cap in S to the corresponding cone in B. Let τ be a face of the ℓ-simplex, and consider the common intersection of its Voronoi domains. It is not difficult to see that this common intersection is γ iff τ does not correspond to a simplex in the nerve of the caps in S. Since the cones form an n-ball and the $(n - 1)$-caps form an $(n - 1)$-sphere, the Euler characteristic of their nerves are 1 and $1 + (-1)^{n-1}$, respectively. It follows that the

alternating sum of the non-maximal simplices whose Voronoi domains intersect in γ is:

$$1-(-1)^{\ell}-[1+(-1^{n-1})]=\begin{cases}2 & \text{if } \ell \text{ is odd and } n \text{ is even,}\\ 0 & \text{if } \ell-n \text{ is even,}\\ -2 & \text{if } \ell \text{ is even and } n \text{ is odd.}\end{cases} \tag{2.39}$$

In words, the alternating sum of the non-maximal simplices is precisely the difference between the contribution of the vertex γ and the ℓ-simplex:

$$(-1)^{n}-(-1)^{\ell}=(-1)^{\operatorname{codim}\gamma}-(-1)^{\ell}. \tag{2.40}$$

This proves the claimed formula for points x equal to or sufficiently close to γ. We need additional arguments for points x that are not contained in the intersection of the k balls for all Voronoi domains meeting at γ.

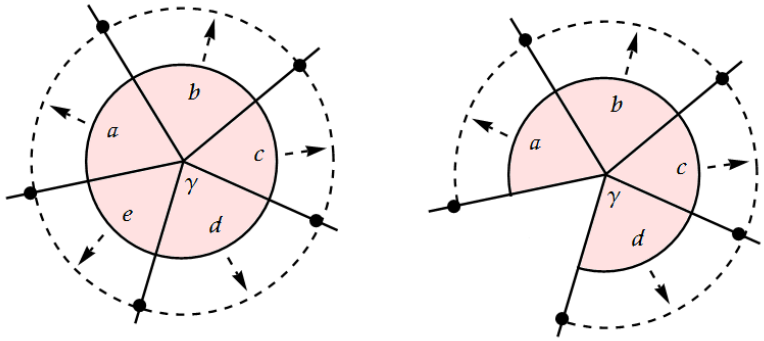

Figure 2.8: The ℓ-simplex has non-maximal faces $ad, bd, acd, \ldots$. On the left, with $\ell = 4$ and $n = 2$, we shade the ball and draw the partition into caps as dashed arcs. On the right, with $\ell = 4$ and $j = 3$, only a proper subset of the Voronoi domains contain x.

Suppose $j+1 < \ell+1$ of the Voronoi domains meeting at γ contain x in the intersection of their balls. The nerve of the corresponding $j+1$ cones in B is a j-simplex with Euler characteristic equal to 1 (Figure 2.8, right). We will prove shortly that the Euler characteristic of the corresponding $j+1$ caps is also equal to 1. The alternating sum of the non-maximal faces of the j-simplex is the difference, which vanishes as desired. It remains to prove that the Euler characteristic of the union of the $j+1$ caps is 1. It suffices to prove that this union is homologically trivial, with $\beta_0 = 1$ the only non-zero Betti number. Suppose it is not (Figure 2.9, left). Then there is a non-bounding cycle, Z, in the union of caps. By construction $Z \subseteq \mathbb{V}_k(x)$, and since $\mathbb{V}_k(x)$ is star-convex we can draw straight line segments from x to all points of Z and thus form a chain, C, with

boundary Z (Figure 2.9, middle). Since we can locally perturb x, we may assume that the point γ does not belong to C. We can therefore centrally project C from γ to S. By construction, the image of this projection is a chain in the union of caps (Figure 2.9, right). Its boundary is Z, which contradicts the assumption that the union of caps is homologically non-trivial.

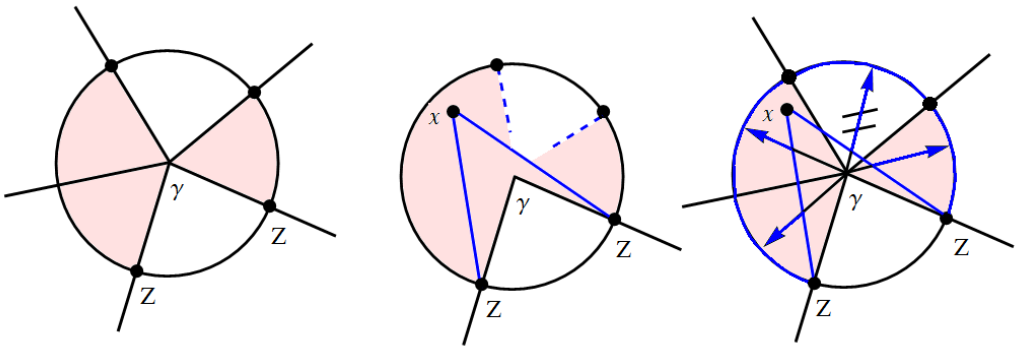

Figure 2.9: Hypothetical example in which the union of caps is homologically non-trivial, as indicated by the shaded Voronoi domains in $\mathbb{V}_k(x)$. Such configuration leads to a contradiction.

To make the step to the claimed equation, we repackage the contributions of the points x to the integral. Specifically, we focus on a cell γ of the order-k Voronoi diagram. The contribution of γ to the integral is ± 1 times the integral of 1 over all points in $\bigcap Q_\gamma$. The sign alternates with the codimension, which gives $(-1)^{\operatorname{codim}\gamma}$, and the integral evaluates to the volume of the common intersection. This implies (2.36). The proof of (2.37) is the same, using again that the sets $\mathbb{R}_k(x)$ are star-convex. □

For $k = 1$, (2.36) specializes to the formula for the volume of the union of balls given in [Naiman and Wynn, 1992], and (2.37) specializes to the smaller formula given in [Edelsbrunner, 1995b]. We note that the terms in the difference between the two formulas are not necessarily zero. Even for $k = 1$, the first formula may contain non-zero terms that cancel with others and do not belong to the second formula.

2.5 Level-k formulas

In this section, we present an alternative approach to deriving short inclusion-exclusion formulas for the k-fold cover. Importantly, it leads to formulas whose terms are limited to common intersections of at most $n+1$ balls.

Indicator function for polyhedra. Letting $\mathcal{B}$ be a set of m balls in $\mathbb{R}^n$, we write $\mathcal{A}$ for the corresponding set of m affine functions from $\mathbb{R}^n$ to $\mathbb{R}$, as introduced in Section 2.3. For an integer k, let $\mathbb{U}_k$ be the set of points $y \in \mathbb{R}^{n+1}$ that lie on or above the k-th level of $\mathcal{A}$, and let $\mathbb{L}_k$ be the set of points on or below the k-th level; see Figure 2.5, which shows $\mathbb{L}_2$ for three intervals in $\mathbb{R}^1$.

To derive the formulas, we begin with $\mathbb{U}_k$ and then move to $\mathbb{L}_k$. Because $\mathbb{U}_k$ is a not necessarily convex polyhedron, its indicator function can be assembled from simple components, each the indicator function of a face and its immediate neighborhood; see [Edelsbrunner, 1995a]. To explain how this works, we refer to the faces of $\mathbb{U}_k$ as *sides*. For $0 \leq q \leq n$, the q-sides of $\mathbb{U}_k$ are the closures of the q-cells in the arrangement that belong to the k-th level. Clearly, all these cells are convex. The only $(n+1)$-side of $\mathbb{U}_k$ is $\mathbb{U}_k$ itself, which is not necessarily convex but contractible. The *star* of a side, ψ, is the set of sides that contain ψ. Let y be a point in the interior of ψ, and let $\varepsilon > 0$ be small enough such that the sphere, S, with center y and radius ε in $\mathbb{R}^{n+1}$ intersects only sides that belong to the star of ψ. The *negative face figure* of ψ is the union of all half-lines that emanate from y whose central reflections pass through points of the intersection of this sphere with the polyhedron:

$$\mathrm{F}_\psi = \{(1-\lambda)y + \lambda u \mid u \in S \cap \mathbb{U}_k, \lambda \leq 0\}. \tag{2.41}$$

Intuitively, it is the central reflection of the local view of the polyhedron as seen from y (Figure 2.10). Note that F_ψ does not depend on the choice of the point y in the interior of ψ. The main theorem in [Edelsbrunner, 1995a] implies that indicator function of $\mathbb{U}_k$ can be written as an alternating sum of indicator functions of interiors of negative face figures: $\mathbf{1}_{\mathbb{U}_k}(y) = \sum_\psi (-1)^{\operatorname{codim}\psi} \cdot \mathbf{1}_{\operatorname{int}\mathrm{F}_\psi}(y)$, in which the sum ranges over all sides of $\mathbb{U}_k$, including $\mathbb{U}_k$ itself for which the negative face figure is the entire $\mathbb{R}^{n+1}$. Substituting the closed for the open negative face figures, the indicator function changes from $\mathbb{U}_k$ to

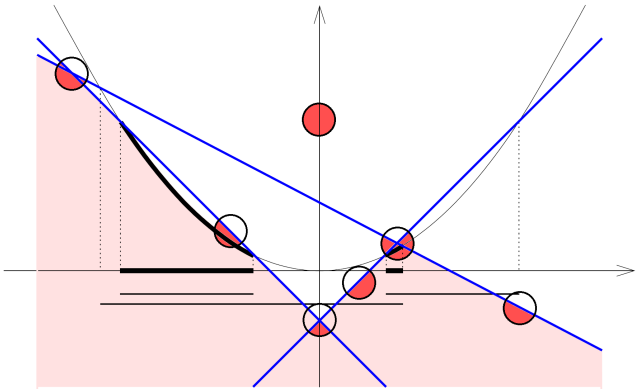

Figure 2.10: The region $\mathbb{U}_2$ above the second level is white and its complement, $\mathbb{L}_2$, is shaded. For each side ψ of $\mathbb{U}_2$, we draw a sphere centered in the interior of ψ and shade the portion of its inside that points in the direction of its negative face figure.

$\operatorname{int}\mathbb{U}_k$, and subtracting it from 1, it changes to the complement, which is closed:

$$\mathbf{1}_{\mathbb{L}_k}(y) = 1 - \mathbf{1}_{\operatorname{int}\mathbb{U}_k}(y) = \sum_{\psi}(-1)^{n-\dim\psi} \cdot \mathbf{1}_{\mathrm{F}_\psi}(y), \tag{2.42}$$

in which the sum now ranges over all sides of dimension 0 to n, which are the same for $\mathbb{U}_k$ and $\mathbb{L}_k$.

Negative face figures. To further decompose the indicator function given in (2.42), we need to understand the negative face figures. It suffices to study a vertex, since the negative face figure of a q-side is that of a vertex in an arrangement of $(n-q)$-planes in $\mathbb{R}^{n+1-q}$, extruded along q additional dimensions. Assuming general position, a vertex w is the intersection of $n+1$ n-planes in $\mathbb{R}^{n+1}$, and its star is dual to a cube of dimension $n+1$; see Figure 2.6. The n-planes are non-vertical so we can order the chambers accordingly, which corresponds to directing the edges of the cube from top to bottom. To make this concrete, we sort the n-planes, and we assign to each chamber a string of $n+1$ labels in which the p-th label is 0 if the chamber lies above the p-th n-plane, and it is 1 if the chamber lies below the p-th n-plane. It should be clear that the assigned labels are the coordinates of the corresponding vertices of the dual $(n+1)$-cube. Let $k_0 + \ell_0 = m - (n+1)$ such that w lies below k_0 and above ℓ_0 of the n-planes. It follows that w belongs to the k-th level of $\mathcal{A}$ iff $k_0 < k \leq m - \ell_0$. Which cells around w belong to the k-th level and are therefore sides $\mathbb{L}_k$ depends solely on $j = j(w) = k - k_0$, which we call the *index* of w. Specifically, the q-cells that belong to the k-th level are dual to p-faces of the $(n+1)$-cube whose lower and upper bounds satisfy $\#u < j \leq \#v$. Using

(2.31), we see that the number of such q-cells is

$$\#\mathrm{Sides}_{q,j}^{n+1} = \sum_{i=j-p}^{j-1} \#\mathrm{Faces}_{p,i}^{n+1}. \tag{2.43}$$

Depending on the index of w, different cells in its neighborhood contribute to the indicator function of its negative face figure. For example in 3 dimensions, we have three indicator functions:

$$j = 1 : abc, \tag{2.44}$$

$$j = 2 : ab + ac + bc - 2abc, \tag{2.45}$$

$$j = 3 : a + b + c - ab - ac - bc + abc, \tag{2.46}$$

where we write a, b, c for the indicator functions of the half-spaces bounded from above by the graphs of the three affine functions. In dimension $n+1$, there are $n+1$ indices and $n+1$ different indicator functions of the negative face figures. To express them formally, we write $\mathbf{1}_A$ for the indicator function of the half-space bounded from above by the affine function A.

Lemma 4 (Face Figure Lemma)**.** *Let $\mathcal{A}$ be a set of $n+1$ affine functions from $\mathbb{R}^n$ to $\mathbb{R}$ whose graphs form an arrangement with a single vertex w in $\mathbb{R}^{n+1}$. For $1 \leq j \leq n+1$, the indicator function of the negative face figure of w with index j satisfies*

$$\mathbf{1}_{\mathrm{F}_w}(y) = \sum_{i=n+2-j}^{n+1} (-1)^{i-n+j} \binom{i-1}{n-j+1} \sum_{\mathcal{A}' \in \binom{\mathcal{A}}{i}} \prod_{A \in \mathcal{A}'} \mathbf{1}_A(y). \tag{2.47}$$

Proof. Since we have only $n+1$ affine functions in $\mathbb{R}^n$, we cannot gain from the geometry of the situation and use the general inclusion-exclusion formula (2.1). Specifically, we use the indicator function from which (2.1) follows by integration:

$$\mathbf{1}_{\mathbb{X}_k}(y) = \sum_{i \geq k} (-1)^{i-k} \binom{i-1}{k-1} \sum_{Q \in \binom{\mathcal{X}}{i}} \mathbf{1}_{\bigcap Q}(y), \tag{2.48}$$

where $\mathcal{X}$ denotes a finite collection of measurable sets in $\mathbb{R}^{n+1}$, and $\mathbb{X}_k$ is the k-fold cover. To specialize this result to our situation, we note that the negative face figure of w is the $(n+2-j)$-fold cover of the $n+1$ closed half-spaces bounded from above by the graphs of the $A_i \in \mathcal{A}$. Substituting $n+2-j$ for k and $\mathcal{A}$ for $\mathcal{X}$, and writing the indicator function of the intersection as a product, we get the claimed relation. □

Short inclusion-exclusion. Combining (2.42) and (2.47), we get the indicator function of $\mathbb{L}_k$ with terms that are products of at most $n+1$ indicator functions of half-spaces. To state it formally, we write $\mathcal{L}_k$ for the abstract simplicial complex whose abstract simplices are the collections $Q \subseteq \mathcal{B}$ such that the graphs of the corresponding affine functions contain a common side of $\mathbb{L}_k$. For each $Q \in \mathcal{L}_k$, we write $\mathbf{1}_Q \colon \mathbb{R}^{n+1} \to \{0,1\}$ for the indicator function of the intersection of half-spaces bounded from above by the graphs of the corresponding affine functions. Combining the mentioned relations, we get $\mathbf{1}_{\mathbb{L}_k}(y) = \sum_{Q \in \mathcal{L}_k} L_Q \cdot \mathbf{1}_Q(y)$, in which L_Q is sum of coefficients of $\mathbf{1}_Q(y)$ contributed by the various negative face figures. We can now compute the n-dimensional volume of the k-fold cover of the set of balls in $\mathcal{B}$ by integration:

$$\operatorname{vol}[\mathbb{B}_k] = \int_{x \in \mathbb{R}^n} \mathbf{1}_{\mathbb{L}_k}(x, \|x\|^2)\,\mathrm{d}x = \sum_{Q \in \mathcal{L}_k} L_Q \int_{x \in \mathbb{R}^n} \mathbf{1}_Q(x, \|x\|^2)\,\mathrm{d}x. \tag{2.49}$$

Note that the last integral is the volume of the intersection of the balls. This gives the first inclusion-exclusion formula for the volume of $\mathbb{B}_k$ derived in this section. However, there are redundant terms that can be removed to obtain an even shorter formula. To identify them, we call a collection of balls, Q, *independent* if for every $P \subseteq Q$ there is a point $x \in \mathbb{R}^n$ such that every ball in P contains x and every ball in $Q \setminus P$ does not contain x; that is: $\bigcap P \setminus \bigcup (Q \setminus P) \neq \emptyset$. Let $\mathcal{I}_k$ be the system of collections $Q \in \mathcal{L}_k$ such that Q is independent. We claim there are integer coefficients I_Q not necessarily equal to L_Q such that the weighted sum over $\mathcal{I}_k$ gives the volume of the k-fold cover. We state both results.

Theorem 3 (Level-k Pie Theorem)**.** *Let $\mathcal{B}$ be a finite set of balls in $\mathbb{R}^n$, and k an integer. Then the volume of the k-fold cover is*

$$\operatorname{vol}[\mathbb{B}_k] = \sum_{Q \in \mathcal{L}_k} L_Q \cdot \operatorname{vol}[\textstyle\bigcap Q] \tag{2.50}$$

$$= \sum_{Q \in \mathcal{I}_k} I_Q \cdot \operatorname{vol}[\textstyle\bigcap Q]. \tag{2.51}$$

Proof. The proof of (2.50) has been given above. To prove (2.51), we show that whenever $Q \in \mathcal{L}_k$ is not independent, then $\operatorname{vol}[\bigcap Q]$ can be written as an integer combination of the $\operatorname{vol}[\bigcap P]$ in which the P are proper subsets of Q. Repeated substitution of dependent terms in (2.50) eventually gives (2.51). To prove that the substitution is always possible, we consider the system of linear equations that relates the volumes of the

common intersections with the volumes of the cells that appear in the definition of independence. Writing

$$\mu = \Big[\mathrm{vol}[\bigcap P]\Big]_{\emptyset \neq P \subseteq Q}, \quad \nu = \Big[\mathrm{vol}[\bigcap P \setminus \bigcup (Q \setminus P)]\Big]_{\emptyset \neq P \subseteq Q} \tag{2.52}$$

for the vectors of volumes, we get $\mu = M\nu$, in which M is a 0-1 matrix. Writing $q = \operatorname{card} Q$, M is a $2^q - 1$ times $2^q - 1$ matrix. It has the regular structure reflecting the incidences between the linear spaces spanned by the non-empty subsets of q independent vectors; see Figure 2.11 for an example. In particular, all entries in the diagonal are 1, and all entries above the diagonal are 0. Furthermore, the number of non-zero entries in each row is a power of 2.

	uvw	uv	uw	vw	u	v	w
uvw	1						
uv	1	1					
uw	1		1				
vw	1			1			
u	1	1	1		1		
v	1	1		1		1	
w	1		1	1			1

Figure 2.11: The matrix relating the vectors μ and ν for a collection of size $\operatorname{card} Q = 3$.

Assume now that Q is not independent. Then at least one component of ν is zero. Equivalently, we may set the corresponding column of M to zero, without violating the correctness of $\mu = M\nu$. This creates dependences between the linear equations. We use the special structure of M to prove that in this case, we can write the volume of $\bigcap Q$ as an integer combination of the $\mathrm{vol}[\bigcap P]$, in which $P \subseteq Q$ but $P \neq Q$. Fixing $2 \leq r \leq 2^q - 1$, we can reduce the r-th row until its only non-zero entry is in the diagonal of M. To do this, we work from the diagonal element backward, adding an integer multiple of a row above for every non-zero entry. Since $r \geq 2$, the r-th row contains an even number of 1s before reduction. Adding an integer multiple of any row other than the first changes the sum of non-zero entries by an even number, and since the sum in the end is odd, we conclude that the first row has been added with a non-zero coefficient. If we now set the r-th column to zero, we have a zero r-th row. But this implies that the first row is an integer combination of the r-th row and all rows used in its reduction, other than the first row of course. □

2.6 Computation

In this section, we comment on the main challenges in implementing the inclusion-exclusion formulas for the k-fold cover of balls proved in the preceding sections. Our main concern is the correctness of the formulas, leaving considerations of size and speed to future research. We begin with experimental results for a small 3-dimensional example.

Example. As explained shortly, we implemented two formulas in $n = 3$ dimensions: the order-k formula (2.36) and the level-k formula (2.50), both after reduction. The reduced formulas are readily evaluated without further case analysis. The input for our example is generated by sampling 10 points uniformly at random from the unit cube in $\mathbb{R}^3$. Centering balls of radius 0.25 at these points gives the first set, $\mathcal{B}_1$, and increasing the radius to 0.875 gives the second set, $\mathcal{B}_2$, see Figure 2.12.

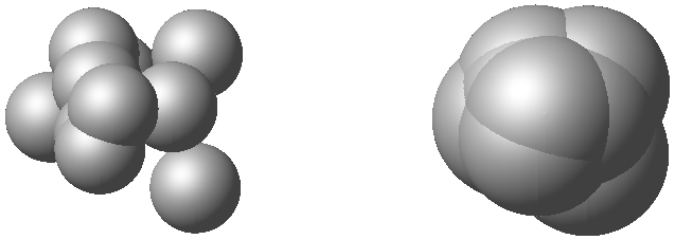

Figure 2.12: Two sets of ten random balls with centers in the unit cube and radii 0.25 on the *left* and radii 0.875 on the *right*.

Computing the volume of the k-fold cover of $\mathcal{B}_1$ and $\mathcal{B}_2$, for $k = 1, 2, \ldots, 10$, we show the volume as well as the number of terms and the average number of balls per term in Table 2.1. In every case, the reduced order-k formula is identical to the reduced level-k formula, so we show only three integers per case: the number of terms of the order-k formula (2.36), of the level-k formula (2.50), and of the reduced formula. While the number of terms in the level-k formulas tend to be smaller than in the order-k formulas, the difference is neither significant nor consistent. We also note that for $\mathcal{B}_1$, most redundant terms have zero volume, while for $\mathcal{B}_2$, all redundant terms have non-zero volume.

	$\mathcal{B}_1$, radius $= 0.25$				$\mathcal{B}_2$, radius $= 0.875$			
k	order-k	level-k	reduced	vol	order-k	level-k	reduced	vol
1	103×2.7	103×2.7	34×2.0	0.523	103×2.7	103×2.7	95×2.6	7.842
2	166×3.4	166×3.1	29×2.4	0.106	166×3.4	166×3.1	149×3.0	5.176
3	220×4.3	219×3.4	14×2.9	0.023	220×4.3	219×3.4	186×3.4	4.137
4	221×5.1	228×3.6	4×3.3	0.001	221×5.1	228×3.6	191×3.5	3.118
5	190×6.0	238×3.6	0×0.0	0.000	190×6.0	238×3.6	189×3.6	2.450
6					140×6.8	203×3.7	156×3.7	1.857
7					80×7.6	184×3.6	128×3.6	1.417
8					34×8.3	127×3.5	80×3.5	1.024
9					9×9.1	65×3.4	32×3.5	0.704
10					1×10.0	17×3.3	11×3.4	0.332

Table 2.1: The volume of the k-fold covers of $\mathcal{B}_1$ and $\mathcal{B}_2$, together with the number of terms in the inclusion-exclusion formulas and the average number of balls per term.

Algorithm. Without going into details, we sketch the main steps in constructing and evaluating an inclusion-exclusion formula for the k-fold cover of a set $\mathcal{B}$ of m balls in $\mathbb{R}^3$. For the order-k formula (2.36), we construct the order-k Voronoi diagram of $\mathcal{B}$ as the order-1 (weighted) Voronoi diagram of the k-fold averages, as explained in [Aurenhammer and Schwarzkopf, 1992]. The latter diagram is then computed with the 3D CGAL weighted Delaunay triangulation software [CGAL]. For the level-k formula (2.50), we construct in addition the order-$(k-1)$ Voronoi diagram and we obtain $V_{k-1,k}(\mathcal{B})$ by superimposing $V_{k-1}(\mathcal{B})$ and $V_k(\mathcal{B})$. While there are standard procedures, we mention that superimposing the two diagrams was perhaps the most laborious task in implementing the algorithm. An important aspect of the above computations is the use of exact arithmetic in making final decisions on the connectivity of the diagrams. Without it, there is little hope to get correct inclusion-exclusion formulas. CGAL offers the exact computation paradigm [Yap and Dubé, 1995] as part of the package, which is the main reason we decided to use CGAL and not one of the many available alternatives. To illustrate the need for exact arithmetic, we mention that already for $k = 2$, the order-k Voronoi diagram is not simple even if the balls are in general position. Taking $m = 4$ points not in a plane, the order-2 Voronoi diagram has six domains that meet at the center of the circumsphere. This is in contrast to the at most four domains that are allowed to meet in a simple diagram in $\mathbb{R}^3$.

Assuming we have $V_k(\mathcal{B})$ or $V_{k-1,k}(\mathcal{B})$, we construct the formula by translating each cell into a term or a small number of terms. This is straightforward for the order-k formula but can be confusing for the level-k formula, for which we give some more details. Iterating over all cells ψ of $V_{k-1,k}(\mathcal{B})$, we write $j(\psi)$ for its index in the corresponding arrangement, as defined in Section 2.5. We begin with an initially empty formula.

CASE 1: $\dim \psi = 3$. Add the volume of the corresponding ball to the formula.

CASE 2: $\dim \psi = 2$. Set $i = 3 - j(\psi)$ and subtract the volume of the i-fold cover of the two corresponding balls.

CASE 3: $\dim \psi = 1$. Set $i = 4 - j(\psi)$ and add the volume of the i-fold cover of the three corresponding balls.

CASE 4: $\dim \psi = 0$. Set $i = 5 - j(\psi)$ and subtract the volume of the i-fold cover of the four corresponding balls.

Once we have the complete formula, we evaluate it, translating each i-fold cover to an alternating sum of intersections among the balls. But even this is not an easy task as the balls we intersect are not in any particular geometric configuration. We therefore first reduce the formula until all terms are independent, as explained shortly. In the reduced formula, we have only four different cases: one, two, three, and four independent balls. Analytic formulas for computing the volume of the intersection in each case can be found in [Edelsbrunner and Fu, 1994].

Reduction. Assume we have an inclusion-exclusion formula for the volume of the k-fold cover of m balls in $\mathbb{R}^3$. Each term is a common intersection of balls, but the collections are not necessarily independent. We now explain how to reduce this formula into a form in which all collections are independent. We proceed one term at a time, starting with one whose collection has a maximum number of balls.

Let Q be the balls that appear in the considered term, and write $q + 1 = \operatorname{card} Q$. If $q > 3$, then we can be sure that Q is not independent, and we can replace this term using a relation computed as described in the proof of the Level-k Pie Theorem. To get started, we need a subset P of Q whose common intersection is contained in the union of $Q \setminus P$, and to find it, we use the affine functions from $\mathbb{R}^3 \to \mathbb{R}$, writing A_i for the ones that correspond to balls in P, and A_j for the ones that correspond to balls in

$Q \setminus P$. A point $x \in \mathbb{R}^3$ belongs to $\bigcap P$ iff $\|x\|^2 \leq A_i(x)$ for all A_i, and x does not belong to $\bigcup(Q \setminus P)$ iff $\|x\|^2 > A_j(x)$ for all A_j. Hence, for $\bigcap P \setminus \bigcup(Q \setminus P)$ to be non-empty, it is necessary that the chamber below the hyperplanes defined by the A_i and above the hyperplanes defined by the A_j exists. Recalling the formula for the number of chambers in $n+1 = 4$ dimensions (2.29), we see that for $q+1 > 4$ hyperplanes their number is less than 2^{q+1}. It follows that there is at least one subset P whose corresponding chamber is empty. This subset witnesses the non-independence of Q and can be used to start the procedure outlined in the proof of the Level-k Pie Theorem. A drawback of this procedure is the exponential size of the matrix, but it suffices to run it on a subset $Q' \subseteq Q$ of $5 \leq q+1$ balls, and to use the relation for Q' to get a relation for Q.

The above method for finding P does not work for sets Q with cardinality $q+1 \leq 4$. But here we can use the fact that Q is independent iff the nerve of the Voronoi domains restricted to the balls is the full q-simplex spanned by the centers of the $q+1$ balls. If Q is not independent, then the simplices missing from the nerve give the desired relation. To see this, we note that the full q-simplex and the mentioned nerve give two different inclusion-exclusion formulas for the union of the $q+1$ balls [Edelsbrunner, 1995b]. The difference of the two evaluates to zero and contains the intersection of the $q+1$ balls as a term.

2.7 Discussion

The main results of this chapter are short inclusion-exclusion formulas for the k-fold cover of a finite set of balls in $\mathbb{R}^n$, one based on the order-k Voronoi (or power) diagram, and the other on the k-th level in the lifted hyperplane arrangement. In addition, we have formalized the reduction to independent terms, which is essential to get effective implementations of the formulas. This work raises a number of questions we have not been able to answer.

- How big are the formulas, in terms of k, m, n, and how fast can they be computed? For constant dimension, the level-k formula gives a polynomial upper bound, but we do not know an asymptotically tight bound.

The same claim is probably not true for the order-k formula for which the reduction may take a large number of steps. Another advantage of the level-k approach is it extends to computing the volume of weighted multiple covers: assigning a real weight to every ball, we ask for the volume of the set of points covered by balls whose sum of weights exceeds a given threshold. What about shapes that are more general than balls?

- Following a general reduction argument, we see that families of simple shapes, such as ellipsoids and axes-aligned boxes, also have short inclusion-exclusion formulas for the k-fold cover. Are there polynomial-time methods to compute them?

Indeed, it is not difficult to generalize the reduction outlined in the proof of the Level-k Pie Theorem to shapes for which the cardinality of an independent collection is bounded. Starting from the exponential size formula (2.1), we can reduce the terms until they are all independent, but this approach takes exponential time. Finally, there is the less specific connection of the work in this chapter to optimal sphere arrangements that neither pack nor cover. We mention one such question:

- What is the best way to arrange equal-size balls in $\mathbb{R}^n$ if the objective is to maximize the probability that a random point is covered by exactly one ball?

Based on the application of our work and software to the SCD model of the eukaryotic cell nucleus, another different optimization criteria may be defined where the volume of the k-fold covering can be used as a primitive tool.

3 Weighted Averages

Voronoi diagrams and Delaunay triangulations have been extensively used to represent and compute geometric features of point configurations. We introduce a generalization to *poset diagrams* and *poset complexes*, which contain order-k and degree-k Voronoi diagrams and their duals as special cases. Extending a result of Aurenhammer from 1990, we show how to construct poset diagrams as weighted Voronoi diagrams of average balls.

3.1 Prior work and results

As documented by Aurenhammer [Aurenhammer, 1991], Voronoi diagrams have found applications in diverse areas of science. This includes biology, where they assist in the study of proteins in atomic resolution [Richards, 1974] as well as cell cultures on much coarser level of organization [Bock *et al.*, 2010]. Returning to atomic resolution, Voronoi diagrams have been used to derive inclusion-exclusion formulas for the volume of a union of balls; see [Kratky, 1978] in physics and [Naiman and Wynn, 1992] in statistics. In chapter 2 [Edelsbrunner and Iglesias-Ham, 2018a], we have extended these formulas to the space of points covered by at least k of the balls using order-k Voronoi diagrams [Shamos and Hoey, 1975; Tóth, 1976; Tóth, 1979] or, alternatively, degree-k Voronoi diagrams [Edelsbrunner, 1987, page 207].

In this chapter, we define cotransitive posets and use them to introduce a family of Euclidean Voronoi diagrams that includes the order-k and degree-k diagrams as special cases. A subset of the family corresponds to generalized permutahedra, as studied within algebraic geometry [A. Postnikov., 2009]. A second contribution is the construction of the diagrams in this family from weighted averages of the given points or

balls. This construction is a generalization of a result of Aurenhammer [Aurenhammer, 1990], who constructs an order-k Voronoi diagram from the k-fold averages of the given points.

Outline. Section 3.2 provides background on Voronoi diagrams and its generalization to poset diagrams. Section 3.3 studies averages of balls in the construction of poset diagrams. Section 3.4 concludes the chapter.

3.2 Poset diagrams

This section introduces a common generalization of order-k and degree-k Voronoi diagrams. We begin by recalling the definitions of these diagrams, which we give for weighted points or balls. We allow ourselves a bit of repetition from the background section in Chapter 2 for a matter of self-containment.

Voronoi diagrams. Let $B(x, r)$ be the closed ball with center $x \in \mathbb{R}^n$ and radius $r \geq 0$. Writing $B_i = B(x_i, r_i)$, we let $\mathcal{B} = \{B_1, B_2, \ldots, B_m\}$ be a finite set of balls in $\mathbb{R}^n$. The *weighted distance* from B_i is defined by the function $\pi_i : \mathbb{R}^n \to \mathbb{R}$ that maps a point x to $\pi_i(x) = \|x - x_i\|^2 - r_i^2$. For example, if $r_i = 0$, then $\pi_i(x)$ is the squared Euclidean distance from the center of B_i.

The *Voronoi domain* of B_i is the set of points for which B_i minimizes this distance:

$$\mathrm{Vor}(B_i) = \{x \in \mathbb{R}^n \mid \pi_i(x) \leq \pi_j(x), \forall j\}. \tag{3.1}$$

The *(ordinary) Voronoi diagram*, denoted as $V(\mathcal{B})$, is the collection of such domains. In the literature, these diagrams are known under several names, including *power diagrams*, *Dirichlet tessellations*, *Thiessen polygons*, and *Wigner-Seitz zones*; see also [Aurenhammer, 1991].

Let now Q be a subset of $\mathcal{B}$. Its *Voronoi domain* consists of all points that satisfy $\pi_q(x) \leq \pi_\ell(x)$ whenever $B_q \in Q$ and $B_\ell \in \mathcal{B} \setminus Q$. For an integer $1 \leq k \leq m$, the *order-k Voronoi diagram* of $\mathcal{B}$ is the collection of Voronoi domains of all subsets of k balls in $\mathcal{B}$ [Shamos and Hoey, 1975; Tóth, 1976; Tóth, 1979]. See Figure 3.1 for an example in which all radii vanish. Note that $k = 1$ gives the ordinary Voronoi diagram. We can further subdivide the Voronoi domain of Q depending on which of its balls maximizes

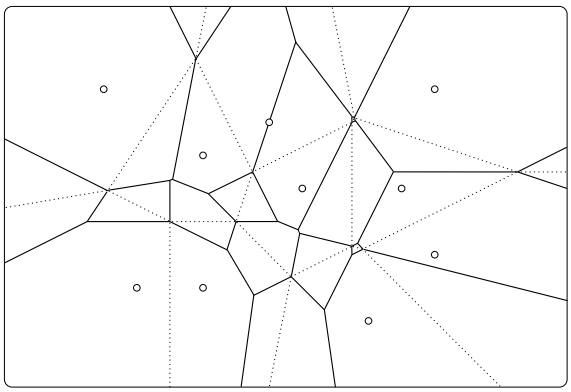

Figure 3.1: The solid lines show the order-2 Voronoi diagram, and the solid together with the dotted lines show the degree-2 Voronoi diagram of the points.

the weighted distance. If we do this for all domains in the order-k diagram, we get the *degree-k Voronoi diagram* studied for example in [Edelsbrunner, 1987, Exercise 13.27]; see again Figure 3.1. It decomposes $\mathbb{R}^n$ into regions within which the same ball realizes the k-smallest weighted distance.

Cotransitive posets. We further generalize the notion of Voronoi diagram using posets. Let $U = \{u_1, u_2, \ldots, u_m\}$ be a finite set of nodes and recall that a *partial order* is a relation on U determined by a set of pairs, $\preceq_U \subseteq U \times U$, that is reflexive, antisymmetric, and transitive, this means:

(i) $u_i \preceq u_i$ for every $u_i \in U$;

(ii) $u_i \preceq u_j$ and $u_j \preceq u_i$ implies $i = j$;

(iii) $u_i \preceq u_j$ and $u_j \preceq u_k$ implies $u_i \preceq u_k$.

We write $u_i \preceq u_j$ whenever (u_i, u_j) is an ordered pair in $\preceq_U$ and $u_i \prec u_j$ if $u_i \preceq u_j$ and $u_i \neq u_j$. Nodes u_i and u_j are *comparable* if $u_i \preceq u_j$ or $u_j \preceq u_i$. Otherwise, they are *incomparable*, which we denote as $u_i \not\sim u_j$. A *chain* of a *partially ordered set*, $(U, \preceq_U)$, is a subset of U in which any two nodes are comparable, and an *antichain* is a subset of U in which any two nodes are incomparable. We say $\preceq_U$ is *cotransitive* if:

(iv) $u_i \not\sim u_j$ and $u_j \not\sim u_k$ implies $u_i \not\sim u_k$.

If two antichains in a cotransitive partial order have a non-empty intersection, then their union is also an antichain. It follows that the maximal antichains partition U. It is

therefore possible to order the maximal antichains as

$$U = C_1 \sqcup C_2 \sqcup \ldots \sqcup C_s, \tag{3.2}$$

such that $\preceq_U = \bigcup_{i<j} C_i \times C_j$. Indeed, the existence of such a partition characterizes cotransitive partial orders.

Domains and diagrams. Let $\mathcal{B}$ be a set of m balls in $\mathbb{R}^n$ and $\preceq_U \subseteq U \times U$ the partial order of a cotransitive poset of m nodes, as before. The *poset domain* of a permutation $\gamma\colon [m] \to [m]$ is the set of points $x \in \mathbb{R}^n$ such that the weighted distances of x from the balls is consistent with the partial order:

$$\mathrm{Vor}^{\preceq_U}(\gamma) = \{x \in \mathbb{R}^n \mid u_i \preceq u_j \Rightarrow \pi_{\gamma(i)}(x) \leq \pi_{\gamma(j)}(x)\}. \tag{3.3}$$

The *poset diagram* of $\mathcal{B}$ and $\preceq_U$, denoted as $\mathrm{V}^{\preceq_U}(\mathcal{B})$, is the set of poset domains. This diagram shares the fundamental properties with the Voronoi diagram of the balls.

Lemma 5 (Structure Lemma)**.** *Let $\mathcal{B}$ be a set of m balls in $\mathbb{R}^n$ and $\preceq_U$ a cotransitive partial order on m nodes.*

(i) The $\mathrm{Vor}^{\preceq_U}$ of a permutation $\gamma\colon [m] \to [m]$ is either empty or a closed convex polyhedron.

(ii) The $\mathrm{Vor}^{\preceq_U}$ domains for two different permutations have pairwise disjoint interiors.

(iii) Every point $x \in \mathbb{R}^n$ belongs to the $\mathrm{Vor}^{\preceq_U}$ of at least one permutation.

Proof. (i) is clear from the definition since every inequality of the form $\pi_{\gamma(i)}(x) \leq \pi_{\gamma(j)}(x)$ defines a closed half-space.

(ii) holds because $\preceq_U$ is transitive as well as cotransitive, which implies that two different permutations either define the same set of inequalities, or at least one inequality is reversed. In the latter case, the two domains lie on different sides of the corresponding bisector.

(iii) follows from the fact that every ordering of the m balls is consistent with the partial order for at least one permutation. □

Examples. Fix an integer $1 \leq k \leq m$ and consider the following four cotransitive partial orders on m nodes:

$$\preceq_1 = \{u_1 \preceq u_j \mid 1 \leq j \leq m\}; \tag{3.4}$$

$$\preceq_2 = \{u_i \preceq u_j \mid 1 \leq i \leq k < j \leq m\}; \tag{3.5}$$

$$\preceq_3 = \{u_i \preceq u_k \preceq u_j \mid 1 \leq i \leq k \leq j \leq m\}; \tag{3.6}$$

$$\preceq_4 = \{u_i \preceq u_j \mid 1 \leq i \leq j \leq m\}. \tag{3.7}$$

We note that $\mathrm{V}^{\preceq_1}(\mathcal{B})$ is the ordinary Voronoi diagram, $\mathrm{V}^{\preceq_2}(\mathcal{B})$ is the order-k Voronoi diagram, and $\mathrm{V}^{\preceq_3}(\mathcal{B})$ is the degree-k Voronoi diagram, see Figure 3.2. The fourth poset consists of a single chain, in which case $\mathrm{V}^{\preceq_4}(\mathcal{B})$ is the collection of chambers in the arrangement formed by all bisectors of the balls. It is the finest of all poset

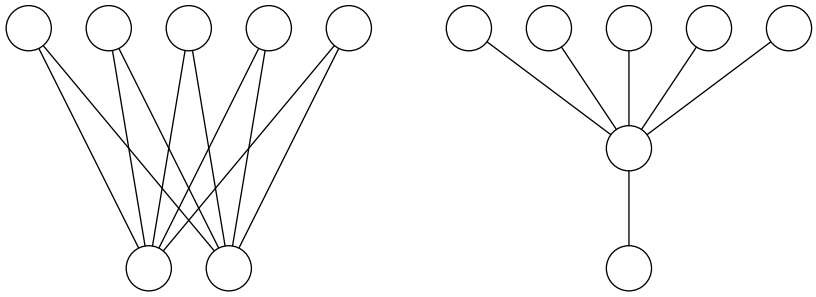

Figure 3.2: The transitive reductions of two cotransitive posets giving rise to the order-2 Voronoi diagram of seven balls on the *left* and to the degree-2 Voronoi diagram of the same number of balls on the *right*.

diagrams. Indeed, every poset diagram of $\mathcal{B}$ can be obtained by coarsening $\mathrm{V}^{\preceq_4}(\mathcal{B})$. Referring to the decomposition into maximal antichains in (3.2), we can describe the poset diagram in general as follows. Letting k_i be the cardinality of the i-th antichain, the diagram decomposes $\mathbb{R}^n$ into the order-k_1 Voronoi domains of the m balls, it refines each domain into the order-k_2 Voronoi domains of the remaining $m - k_1$ balls, and repeats until refining the domain into the order-k_{i-1} Voronoi domains of the remaining $k_{i-1} + k_i$ balls.

3.3 Average balls

In this section, we construct the poset diagrams by taking averages of the balls in $\mathcal{B}$. We begin with the introduction of a vector space structure of the set of all balls,

including those with negative squared radii.

Vector space of balls. We follow Pedoe [Pedoe, 1988, Chapter IV], who introduced the vector space to study the geometry of circles in the plane or spheres in higher-dimensions. In particular, we represent the ball $B(x,r)$ by the point $b(x,r) = (x, \|x\|^2 - r^2)$ in $\mathbb{R}^{n+1}$. To have a bijection between the set of balls in $\mathbb{R}^n$ and the set of points in $\mathbb{R}^{n+1}$, we let r^2 range over all real numbers or, equivalently, we let r range over all non-negative real numbers and all positive multiples of the imaginary unit, a set we denote as $\sqrt{\mathbb{R}}$. Borrowing the vector space structure of $\mathbb{R}^{n+1}$, we have a vector space of balls in which addition and multiplication with scalars make sense. More formally, if B_1, B_2 are two balls with corresponding points b_1, b_2, and λ_1, λ_2 are real numbers, then $B_0 = \lambda_1 B_1 + \lambda_2 B_2$ is defined such that the corresponding point satisfies $b_0 = \lambda_1 b_1 + \lambda_2 b_2$ in $\mathbb{R}^{n+1}$. From the centers x_1, x_2 and squared radii r_1^2, r_2^2 of B_1, B_2, we can compute the center and squared radius of B_0 as:

$$x_0 = \lambda_1 x_1 + \lambda_2 x_2, \tag{3.8}$$

$$r_0^2 = \|x_0\|^2 - \lambda_1\left(\|x_1\|^2 - r_1^2\right) - \lambda_2\left(\|x_2\|^2 - r_2^2\right). \tag{3.9}$$

Assuming $\lambda_1 + \lambda_2 = 1$, we can plug these expressions of the center and the squared radius into the formula for the weighted distance of a point $x \in \mathbb{R}^n$ from B_0 and get

$$\pi_0(x) = \lambda_1 \pi_1(x) + \lambda_2 \pi_2(x). \tag{3.10}$$

Affine combinations. This is an interesting conclusion worth generalizing. For this purpose, we recall that a *linear combination* is a ball $B_0 = \sum_{i=1}^k \lambda_i B_i$. It is an *affine combination* if $\sum_i \lambda_i = 1$, and it is a *convex combination* if, in addition, $0 \leq \lambda_i$ for all i. For affine combinations, the weighted distance satisfies a relation that generalizes (3.10):

Lemma 6 (Weighted Distance Lemma)**.** *Let $B_0 = \sum_{i=1}^k \lambda_i B_i$ with $\sum_{i=1}^k \lambda_i = 1$. Then $\pi_0(x) = \sum_{i=1}^k \lambda_i \pi_i(x)$, for every point $x \in \mathbb{R}^n$.*

Proof. For $k = 2$, the claimed relation is the same as (3.10). For $k > 2$, we decompose the affine combination into two affine combinations of fewer than k balls each:

$$B_0' = \tfrac{1}{\lambda_2 + \ldots + \lambda_k}\left(\lambda_2 B_2 + \ldots + \lambda_k B_k\right), \tag{3.11}$$

$$B_0 = \lambda_1 B_1 + (\lambda_2 + \ldots + \lambda_k) B_0'. \tag{3.12}$$

Inductively, we get the claimed relation for the weighted distance from B_0', and combining it with (3.10), we get the claimed relation for the weighted distance from B_0. □

To understand the effect of a scalar multiplication on the weighted distance, we consider $B_{\text{org}} = (0, 0)$, and note that $\mu B_{\text{org}} = B_{\text{org}}$ for all $\mu \in \mathbb{R}$. Setting $B_0 = \lambda B_1$, we note that $B_0 = \lambda B_1 + (1 - \lambda)B_{\text{org}}$. Using (3.10), we therefore get

$$\pi_0(x) = \lambda \pi_1(x) + (1 - \lambda)\|x\|^2 \tag{3.13}$$

because $\pi_{\text{org}}(x) = \|x\|^2$. Any linear combination can be written as a scalar multiple of an affine combination, so we can get the weighted distance function from (3.13) applied to the relation given in the Weighted Distance Lemma.

Weighted averages. As proved in [Aurenhammer, 1990], the order-k Voronoi diagram of a finite set of points is the ordinary Voronoi diagram of the k-fold averages. We generalize this result, showing that every poset diagram is an ordinary Voronoi diagram, of course of a different set of balls. To construct this set, we say a function $\lambda\colon [m] \to \mathbb{R}$ is *anti-parallel* to a cotransitive partial order if $\sum \lambda(i) = 1$ and $\lambda(i) > \lambda(j)$ iff $u_i \prec u_j$. Hence, λ is constant on the nodes in an antichain, and using the ordered partition into maximal antichains (3.2), there are values $\lambda_1 > \lambda_2 > \ldots > \lambda_s$, such that $\lambda(i) = \lambda_p$ iff $u_i \in C_p$. Given $\mathcal{B}$ and $\preceq_U$, the *weighted average ball* of a permutation $\gamma\colon [m] \to [m]$ is

$$\overline{B}_\gamma = \sum_{i=1}^{m} \lambda(i) B_{\gamma(i)}, \tag{3.14}$$

and we write $\overline{\mathcal{B}} = \overline{\mathcal{B}}(\mathcal{B}, \preceq_U)$ for the set of all such weighted averages. Noting that $\overline{B}_\gamma = \overline{B}_{\gamma'}$ iff γ and γ' define the same domain, we see that the number of balls in $\overline{\mathcal{B}}$ is

$$\operatorname{card} \overline{\mathcal{B}} = \frac{m!}{\prod_{p=1}^{s} (\operatorname{card} C_p)!}. \tag{3.15}$$

The Voronoi domain generated by a weighted point may or may not be empty, which implies that the left-hand side of (3.15) is an upper bound on the number of non-empty domains in $\mathrm{V}^{\preceq \mathrm{U}}(\overline{\mathcal{B}})$.

Main result. Importantly, the poset diagram of $\mathcal{B}$ and $\preceq_U$ is equal to the ordinary Voronoi diagram of $\overline{\mathcal{B}}$.

Theorem 4 (Poset Diagram Theorem)**.** *Let $\mathcal{B}$ be a finite set of balls in $\mathbb{R}^n$, let $\preceq_U$ be a cotransitive partial order on the same number of nodes, and set $\overline{\mathcal{B}} = \overline{\mathcal{B}}(\mathcal{B}, \preceq_U)$. Then* $\mathrm{V}^{\preceq \mathrm{U}}(\mathcal{B}) = V(\overline{\mathcal{B}})$.

Proof. Fixing a permutation γ, we prove that a point x belongs to the Voronoi domain of γ, $\mathrm{Vor}^{\preceq_U}(\gamma)$, iff x belongs to the Voronoi domain of the weighted average ball, $\mathrm{Vor}(\overline{B}_\gamma)$. To see $\mathrm{Vor}^{\preceq_U}(\gamma) \subseteq \mathrm{Vor}(\overline{B}_\gamma)$, we recall that the weighted distance of x from $B_0 = \overline{B}_\gamma$ satisfies $\pi_0(x) = \sum_{i=1}^m \lambda(i)\pi_{\gamma(i)}(x)$ by Lemma 6. Assuming $x \in \mathrm{Vor}^{\preceq_U}(\gamma)$, we have $\pi_{\gamma(i)}(x) \leq \pi_{\gamma(j)}(x)$ as well as $\lambda(i) > \lambda(j)$ whenever $u_i \prec u_j$. It follows that the weighted distance to any other weighted average ball is larger. Indeed, this other weighted distance is obtained by switching some of the $\lambda(i)$. We thus go away from the global minimum, which we get by sorting the $\pi_{\gamma(i)}(x)$ and the $\lambda(i)$ in anti-parallel fashion.

Since both the $\mathrm{Vor}^{\preceq_U}(\gamma)$ and the $\mathrm{Vor}(\overline{B}_\gamma)$ domains are interior-disjoint closed convex polyhedra that cover $\mathbb{R}^n$, we have $\mathrm{Vor}^{\preceq_U}(\gamma) = \mathrm{Vor}(\overline{B}_\gamma)$ for every γ. Indeed, if $\mathrm{Vor}^{\preceq_U}(\gamma)$ domains were a strict subset of $\mathrm{Vor}(\overline{B}_\gamma)$, then there would be points in the interior of the Voronoi domain that are not covered by any $\mathrm{Vor}^{\preceq_U}$ domain. □

Geometric dual. Recall that $V(\overline{\mathcal{B}})$ has a geometric dual, namely the *Delaunay triangulation* of $\overline{\mathcal{B}}$, $D(\overline{\mathcal{B}})$. We call this Delaunay triangulation the *poset complex* of $\mathcal{B}$ and $\preceq_U$, $\mathrm{D}^{\preceq_U}(\mathcal{B})$. As shown in Figure 3.3, it has cells that are not necessarily simplicial even

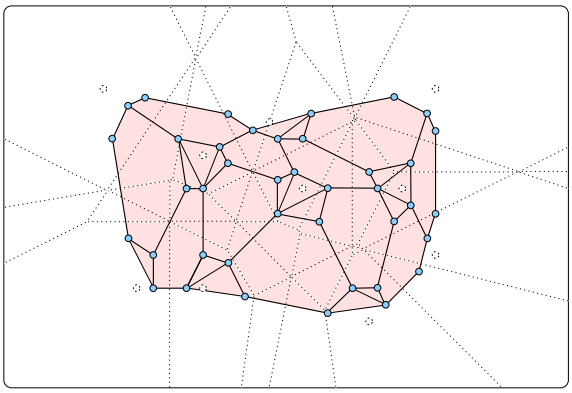

Figure 3.3: The Delaunay complex superimposed on the dotted degree-2 Voronoi diagram. Only the edges and faces corresponding to Voronoi cells visible in the window are drawn.

for generic sets $\mathcal{B}$. Specifically, a Delaunay cell is the convex hull of the centers of a maximal collection of average balls whose corresponding Voronoi regions have a given non-empty common intersection. As usual, the dimension of the common intersection of Voronoi domains and of the dual Delaunay cell are complementary, that is: they add to n.

3.4 Discussion

In this chapter, we introduce the concept of cotransitive posets to generalize Voronoi diagrams to *poset diagrams* and their dual Delaunay triangulations to *poset complexes*. This provides a general setting that includes order-k and degree-k Voronoi diagrams as well as arrangements of bisectors as special cases. Generalizing a result of Aurenhammer [Aurenhammer, 1990], we prove that each poset diagram is also the weighted Voronoi diagram of a finite set of points with real weights. Starting from lattice configurations, the sets of weighted averages often form fascinating patterns that may be worth studying independently (See Figures 3.4 and 3.5).

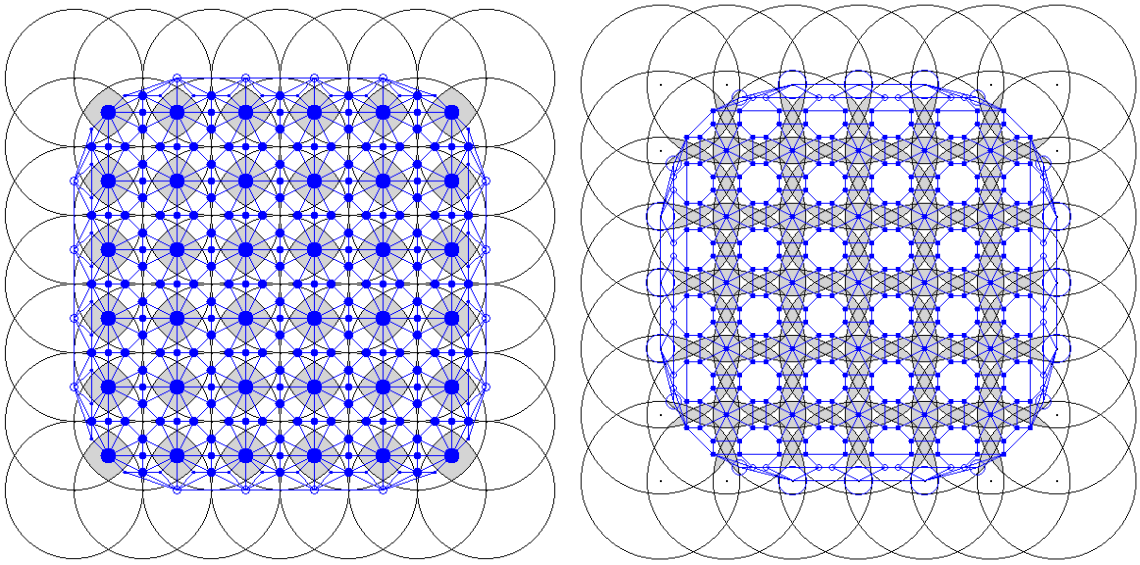

Figure 3.4: Shaded is the k-fold area for balls centered in a subset of a lattice. On top we plot the graphs of the order-k Delaunay triangulation with different size vertices representing the weight of the corresponding average points. Transparent vertices represent negative radii. On the left the 4-fold and on the right the 5-fold, both for the integer lattice.

In closing this chapter, we point out a connection between the poset diagrams and the generalized permutahedra studied in [Feichtner and Sturmfels, 2005; A. Postnikov., 2009]. Recall $\mathrm{V}^{\preceq_4}(\mathcal{B})$, which is defined by the total order. It is formed by drawing the perpendicular bisector of every pair of balls. Interpreting the resulting arrangement projectively, every chamber corresponds to a permutation as well as its reverse. For $m = n + 2$ balls, we can check that the arrangement has $\frac{m!}{2}$ chambers and thus cov-

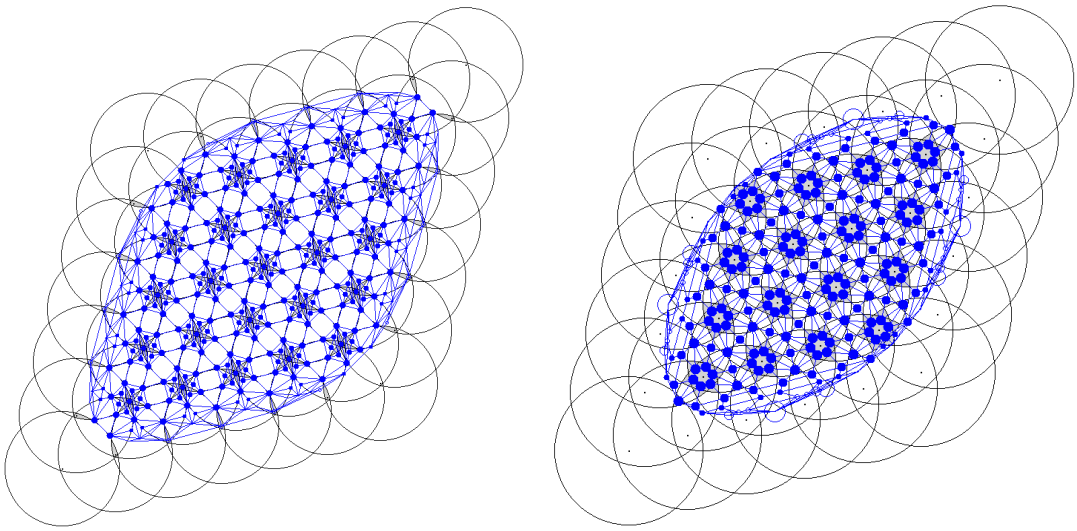

Figure 3.5: 5-fold (left) and 6-fold (right) for the hexagonal lattice.

ers all permutations. This arrangement corresponds to the permutahedron, which is a convex polytope with $m!$ vertices in $\mathbb{R}^{n+1}$. Poset diagrams obtained by coarsening

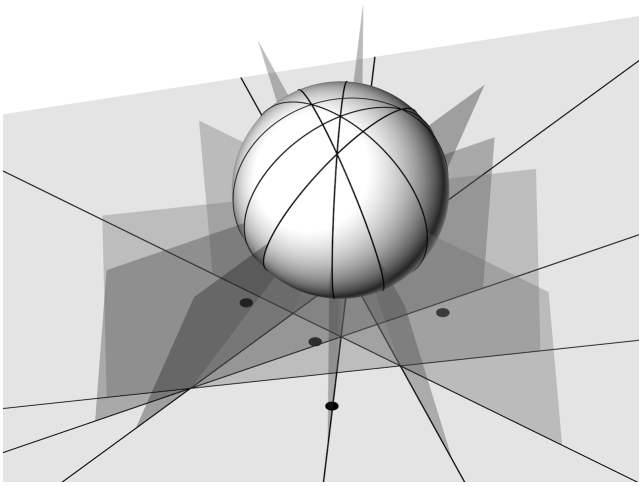

Figure 3.6: The arrangement of 6 bisectors of 4 points in the plane, and the corresponding decomposition of the unit sphere into $4! = 24$ regions[1].

the arrangement of bisectors correspond to generalized permutahedra as defined in the mentioned papers. Referring to Figure 3.6, we briefly describe the construction in $n = 2$ dimensions. Starting with 4 points in $\mathbb{R}^2$, we draw 6 lines, each the perpendicular bisector of two points. Identifying $\mathbb{R}^2$ with the plane $x_3 = -1$ in $\mathbb{R}^3$, we extend each lines to a plane passing through the origin. The 6 planes cut the unit sphere into 24 regions, each corresponding to a unique permutation of the 4 points. To get a poly-

[1]Special thanks to Hubert Wagner for his help in creating the 3D plot using the 3DsMax software.

tope with the combinatorial structure of the 3-dimensional permutahedron, we take the Minkowski sum of 6 line segments, each normal to one of the planes. We feel that this geometric view sheds new light on the family of generalized permutahedra. It would be useful to recast our main result – the Poset Diagram Theorem – in terms of generalized permutahedra and generalizations of them.

4 Relaxed packing

In this chapter we find optimal configurations of balls lying between the traditional packing and covering settings. The results are accompanied with extensive computations realized in the support software Maple [MAPLE]. We provide the relevant details in appendices at the end of the thesis.

4.1 Prior work and results

Looking for optimal arrangement of balls in the relaxed packing setting we have consider three main approaches. First, in Section 4.2, we allow configurations of spheres where the overlap is limited by a parameter, and the quality of the configuration is measured by its *density*, which is the expected number of balls that contain a randomly selected point. The overlap is measured in two different ways: by the *distance-based overlap*, which is simply a linear function of the distance between two sphere centers and has been used for the analysis in [Uhler and Wright., 2013], and the more intuitive *volume-based overlap*, which is based on the volume in the intersection of balls. Using the *distance-based overlap*, we show that the FCC lattice results in the densest arrangement regardless of the amount of allowed overlap. Computational experiments using the *volume-based overlap* show that for small values of the parameter, the highest density is attained for the FCC lattice, and that for large values, the highest density is attained for the BCC lattice. These experiments are limited to a 1-parameter family of lattices (see [Edelsbrunner and Kerber, 2011]) — the same considered in Section 4.4 of this chapter — and it is remarkable that there is a sharp transition, with none of the other lattices challenging the dominance of FCC and BCC. This family of lattices is particularly interesting, since it contains the optimal packing lattices in dimensions 2

and 3 and the optimal covering lattices in dimensions 2–5.

A similar setting was considered in [Bezdek and Lángi, 2015] but for different reasons. To study the packing of balls, the authors give upper bounds on the volume of the union in which every ball is thickened by a parameter. Equivalently, the (thickened) balls are packed softly, allowing for a limited overlap controlled by the parameter. The bounds are proved for packings in $\mathbb{R}^n$ and are not limited to lattices. Soft packing is also the natural setting for modeling physical processes at the nanoscale. For example, Radin [C.ÑRADIN., 1981] considers finitely many interacting particles governed by a potential function defined for pairs that penalizes distances below a threshold while giving preference to particles in close contact but above the distance threshold. In two dimensions, the optimal configuration was found to be a subset of the hexagonal lattice.

As a second approach, we introduce a new measure that favors configurations between packing and covering without explicit constraints on the allowed overlap. Specifically, we measure a configuration by the probability of a randomly selected point to belong to exactly one ball. Since empty space and overlap between disks are both discouraged, the optimum lies necessarily between packing and covering. We restrict our attention to equal-sized disks in $\mathbb{R}^2$, whose centers form a lattice, leaving three and higher dimensions as well as nonlattice configurations as open problems. The main result is the non-surprising fact, that this measure attains its maximum for the hexagonal grid [Balázs, 1973], and even nonlattice configurations cannot increase the measure [Blind and Blind., 1986]. In the optimal configuration each disk overlaps the six neighboring circles in 30° arcs. For obvious reasons, we call this the 12-*hour clock configuration*. While preparing the final version of the paper containing this result, we have learnt that László Fejes Tóth in his book on *Regular Figures* introduced the same measure and conjectured that the 12-hour clock configuration is optimal among all configurations in the plane. He mentions that J. Balázs proved the conjecture for lattices [Tóth., 1964, page 195] and therefore acknowledge their result as a reference here. We have found later the publication in german, and we are unsure whether we rediscover Balázs' proof or we give a different proof for the same result.

In a third approach we extend the previous result to 3D (Section 4.4) restricting our attention to equal balls centered at points of a lattice. Writing φ_i for the probability that

a randomly selected point lies in at least i balls, the density is $\delta = \sum_{i\geq 1} \varphi_i$. Departing from the previous results and also [Bezdek and Lángi, 2015], we introduce the *soft density*, $\delta_1 = \varphi_1 - \sum_{i\geq 2} \varphi_i$, which penalizes for gaps in the coverage but also for overlaps among the balls. Following [Edelsbrunner and Kerber, 2011], we focus on the mentioned 1-parameter *diagonal family* of lattices obtained by compressing or stretching the integer lattice along the diagonal direction. We use the unimodality of the measure to prove that in $\mathbb{R}^3$ the FCC lattice with balls of radius $1.090\ldots$ times the packing radius maximizes the soft density at $\delta_1 = 0.844\ldots$. The proof is a detailed study of all lattices in the diagonal family, giving analytic expressions for the maximum soft density over distortion intervals that cover the entire family. Crucial ingredients to the proof are the use of Brillouin zones, a new result about their long-range behavior in lattices, and the unimodality of the soft density.

The interested reader can find a wealth of further information and references on packing and covering in [Conway and Sloane, 1999; Tóth, 1953]. To avoid ambiguity, we mention that in the mathematical literature, a *packing* refers to a configuration of balls (hard spheres) with disjoint interiors, while a *covering* is one in which the balls cover the entire space without gaps. The traditional measure of quality is the density as defined above.

Outline. In Section 4.2 we study two natural choices of overlap measures and obtain the optimal soft-lattice packings restricting the overlap by a threshold. In Section 4.3 we study relaxed packing configurations of equal-sized disks in the Euclidean plane that neither pack nor cover. Measuring the quality by the probability that a random point lies in exactly one disk, we show that the regular hexagonal grid gives the maximum among lattice configurations. We then extend this unparameterized setting to 3D in Section 4.4, and conclude the chapter with the discussion in Section 4.5.

4.2 Packing with limited overlap

In this section we discuss two different measures of overlap in sphere arrangements, the *distance-based overlap* (also used in [Uhler and Wright., 2013]) and the *volume-based overlap*. Using the distance-based overlap we show that the FCC lattice re-

sults in the densest arrangement in the considered family of lattices, regardless of the amount of allowed overlap. In the case of the more complicated volume-based overlap measure, we prove that in 2D the hexagonal lattice remains optimal for any overlap. However, in 3D we show that the best choice depends on the allowed overlap and we provide numerical evidence that the optimal lattice is always either the FCC or the BCC lattice.

4.2.1 Measures of Sphere Arrangements

As before we let $B(x, r)$ denote the closed ball of radius r and center x. In particular we call the ball centered at the origin $B_{\mathrm{org}} = B(0, r)$. Let Λ denote a lattice; w.l.o.g., we assume that the origin is a lattice point. We let $\mathrm{Vor}(B_{\mathrm{org}})$ denote the Voronoi cell of the origin consisting of all points that are closer to the origin than to any other lattice point. The Voronoi cells of other lattice points are just translations of $\mathrm{Vor}(B_{\mathrm{org}})$ and they tessellate $\mathbb{R}^n$.

A first measure of a sphere arrangement is the *density*. It is defined as the number of spheres that contain an average point and can be rephrased as

$$\delta(\Lambda, r) \;=\; \frac{\mathrm{vol}[B_{\mathrm{org}}]}{\mathrm{vol}[\mathrm{Vor}(B_{\mathrm{org}})]}. \tag{4.1}$$

We define the *union* of a sphere arrangement to be

$$\mathcal{U}(\Lambda, r) \;=\; \frac{\mathrm{vol}[B_{\mathrm{org}} \cap \mathrm{Vor}(B_{\mathrm{org}})]}{\mathrm{vol}[\mathrm{Vor}(B_{\mathrm{org}})]}. \tag{4.2}$$

The $\mathcal{U}$ denotes what fraction of the Voronoi cell is covered by the ball of radius r. Looking at the whole space, it also denotes what fraction of $\mathbb{R}^n$ is covered by the union of all balls of radius r. This follows because the Voronoi cells tessellate $\mathbb{R}^n$ and from the following statement:

Proposition 5. *Let p be a point that belongs to the Voronoi cell of p_1. If p is covered by a ball $B(p_2, r)$, then p is also covered by $B(p_1, r)$.*

A third measure of a sphere arrangement is the *overlap*. We define two versions, the *distance-based overlap* and the *volume-based overlap*. The *distance-based overlap* was used to model the spatial organization of chromosomes in [Uhler and Wright.,

2013] and is defined as the diameter of the largest sphere that can be inscribed into the intersection of two spheres, i.e.:

$$\mathcal{O}_{\mathrm{dist}}(\Lambda, r) \;=\; \max\left(\frac{2r - \min_{\ell \in \Lambda \setminus \{0\}}(\|\ell\|)}{2r}, 0\right). \tag{4.3}$$

A less simplified measure of overlap is the *volume-based overlap*, which we define as the fraction of a sphere that expands outside its Voronoi cell:

$$\mathcal{O}_{\mathrm{vol}}(\Lambda, r) = \frac{\mathrm{vol}[B_{\mathrm{org}}] - \mathrm{vol}[B_{\mathrm{org}} \cap \mathrm{vol}[\mathrm{Vor}(B_{\mathrm{org}})]]}{\mathrm{vol}[\mathrm{Vor}(B_{\mathrm{org}})]}. \tag{4.4}$$

This value is equivalent to the fraction of all other spheres expanding into a Voronoi cell (i.e., the overlap with multiplicity inside a Voronoi cell).

We refer to the unnormalized version of $\mathcal{O}_{\mathrm{vol}}$ as the *excess*:

$$\mathcal{E}(\Lambda, r) = \mathrm{vol}[B_{\mathrm{org}}] - \mathrm{vol}[B_{\mathrm{org}} \cap \mathrm{vol}[\mathrm{Vor}(B_{\mathrm{org}})]]. \tag{4.5}$$

We observe that $\delta(\Lambda, \cdot)$, $\mathcal{U}(\Lambda, \cdot)$ and $\mathcal{O}(\Lambda, \cdot)$ (for both overlap measures) are non-negative, monotonously increasing functions with $\mathcal{U}(\Lambda, \cdot)$ upper bounded by 1. The upper bound for $\mathcal{U}$ is reached exactly at the covering radius, the maximal distance of the origin to the boundary of $\mathrm{Vor}(B_{\mathrm{org}})$. The lower bound for $\mathcal{O}$ is reached exactly at the packing radius, the minimal distance of the origin to the boundary of $\mathrm{Vor}(B_{\mathrm{org}})$. Also, it holds that

$$\mathcal{O}_{\mathrm{vol}}(\Lambda, r) \;=\; \delta(\Lambda, r) - \mathcal{U}(\Lambda, r). \tag{4.6}$$

Building upon these measures of sphere arrangements we can now define a relaxed packing and covering quality when allowing overlap and uncovered space, respectively. By fixing a threshold $\omega \in \mathbb{R}_{\geq 0}$, we define the *relaxed packing quality* of a lattice as

$$\mathcal{Q}_{\mathrm{pack}}(\Lambda, \omega) \;=\; \max_{r \geq 0} \left\{ \delta(\Lambda, r) \mid \mathcal{O}(\Lambda, r) \leq \omega \right\}.$$

The goal is to find the lattice that maximizes $\mathcal{Q}_{\mathrm{pack}}$. Note that for $\omega = 0$, this is equivalent to the classical sphere packing problem: We want to cover as much space as possible by balls without overlap. It is known that in dimension 3 the FCC lattice is the optimal solution to this problem.

Lemma 7. *The FCC lattice is not optimal w.r.t. $\mathcal{Q}_{\mathrm{pack}}$ for some value of ω when measuring overlap by $\mathcal{O}_{\mathrm{vol}}$.*

Proof. Let ω be the overlap of the BCC lattice when choosing the radius to be its covering radius. Note that the density of this covering is $1+\omega$ by (4.6). Assume that the FCC lattice attains the same density for ω. Then, again by (4.6), the union must be 1, so the FCC lattice yields a sphere covering with the same density as the BCC lattice. But this is a contradiction to the well-known fact that the FCC covering density is strictly larger than the BCC covering density. □

Interestingly, we will prove in Section 4.2.2 that the FCC lattice is in fact optimal for all values of ω when measuring overlap by $\mathcal{O}_{\mathrm{dist}}$. Similarly, we can define a *relaxed covering quality* as

$$\mathcal{Q}_{\mathrm{cover}}(\Lambda,\omega) \;=\; \min_{r\geq 0}\left\{\delta(\Lambda,r) \mid 1-\mathcal{U}(\Lambda,r)\leq\omega\right\}.$$

In words, we want as little overlap as possible while allowing only a certain amount of uncovered space. Note that for $\omega=0$, this is equivalent to the classical covering problem: We want to cover the whole space by balls minimizing the density. Similarly as in Lemma 7 we can prove that the BCC lattice is not optimal w.r.t. $\mathcal{Q}_{\mathrm{cover}}$ for all values of ω when measuring overlap by $\mathcal{O}_{\mathrm{vol}}$. However, the BCC lattice is optimal for all values of ω when measuring overlap by $\mathcal{O}_{\mathrm{dist}}$ as we will see in Section 4.2.2. For brevity, we concentrate on $\mathcal{Q}_{\mathrm{pack}}$; our analysis easily extended to $\mathcal{Q}_{\mathrm{cover}}$ with minor changes.

From now on, we focus on lattices Λ_ε given by a diagonal distortion of the integer lattice in $\mathbb{R}^n$ by the distortion parameter $\varepsilon>0$. The lattice Λ_ε is defined by mapping each unit vector $u_i\in\mathbb{R}^n$, $i=1,\ldots,n$, to

$$u_i^\varepsilon \;=\; u_i+\frac{\varepsilon-1}{n}\mathbf{1}. \tag{4.7}$$

The parameter $\varepsilon=1$ denotes no distortion. For ε from 1 to 0, every point of the integer lattice undergoes a continuous motion towards its projection onto the plane with normal vector $(1,\ldots,1)$. For $\varepsilon\geq 1$, each lattice point moves continuously in the opposite direction. For $n=2$, the hexagonal lattice corresponds to $\varepsilon=1/\sqrt{3}$ and $\varepsilon=\sqrt{3}$, and for $n=3$, the FCC lattice corresponds to $\varepsilon=2$ and the BCC lattice to $\varepsilon=1/2$; see [Edelsbrunner and Kerber, 2011] for more details. We will abuse notation and identify ε and the lattice Λ_ε in the definitions of density, overlap and packing quality: for instance, we write $\delta(\varepsilon,r)$ instead of $\delta(\Lambda_\varepsilon,r)$.

Fixing a threshold ω for the overlap, we would like to find the best lattice in the family such that $\mathcal{Q}_{\text{pack}}(\varepsilon, \omega)$ is maximized. The approach we take is to compute $\mathcal{Q}_{\text{pack}}$ for a given ε in two steps:

1. Compute the largest ball radius $r(\varepsilon, \omega)$ such that $\mathcal{O}(\varepsilon, r(\varepsilon, \omega)) \leq \omega$.

2. Compute $\mathcal{Q}_{\text{pack}}(\varepsilon, \omega) = \delta(\varepsilon, r(\varepsilon, \omega))$.

4.2.2 Distance-based overlap

In [Uhler and Wright., 2013], an algorithm was developed for finding minimum overlap configurations of N spheres (or more generally ellipsoids) packed into an ellipsoidal container. In order to get an efficient algorithm, the simplified distance-based overlap measure was used, which could be computed as a convex optimization problem. One can easily check that the problem of finding minimal overlap configurations of spheres with a certain density is equivalent to finding maximal density configurations of spheres with a certain overlap, the problem we study in this section. It was observed in a few examples (see Example 3.4 in [Uhler and Wright., 2013]) that the optimal configuration of the spheres is invariant to scaling of the radii. This is in fact an important property for the application to chromosome packing, since the exact chromatin packing density is not known and one would hope that the positioning is robust to different scalings of the chromosomes. In the following, we prove that this scaling-invariance holds in the infinite space when the sphere centers are restricted to lie on the 1-parameter distortion family defined before. In this case, the density simplifies to

$$\delta(\varepsilon, r) = \frac{\nu_n r^n}{\varepsilon}, \tag{4.8}$$

where ν_n denotes the (n-dimensional) volume of the n-dimensional unit ball. The packing radius of Λ_ε has been computed in [Edelsbrunner and Kerber, 2011] as:

$$\min_{p \in \partial \text{Vor}(B_{\text{org}})} \|p\| = \begin{cases} \frac{1}{2}\varepsilon\sqrt{n} & 0 \leq \varepsilon \leq \frac{1}{\sqrt{n+1}}, \\ \frac{1}{2}\sqrt{1 + \frac{\varepsilon^2 - 1}{n}} & \frac{1}{\sqrt{n+1}} \leq \varepsilon \leq \sqrt{n+1}, \\ \frac{1}{2}\sqrt{2}, & \sqrt{n+1} \leq \varepsilon. \end{cases} \tag{4.9}$$

Using these formulas we prove that the maximum density configuration is always attained by $\varepsilon = \sqrt{n+1}$, regardless of the allowed overlap. This corresponds to the optimal packing lattice in the family for all $n \geq 2$ and over all lattices in dimension 2 and 3. The corresponding statement for the relaxed covering quality can be found in the Appendix A.

Theorem 6. *The lattice Λ_ε which maximizes the relaxed packing quality w.r.t. $\mathcal{O}_{\text{dist}}$ is attained by $\varepsilon = \sqrt{n+1}$ independent of the value of $\omega \in [0, 1)$.*

Proof. By plugging the packing radius given in (4.9) into the definition of $\mathcal{O}_{\text{dist}}$ in (4.3), we can solve for $r(\varepsilon, \omega)$ [1]. Then plugging $r(\varepsilon, \omega)$ into the formula for the density given in (4.1) we get for the ε intervals given in (4.9):

$$\delta(\varepsilon, r(\varepsilon,\omega)) = \begin{cases} \frac{n^{\frac{n}{2}}\nu_n}{2^n(1-\omega)^n}\,\varepsilon^{n-1} \\ \frac{\nu_n}{2^n(1-\omega)^n}\,\varepsilon^{-1}\left(1+\frac{\varepsilon^2-1}{n}\right)^{\frac{n}{2}} \\ \frac{\nu_n}{2^{\frac{n}{2}}(1-\omega)^n}\,\varepsilon^{-1}. \end{cases} \tag{4.10}$$

The function $\delta(\varepsilon, r(\varepsilon, \omega))$ for $n = 3$ and $\omega = 0.5$ is shown in Figure 4.1 (left). Since $\omega < 1$, the constants in the function $\delta(\varepsilon, r(\varepsilon, \omega))$ in (4.10) are positive. By taking derivatives w.r.t. ε we find that for $0 < \varepsilon \leq 1/\sqrt{n+1}$ the density is strictly increasing for all values of ω. Similarly, for the branch $1/\sqrt{n+1} \leq \varepsilon \leq \sqrt{n+1}$ the density is strictly decreasing for $\varepsilon < 1$, achieves a minimum at $\varepsilon = 1$, and is strictly increasing for $\varepsilon > 1$, independent of the value of ω. Finally, for $\varepsilon \geq \sqrt{n+1}$ the density is strictly decreasing for all values of ω. As a consequence, the $\max_{\varepsilon>0}\ \delta(\varepsilon, r(\varepsilon, \omega))$ is obtained in one of the interval boundaries $\varepsilon \in \{\frac{1}{\sqrt{n+1}}; \sqrt{n+1}\}$.

Evaluating δ using the first and last expressions from (4.10), we get $n^{\frac{n}{2}}(n+1)^{-\frac{n-1}{2}} \leq 2^{\frac{n}{2}}(n+1)^{-\frac{1}{2}}$ for all $n \geq 2$ with equality only for $n = 2$ where both lattices equal to the hexagonal lattice. Hence, the maximum is attained by $\varepsilon = \sqrt{n+1}$. □

This proves that the sphere configuration which maximizes the density when allowing a certain overlap (measured by the distance-based overlap) is identical to the optimal packing configuration independent of the allowed overlap.

[1] Note that $\min_{\ell\in\Lambda\setminus\{0\}}(\|\ell\|) = 2 \cdot \min_{p\in\partial\text{Vor}(B_{\text{org}})} \|p\|$

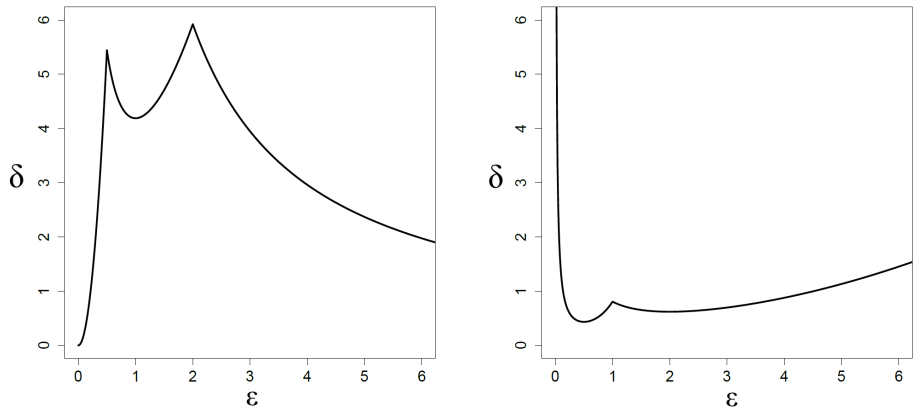

Figure 4.1: $\mathcal{Q}_{\text{pack}}$ (left) and $\mathcal{Q}_{\text{cover}}$ (right) as a function of the distortion parameter ε for $n = 3$ and $\omega = 0.5$.

4.2.3 Volume-based overlap

We next analyze $\mathcal{Q}_{\text{pack}}$ for the volume-based overlap measure in dimension 2 and 3. Because of Lemma 7, we cannot expect the same behavior as for the distance-based overlap measure from the previous section because the FCC lattice becomes worse than the BCC lattice for some value of ω. However, this does not rule out the possibility of other lattices being optimal. We perform a deeper investigation of the optimal lattice configurations, starting with the two-dimensional case.

Dimension 2

First of all, note that in dimension 2, the lattice for ε is a scaled version of the lattice for $\frac{1}{\varepsilon}$. Because of this symmetry, it suffices to study all lattices with $0 < \varepsilon \leq 1$.

Analyzing the volume-based overlap measure requires the investigation of $\text{Vor}(B_{\text{org}}) = \text{Vor}(B_{\text{org}})^{\varepsilon}$, the Voronoi cell of the origin in Λ_ε, in some detail. $\text{Vor}(B_{\text{org}})$ is bounded by six bisectors: four of them with the lattice points $\pm u_1^{(\varepsilon)}, \pm u_2^{(\varepsilon)}$, and two with the lattice points $\pm(u_1^{(\varepsilon)} + u_2^{(\varepsilon)})$. We call the bisectors of type 1 and type 2, respectively. Their distances to the origin are given by $f_1(\varepsilon)$ and $f_2(\varepsilon)$, respectively, with

$$f_1(\varepsilon) \;=\; \frac{\sqrt{\varepsilon^2+1}}{2\sqrt{2}}, \qquad f_2(\varepsilon) \;=\; \frac{\varepsilon}{\sqrt{2}}.$$

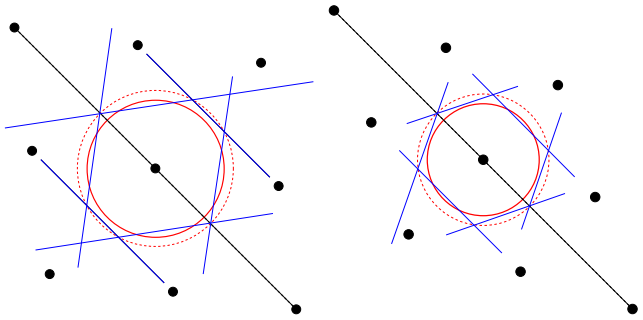

Figure 4.2: The Voronoi cell $\mathrm{Vor}(B_{\mathrm{org}})$ for two different values of $\varepsilon > \sqrt{\frac{1}{3}}$ (left) and $\varepsilon < \sqrt{\frac{1}{3}}$ (right). On the left, the bisectors of type 1 are hit first, whereas in the right bisectors of type 2 are hit first. Note that all lattice points neighboring the origin lie on a common circle around the origin.

We call $f_m(\varepsilon) = \min\{f_1(\varepsilon), f_2(\varepsilon)\}$, and $f^m(\varepsilon) = \max\{f_1(\varepsilon), f_2(\varepsilon)\}$. Note that $f_1(\varepsilon) > f_2(\varepsilon)$ if and only if $\varepsilon < \sqrt{\frac{1}{3}}$ (Figure 4.2).

There are six boundary vertices of $\mathrm{Vor}(B_{\mathrm{org}})$ and they all have the same distance to the origin, namely

$$v_1(\varepsilon) \;=\; \frac{\varepsilon^2+1}{2\sqrt{2}},$$

which agrees with the covering radius computed in [Edelsbrunner and Kerber, 2011]. As expected, $v_1(\varepsilon) \geq f^m(\varepsilon)$, with equality if and only if $\varepsilon = 1$.

With this data we can directly derive a formula for the excess $\mathcal{E}$: If $r \leq f_m(\varepsilon)$, B_{org} is completely contained in $\mathrm{Vor}(B_{\mathrm{org}})$ and the $\mathcal{E}$ equals 0. If $r \geq v_1(\varepsilon)$, B_{org} contains all boundary vertices of $\mathrm{Vor}(B_{\mathrm{org}})$ and thus all of $\mathrm{Vor}(B_{\mathrm{org}})$ (of volume ε), by convexity. In the last case where $f_m(\varepsilon) < r < v_1(\varepsilon)$, the part of B_{org} that is not in $\mathrm{Vor}(B_{\mathrm{org}})$ is the union of up to six circular segments. Their area is given by

$$A = \frac{r^2}{2}(\Theta - \sin\Theta),$$

where Θ is the angle at the origin induced by the chord that bounds the circular segment. This angle can be expressed as

$$\Theta = 2\arccos\left(\frac{d}{r}\right),$$

where d is the smallest distance of the chord to the origin. In our case, the chord is given by a bisector. Depending on the type t of the bisector, d is either equal to $f_1(\varepsilon)$

or equal to $f_2(\varepsilon)$. So we define

$$\Theta_t = \begin{cases} 0 & r < f_t(\varepsilon), \\ 2\arccos\left(\frac{f_t(\varepsilon)}{r}\right) & r \geq f_t(\varepsilon), \end{cases}$$

Since the circular segments do not intersect for any $r < v_1(\varepsilon)$ (because an intersection would imply that a boundary vertex of $\mathrm{Vor}(B_{\mathrm{org}})$ is part of B_{org}) and there are four bisectors of type 1 and two bisectors of type 2, it follows that for $0 \leq \varepsilon \leq 1$:

$$\mathcal{E} = \begin{cases} 0 & 0 \leq r \leq f_m(\varepsilon), \\ r^2(2\Theta_1 + \Theta_2 - 2\sin\Theta_1 - \sin\Theta_2) & f_m(\varepsilon) \leq r \leq v_1(\varepsilon), \\ \pi r^2 - \varepsilon & v_1(\varepsilon) \leq r\ . \end{cases}$$

Recall that the overlap $\mathcal{O}_{\mathrm{vol}}$ is simply the normalization of the excess; therefore, we obtain its formula after a division by ε. We can now prove:

Theorem 7. *In dimension 2, the lattice Λ_ε which maximizes the relaxed packing quality w.r.t. $\mathcal{O}_{\mathrm{vol}}$ is attained by the hexagonal lattice (i.e. $\varepsilon \in \{1/\sqrt{3}, \sqrt{3}\}$) independent of the value of $\omega \in \mathbb{R}_{\geq 0}$.*

Proof. Let ω and ε be fixed. Our goal is to compute $\delta(\varepsilon, r)$ where $r := r(\varepsilon, \omega)$ is chosen maximally such that $\mathcal{O}_{\mathrm{vol}}(\varepsilon, r) \leq \omega$. Observe that the maximal r is certainly at least the packing radius $f_m(\varepsilon)$. This results in the packing density, which is maximized by the hexagonal lattice. Moreover, if ω is sufficiently large to allow a covering, i.e. $\omega \geq \mathcal{O}_{\mathrm{vol}}(\varepsilon, v_1(\varepsilon))$, the maximal density is attained at the best covering. This is known to be the hexagonal lattice. So we can concentrate on the case $f_m(\varepsilon) \leq r \leq v_1(\varepsilon)$ where

$$0 \leq \mathcal{O}_{\mathrm{vol}}(\varepsilon, r) \leq \mathcal{O}_{\mathrm{vol}}(\varepsilon, v_1(\varepsilon)) = \frac{\pi(\varepsilon^2+1)^2}{8\varepsilon} - 1, \tag{4.11}$$

Consider the function $F(\varepsilon, \omega, r) := \omega - \mathcal{O}_{\mathrm{vol}}(\varepsilon, r)$, with $\mathcal{O}_{\mathrm{vol}} = \mathcal{E}/\varepsilon$, which is defined for (ω, ε, r) in the limits of interest given in (4.11). By definition, $r = r(\varepsilon, \omega)$ satisfies $F(\varepsilon, \omega, r(\varepsilon, \omega)) = 0$. The density is given by

$$\delta(\varepsilon, r(\varepsilon, \omega)) = \frac{\pi \cdot r(\varepsilon, \omega)^2}{\varepsilon},$$

which we want to maximize w.r.t. ε. This requires computing the derivative of $r(\varepsilon,\omega)$ w.r.t. ε. We do this by using the implicit function theorem

$$\frac{\partial r}{\partial \varepsilon}(\varepsilon,\omega) = -\frac{\frac{\partial F}{\partial \varepsilon}(\varepsilon,\omega,r)}{\frac{\partial F}{\partial r}(\varepsilon,\omega,r)}.$$

After some calculations we find

$$\frac{\partial\, \delta(\varepsilon, r(\varepsilon,\omega))}{\partial \varepsilon} = \begin{cases} \frac{\pi\sqrt{2r^2-\varepsilon^2}}{2\varepsilon \arccos\left(\frac{\varepsilon}{r\sqrt{2}}\right)} & f_2(\varepsilon) \le r \le f_1(\varepsilon),\ 0<\varepsilon<\frac{1}{\sqrt{3}}, \\ \frac{\pi(\varepsilon^2-1)\sqrt{8r^2-\varepsilon^2-1}}{8\varepsilon^2\sqrt{\varepsilon^2+1}\arccos\left(\frac{\varepsilon^2+1}{8r^2}\right)} & f_1(\varepsilon) \le r \le f_2(\varepsilon),\ \frac{1}{\sqrt{3}}<\varepsilon<1, \\ \frac{\sqrt{8r^2-\varepsilon^2-1}(\varepsilon^2-1)+2\varepsilon\sqrt{2r^2-\varepsilon^2}\sqrt{\varepsilon^2+1}}{4r\sqrt{\varepsilon^2+1}\left(2\arccos\sqrt{\frac{\varepsilon^2+1}{8r^2}}+\arccos\left(\frac{\varepsilon}{r\sqrt{2}}\right)\right)} & f^m(\varepsilon) \le r \le v_1(\varepsilon),\ 0<\varepsilon<1. \end{cases}$$

One can easily check that the first derivative is non-negative for any ε, except if r equals the packing radius $f_2(\varepsilon)$ corresponding to $\omega = 0$, and we know the optimal packing for this case. Similarly, the second derivative is non-positive except if r equals the packing radius $f_1(\varepsilon)$. The third derivative is zero either if $\varepsilon = \frac{1}{\sqrt{3}}$ or if r equals the covering radius $v_1(\varepsilon)$ corresponding to $\omega \ge \mathcal{O}_{\mathrm{vol}}(\varepsilon, v_1(\varepsilon))$, in which case the hexagonal lattice is optimal as we argued above. Moreover, for $r < v_1(\varepsilon)$, the derivative is increasing for $\varepsilon < \frac{1}{\sqrt{3}}$ and decreasing for $\varepsilon > \frac{1}{\sqrt{3}}$. This concludes the proof. □

Dimension 3

In three dimensions, we analyze the 3 dimensional Voronoi region $\mathrm{Vor}(B_{\mathrm{org}})$ and measure the excess $\mathcal{E}$ by an inclusion-exclusion formula for spherical caps: for small radii, $B_{\mathrm{org}} \subseteq \mathrm{Vor}(B_{\mathrm{org}})$ the excess is zero. For increasing r, B_{org} starts to intersect facets of $\mathrm{Vor}(B_{\mathrm{org}})$, and the excess is the sum of spherical caps. When r further increases, B_{org} also intersects edges of $\mathrm{Vor}(B_{\mathrm{org}})$, and the intersection of two spherical caps must be subtracted from $\mathcal{E}$. Finally, when B_{org} includes vertices of $\mathrm{Vor}(B_{\mathrm{org}})$ (but not all of $\mathrm{Vor}(B_{\mathrm{org}})$), the intersection of three spherical caps must be re-added to $\mathcal{E}$; we refer to the appendix B for further details.

Formulas for the intersection of one, two and three spherical caps have been described in [Edelsbrunner and Fu, 1994]. In combination with our analysis, they result in a branchwise-defined closed expression for $\mathcal{O}_{\mathrm{vol}}(\varepsilon, r)$. We have computed these expressions using the computer algebra system [MAPLE].[2] A 3-dimensional plot of the

[2] http://www.maplesoft.com

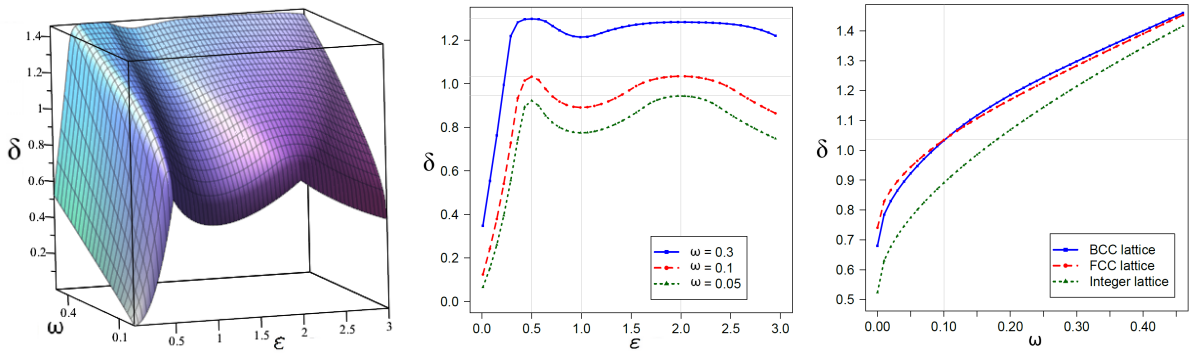

Figure 4.3: Surface plot of $\mathcal{Q}_{\text{pack}}(\varepsilon, \omega)$ (left), slices through the surface $\mathcal{Q}_{\text{pack}}$ for $\omega = 0.05$, 0.1 and 0.3 (middle), and slices through the surface $\mathcal{Q}_{\text{pack}}$ for the BCC lattice, the integer lattice and the FCC lattice (right).

function $\mathcal{Q}_{\text{pack}}(\varepsilon, \omega)$ is shown in Figure 4.3 (left). In Figure 4.3 (middle and right) we highlight specific slices through the 3-dimensional plot to better explain the behavior. Figure 4.3 (middle) shows $\mathcal{Q}_{\text{pack}}(\varepsilon, \omega)$ for three different values of ω. We can observe that the FCC lattice ($\varepsilon = 2$) is indeed optimal for small values of allowed overlap ω. When $\omega = 0.1$, the BCC ($\varepsilon = 0.5$) and the FCC lattice achieve approximately the same density, namely $\delta = 1.03$. Interestingly, for larger values of ω the BCC lattice attains the maximal density and surpasses the FCC lattice. Also observe that both lattices always achieve a better relaxed packing quality than the integer lattice ($\varepsilon = 1$). Looking at the density of the FCC and the BCC lattice depending on ω in Figure 4.3 (right), we can note that there is indeed only one switch of optimality (at $\omega \approx 0.1$).

Our analysis indicates that the FCC and the BCC lattice are always locally optimal configurations, and no other lattice from the family yields a better packing, independently of the allowed overlap. The natural next step would be to prove our observation. This problem can in theory be tackled with the same approach that we used in Section 4.2.3 in the $2D$ case by relating the derivative of $\mathcal{Q}_{\text{pack}}(\varepsilon, \omega)$ to the partial derivatives of $\mathcal{O}_{\text{vol}}$ using the implicit function theorem. For small values of ω, we were able to verify the claim, that is, prove monotonicity of the function in all branches with a substantial amount of symbolic computations. However, as soon as the expression for $\mathcal{O}_{\text{vol}}$ involves intersections of 2 and 3 spherical caps, the derivatives seem to become too complicated to be handled analytically.

4.3 Soft disc packing

The main result of this section is the following,

Theorem 8 (Main)**.** *Among all lattice configurations in $\mathbb{R}^2$, the regular hexagonal grid in which each disk overlaps the six neighboring circles in 30° arcs maximizes the probability that a random point lies exactly in one disk.*

Maximizing the given probability, we naturally favor configurations between the traditional packing and covering without the explicit use of any constraining parameter.

4.3.1 Background

In this section, we introduce notation for lattices, Voronoi domains, and Delaunay triangulations in $\mathbb{R}^2$. We allow ourselves a bit of repetition from the background sections in other chapters for a matter of self-containment.

Lattices. Depending on the context, we interpret an element of $\mathbb{R}^2$ as a point or a vector in the plane. Vectors $a_1, a_2 \in \mathbb{R}^2$ are *linearly independent* if $k_1 a_1 + k_2 a_2 = 0$ implies $k_1 = k_2 = 0$. A *lattice* is defined by two linearly independent vectors, $a_1, a_2 \in \mathbb{R}^2$, and consists of all integer combinations of these vectors:

$$\Lambda(a_1, a_2) = \{k_1 a_1 + k_2 a_2 \mid k_1, k_2 \in \mathbb{Z}\}. \tag{4.12}$$

Its *fundamental domain* is the parallelogram of points $k_1 a_1 + k_2 a_2$ with real numbers $0 \leq k_1, k_2 \leq 1$. Writing $\|a_1\|$ for the length of the vector and γ for the angle between a_1 and a_2, the area of the fundamental domain is $\det \Lambda(a_1, a_2) = \|a_1\| \|a_2\| \sin(\gamma)$. The same lattice is generated by different pairs of vectors, and we will see shortly that at least one of these pairs defines a non-obtuse triangle. We will be more specific about this condition shortly, as it is instrumental in our proof of the optimality of the regular hexagonal grid.

Voronoi domain. Given a lattice Λ, the *Voronoi domain* of a point $p \in \Lambda$ is the set of points for which p is the closest:

$$\mathrm{Vor}(p) = \{x \in \mathbb{R}^2 \mid \|x - p\| \leq \|x - q\|, \forall q \in \Lambda\}. \tag{4.13}$$

It is a convex polygon that contains p in its interior. Any two Voronoi domains have disjoint interiors but may intersect in a shared edge or a shared vertex. The lattice looks the same from every one of its points, which implies that all Voronoi domains are translates of each other: $\mathrm{Vor}(p) = p + \mathrm{Vor}(0)$. Similarly, central reflection through the origin preserves the lattice, which implies that $\mathrm{Vor}(0)$ is centrally symmetric.

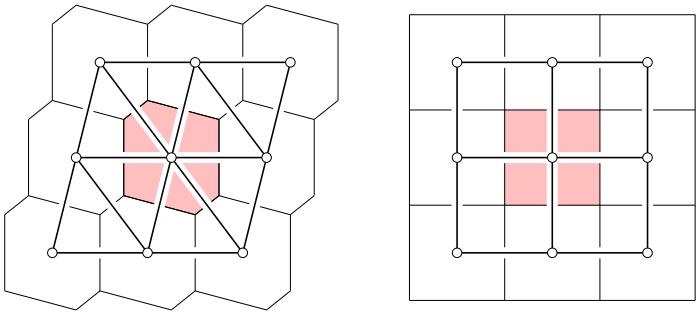

Figure 4.4: A primitive Voronoi diagram on the *left*, and a non-primitive Voronoi diagram on the *right*. The Delaunay triangulations are superimposed.

The *Voronoi diagram* of Λ is the collection of Voronoi domains of its points. It is *primitive* if the maximum number of Voronoi domains with non-empty common intersection is 3. In this case, the Voronoi domain is a centrally symmetric hexagon; see Figure 4.4. In the non-primitive case, there are generators that enclose a right angle, and the Voronoi domains are rectangles. To the first order of approximation, the area of any sufficiently simple and sufficiently large subset of $\mathbb{R}^2$ is the number of lattice points it contains times the area of $\mathrm{Vor}(0)$. Similarly, it is the number of lattice points times the area of the fundamental domain. It follows that the area of $\mathrm{Vor}(0)$ is equal to $\det \Lambda$.

Packing and covering. Like before, for $\varrho > 0$, we write $B(p, \varrho)$ for the closed disk with center p and radius ϱ. The *packing radius* is the largest radius, r_Λ, and the *covering radius* is the smallest radius, R_Λ, such that $B(0, r_\Lambda) \subseteq V(0) \subseteq B(0, R_\Lambda)$. The *density* of the configuration of disks with radius ϱ centered at the points of Λ is the area of a disk divided by the area of the Voronoi domain:

$$\delta_\Lambda(\varrho) = \tfrac{\varrho^2 \pi}{\det \Lambda}. \tag{4.14}$$

It is also the expected number of disks containing a random point in $\mathbb{R}^2$. The *packing density* is $\delta_\Lambda(r_\Lambda)$, which is necessarily smaller than 1. It is maximized by the regular hexagonal grid, H, for which we have $\delta_H(r_H) = 0.906\ldots$. The *covering density* is

$\delta_\Lambda(R_\Lambda)$, which is necessarily larger than 1. It is minimized by the regular hexagonal grid for which we have $\delta_H(R_H) = 1.209\ldots$. More generally, it is known that H maximizes the density among all configuration of congruent disks whose interiors are pairwise disjoint [Thue, 1910], and it minimizes the density among all configurations that cover the entire plane [Kershner, 1939]. Elegant proofs of both optimality results can be found in Fejes Tóth [Tóth, 1953].

Delaunay triangulations. Drawing a straight edge between points p and q in Λ iff $\mathrm{Vor}(p)$ and $\mathrm{Vor}(q)$ intersect along a shared edge, we get the *Delaunay triangulation* of Λ. In the primitive case, the edges decompose the plane into triangles. Among the six triangles sharing 0 as a vertex, three are translates of each other and, going around 0, they alternate with their central reflections. It follows that all six triangles are congruent and, in particular, they have equally large circumcircles that all pass through 0. Since their centers are vertices of the Voronoi domain of 0, we have the following result.

Lemma 8 (Inscribed Voronoi Domain)**.** *The vertices of* $\mathrm{Vor}(0)$ *all lie on the circle bounding* $B(0, R_\Lambda)$*.*

The discussion above proves the Inscribed Voronoi Domain Lemma in the primitive case. It is also true in the simpler, non-primitive case in which $\mathrm{Vor}(0)$ is a rectangle. Returning to the primitive case, we note that the two angles opposite to a shared edge in the Delaunay triangulation add up to less than $180°$. In a lattice, these two angles are the same and therefore both acute. The two types of triangles in the Delaunay triangulation of a lattice can be joined across a shared edge in three different ways. We can therefore make the same argument three times and conclude that all angles are less than $90°$. A slightly weaker bound holds in the non-primitive case.

Lemma 9 (Non-obtuse Generators)**.** *Every lattice* Λ *in* $\mathbb{R}^2$ *has vectors* $a_1, a_2 \in \mathbb{R}^2$ *with* $\Lambda = \Lambda(a_1, a_2)$ *such that*

(i) in the primitive case $0, a_1, a_2$ *are the vertices of an acute triangle,*

(ii) in the non-primitive case $0, a_1, a_2$ *are the vertices of a non-obtuse triangle with a right angle at* 0*.*

Assuming a_1, a_2 satisfy the Non-obtuse Generators Lemma, the triangle $0a_1a_2$ has edges of length $\|a_1\|$, $\|a_2\|$, and $\|a_3\| = \|a_1 - a_2\|$. In the non-primitive case (ii), $\|a_1\|$ and $\|a_2\|$ are the lengths of the sides of the rectangle $\mathrm{Vor}(0)$, and $\|a_3\|$ is the length of a diagonal. We have $\|a_3\|^2 = \|a_1\|^2 + \|a_2\|^2$, and therefore $\|a_1\| \leq \|a_2\| \leq \|a_3\|$, possibly after swapping a_1 and a_2. In the primitive case (i), we can choose a_1, a_2, and $a_3 = a_1 - a_2$ such that $\|a_1\| \leq \|a_2\| \leq \|a_3\|$. In this case, $\mathrm{Vor}(0)$ is a centrally symmetric hexagon with distances $\|a_1\|, \|a_2\|, \|a_3\|$ between antipodal edge pairs.

4.3.2 Equilibrium configurations

Given a lattice in $\mathbb{R}^2$, we are interested in the radius of the disks for which the probability that a random point lies inside exactly one disk is maximized. Further maximizing this probability over all lattices, we get the main result of Section 4.3.

Partial disks. Fix a lattice Λ in $\mathbb{R}^2$. For a radius $\varrho > 0$, consider the set of points that belong to the disk centered at the origin but not to any other disk centered at a point of Λ:

$$D_*(\varrho) = B(0, \varrho) \setminus \bigcup_{0 \neq p \in \Lambda} B(p, \varrho). \tag{4.15}$$

As illustrated in Figure 4.5, for radii strictly between the packing radius and the covering radius, this set is partially closed and partially open. We distinguish between the *convex boundary* that belongs to the circle bounding $B(0, \varrho)$, and the *concave boundary* that belongs to other circles:

$$\partial_x D_*(\varrho) = \partial B(0, \varrho) \cap D_*(\varrho), \tag{4.16}$$

$$\partial_v D_*(\varrho) = \partial D_*(\varrho) \setminus \partial_x D_*(\varrho). \tag{4.17}$$

We note that $\partial_x D_*(\varrho) = \partial B(0, \varrho) \cap \mathrm{Vor}(0)$. By the Inscribed Voronoi Domain Lemma, the vertices of $\mathrm{Vor}(0)$ are all at the same distance from 0. This implies that for $r_\Lambda < \varrho < R_\Lambda$, the convex boundary consists of 2, 4, or 6 circular arcs that alternate with the same number of circular arcs in the concave boundary.

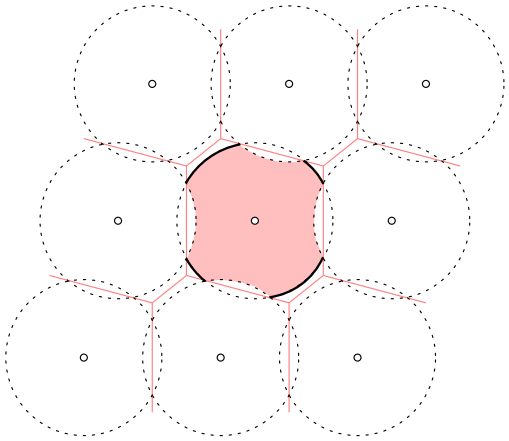

Figure 4.5: The shaded partial disk $D_*(\varrho)$ with its boundary divided into a solid convex portion and a dotted concave portion.

Angles. Recall that the concave boundary consists of at most three pairs of arcs, and let $\alpha_i(\varrho)$ be the angle of each of the two arcs in the i-th pair, for $i = 1, 2, 3$. The total angle of the concave boundary is

$$\Phi_\Lambda(\varrho) = \sum_{i=1}^{3} 2\alpha_i(\varrho), \tag{4.18}$$

and the total angle of the convex boundary is $2\pi - \Phi_\Lambda(\varrho)$. We have $\Phi_\Lambda(r_\Lambda) = 0$ and $\Phi_\Lambda(R_\Lambda) = 2\pi$, and between these two limits, the function is continuous and monotonically increasing.

Lemma 10 (Monotonicity)**.** *Let Λ be a lattice in $\mathbb{R}^2$. Then $\Phi_\Lambda \colon [r_\Lambda, R_\Lambda] \to [0, 2\pi]$ is continuous, with $\Phi_\Lambda(\varrho_1) < \Phi_\Lambda(\varrho_2)$ whenever $\varrho_1 < \varrho_2$.*

Proof. The continuity of the function follows from the fact that $\partial B(0, \varrho)$ intersects $\partial \mathrm{Vor}(0)$ in at most a finite number of points.

To prove monotonicity, we recall that $2\pi - \Phi_\Lambda(\varrho)$ is the total angle of $\partial_x D_*(\varrho) = \partial B(0, \varrho) \cap \mathrm{Vor}(0)$. The Voronoi domain is a convex polygon with $0 \in \mathrm{Vor}(0)$. Drawing circles with radii $\varrho_1 < \varrho_2$ centered at 0, we let $0 \le \theta < 2\pi$ and write $p_1(\theta)$ and $p_2(\theta)$ for the points on the circles in direction θ. Either both points belong to $\mathrm{Vor}(0)$, both points do not belong to $\mathrm{Vor}(0)$, or $p_1(\theta) \in \mathrm{Vor}(0)$ but $p_2(\theta) \notin \mathrm{Vor}(0)$. The fourth combination is not possible, which implies $2\pi - \Phi_\Lambda(\varrho_1) \ge 2\pi - \Phi_\Lambda(\varrho_2)$ or, equivalently, $\Phi_\Lambda(\varrho_1) \le \Phi_\Lambda(\varrho_2)$. To prove the strict inequality, we just need to observe that there is an arc of non-zero length in $\partial_x D_*(\varrho_1)$ such that the corresponding arc in $\partial B(0, \varrho_2)$ lies outside $\mathrm{Vor}(0)$ and therefore does not belong to $\partial_x D_*(\varrho_2)$. □

Area. The probability that a random point belongs to exactly one disk is the area of $D_*(\varrho)$ over the area of $\mathrm{Vor}(0)$. The latter is a constant independent of the radius. We will prove shortly that the former is a unimodal function in ϱ with a single maximum at the radius $\varrho = \varrho_\Lambda$ that balances the lengths of the two kinds of boundaries; see Figure 4.6. We call ϱ_Λ the *equilibrium radius* of Λ. Write $\mathrm{area}_\Lambda \colon [r_\Lambda, R_\Lambda] \to \mathbb{R}$ for the function that maps ϱ to the area of $D * (\varrho)$.

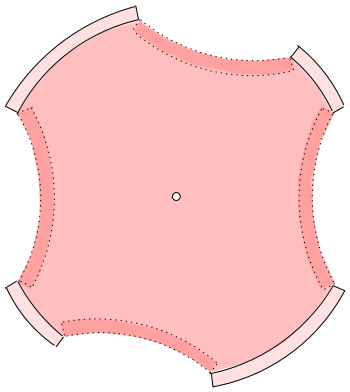

Figure 4.6: Increasing the radius grows $D_*(\varrho)$ along the convex boundary and shrinks it along the concave boundary.

Lemma 11 (Equilibrium Radius)**.** *Let Λ be a lattice in $\mathbb{R}^2$. The function $\mathrm{area}_\Lambda \colon [r_\Lambda, R_\Lambda] \to \mathbb{R}$ is strictly concave, with a unique maximum at the equilibrium radius ϱ_Λ that satisfies $\Phi_\Lambda(\varrho_\Lambda) = \pi$.*

Proof. Recall that $\Phi_\Lambda(\varrho)$ is the total angle of the concave boundary of $D_*(\varrho)$, and $2\pi - \Phi_\Lambda(\varrho)$ is the total angle of the convex boundary. When we increase the radius, the partial disk grows along the convex boundary and shrinks along the concave boundary. Indeed, the derivative is the difference between the two lengths:

$$\frac{\partial \mathrm{area}_\Lambda}{\partial \varrho}(\varrho) = \varrho[2\pi - \Phi_\Lambda(\varrho) - \Phi_\Lambda(\varrho] \tag{4.19}$$

$$= 2\varrho[\pi - \Phi_\Lambda(\varrho)]. \tag{4.20}$$

The derivative vanishes when $\Phi_\Lambda(\varrho) = \pi$, is positive when $\Phi_\Lambda(\varrho) < \pi$ and negative when $\Phi_\Lambda(\varrho) > \pi$, as claimed. □

4.3.3 Optimality of the regular hexagonal grid

Here we present the proof of the main result stated in Section 4.3. After writing the probability that a random point lies in exactly one disk as a function of the radius, we distinguish between three cases, showing that the maximum is attained at the regular hexagonal grid.

Probability. Given a lattice Λ in $\mathbb{R}^2$, we write $r_\Lambda < \varrho_\Lambda < R_\Lambda$ for the packing, equilibrium, and covering radii. Recall that the probability in question is

$$P_\Lambda(\varrho_\Lambda) = \tfrac{\text{area}_\Lambda(\varrho_\Lambda)}{\|a_1\|\|a_2\|\sin\gamma}, \tag{4.21}$$

in which $\Lambda = \Lambda(a_1, a_2)$ and γ is the angle between a_1 and a_2. Recall furthermore that the convex boundary consists of at most six arcs, two each with angle α_1, α_2, α_3, in which we set the angle to zero if the arc degenerates to a point or is empty.

Lemma 12 (Equilibrium Area)**.** *Let $\Lambda = \Lambda(a_1, a_2)$ be a lattice in $\mathbb{R}^2$ with angle γ between a_1 and a_2. Then*

$$P_\Lambda(\varrho_\Lambda) = \tfrac{2\varrho_\Lambda^2}{\|a_1\|\|a_2\|\sin\gamma} \cdot \sum_{i=1}^{3} \sin\alpha_i. \tag{4.22}$$

Proof. Recall that $\|a_1\|\|a_2\|\sin\gamma$ is the area of $\mathrm{Vor}(0)$. Let A_{in} be the area of $B(0,\varrho_\Lambda) \cap \mathrm{Vor}(0)$, let A_{out} be the area of $B(0,\varrho_\Lambda) \setminus \mathrm{Vor}(0)$, and note that $A_{\text{in}} - A_{\text{out}}$ is the area of $D_*(\varrho_\Lambda)$. Since $A_{\text{in}} + A_{\text{out}} = \varrho_\Lambda^2\pi$, we have $A_{\text{in}} - A_{\text{out}} = \varrho_\Lambda^2\pi - 2A_{\text{out}}$. The portion of $B(0,\varrho_\Lambda)$ outside the Voronoi domain consists of up to three symmetric pairs of disk segments, with total area

$$A_{\text{out}} = 2\sum_{i=1}^{3} \tfrac{\varrho_\Lambda^2}{2}(\alpha_i - \sin\alpha_i) \tag{4.23}$$

$$= \varrho_\Lambda^2 \left(\tfrac{\pi}{2} - \sum_{i=1}^{3} \sin\alpha_i \right), \tag{4.24}$$

in which the second line is obtained using $\sum_{i=1}^{3}\alpha_i = \frac{\pi}{2}$ from the Equilibrium Radius Lemma. The probability is $A_{\text{in}} - A_{\text{out}}$ divided by the area of the Voronoi domain:

$$P_\Lambda(\varrho_\Lambda) = \tfrac{\varrho_\Lambda^2\pi - 2A_{\text{out}}}{\|a_1\|\|a_2\|\sin\gamma}. \tag{4.25}$$

Together with (4.24) this implies the claimed relation. □

Case analysis. We focus on the primitive case in which the Voronoi domain is a hexagon, considering the non-primitive case a limit situation in which two of the edges shrink to zero length. Let $a_1, a_2 \in \mathbb{R}^2$ be generators of the lattice satisfying the condition in the Non-obtuse Generators Lemma, set $a_3 = a_1 - a_2$, and assume $\|a_1\| \leq \|a_2\| \leq \|a_3\|$. Recall that these three lengths are the distances between parallel edges of the hexagon. Further notice that we have $r_\Lambda = \frac{\|a_1\|}{2}$ for the packing radius and $R_\Lambda > \frac{\|a_3\|}{2}$ for the covering radius. As before, we write α_i for the angles of the arcs of $\partial_x D_*(\varrho)$, and we index such that $\alpha_1 \geq \alpha_2 \geq \alpha_3$.

CASE 1: $\frac{\|a_1\|}{2} < \varrho_\Lambda \leq \frac{\|a_2\|}{2}$. Then $\alpha_1 > 0$ and $\alpha_2 = \alpha_3 = 0$.

CASE 2: $\frac{\|a_2\|}{2} < \varrho_\Lambda \leq \frac{\|a_3\|}{2}$. Then $\alpha_1 \geq \alpha_2 > 0$ and $\alpha_3 = 0$.

CASE 3: $\frac{\|a_3\|}{2} < \varrho_\Lambda < R_\Lambda$. Then $\alpha_1 \geq \alpha_2 \geq \alpha_3 > 0$.

For example the configuration depicted in Figure 4.5 falls into Case 2. Using the expression for the probability in the Equilibrium Area Lemma, we determine the maximum for each of the three cases. Here we state the results, referring to Appendix C for the proofs. By *the probability* we mean of course the probability that a random point belongs to exactly one disk.

Lemma 13 (Two Arcs)**.** *In Case 1, the maximum probability is attained for* $\|a_2\| = \sqrt{2}\|a_1\|$, $\gamma = \arccos \frac{1}{2\sqrt{2}}$, *and* $\varrho_\Lambda = \|a_1\|/\sqrt{2}$, *which gives* $P_\Lambda(\varrho_\Lambda) = 0.755\ldots$.

Lemma 14 (Four Arcs)**.** *In Case 2, the maximum probability is attained for* $\|a_2\| = \|a_1\|$, $\gamma = \arccos(\sqrt{2} - 1)$, *and* $\varrho_\Lambda = \|a_1\|\sqrt{1 - 1/\sqrt{2}}$, *which gives* $P_\Lambda(\varrho_\Lambda) = 0.910\ldots$.

Lemma 15 (Six Arcs)**.** *In Case 3, the maximum probability is attained for* $\|a_2\| = \|a_1\|$ = $\|a_3\|$, $\gamma = \frac{\pi}{3}$ *and* $\varrho_\Lambda = \|a_1\|/(2\cos\frac{\pi}{12})$, *which gives* $P_\Lambda(\varrho_\Lambda) = 0.928\ldots$.

Note that the lattice in the Six Arcs Lemma is the regular hexagonal grid. Comparing the three maximum probabilities, we see that the regular hexagonal grid gives the global optimum; see Figures 4.7. For this lattice, we get ϱ_H such that each disk overlaps with six others and in each case covers 30° of the bounding circle: the 12-hour clock configuration in the plane. This implies the Main Theorem stated in Section 4.3.

We further illustrate the result by showing the graph of the function that maps $\|a_1\|/\|a_2\|$ and the angle γ to the probability at the equilibrium radius; see Figure 4.8.

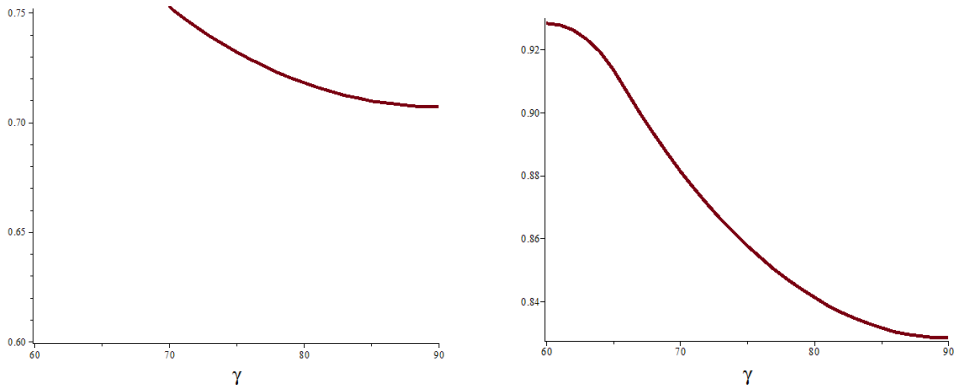

Figure 4.7: *Left:* for $\sqrt{2}\|a_1\| = \|a_2\| \leq \|a_3\|$, the angle γ is between $\arccos \frac{1}{2\sqrt{2}}$ and $\frac{\pi}{2}$. *Right:* for $\|a_1\| = \|a_2\| \leq \|a_3\|$, the angle γ is between $\frac{\pi}{3}$ and $\frac{\pi}{2}$. In both cases, the probability increases as the angle decreases, attaining its maximum at the minimum angle.

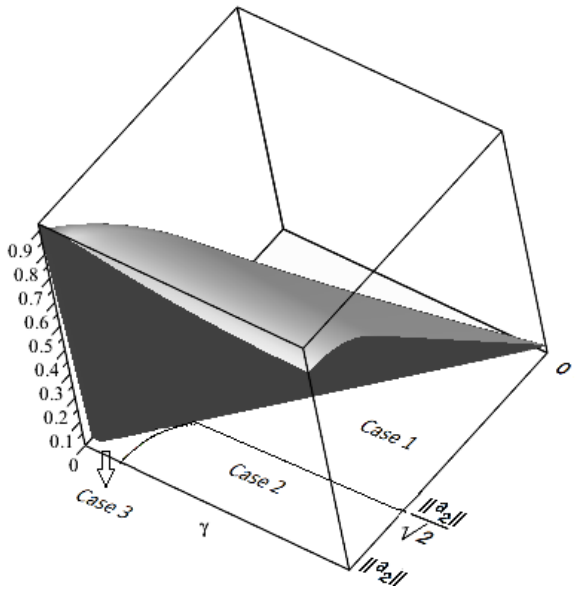

Figure 4.8: The graph of the function that maps $0 \leq \|a_1\|/\|a_2\| \leq 1$ and $\arccos \frac{\|a_1\|}{2\|a_2\|} \leq \gamma \leq 90°$ to the probability that a random point lies in exactly one disk. The thus defined domain resembles a triangle and decomposes into three regions corresponding to Cases 1, 2, 3. The regular hexagonal grid is located at the lower left corner of the domain.

4.4 Soft sphere packing

In this section we extend the previous relaxed packing setting to 3D. Placing the sphere centers on a lattice, we define the soft density of the configuration by penalizing multiple

overlaps. Considering the 1-parameter family of diagonally distorted 3-dimensional integer lattices, we show that the soft density is maximized at the FCC lattice.

4.4.1 Lattice configurations

In $\mathbb{R}^n$, we need n linearly independent vectors to define a *lattice*, which consists of all integer combinations:

$$\Lambda(a_1, a_2, \ldots, a_n) = \left\{ p = \sum_{i=1}^{n} k_i a_i \mid k_i \in \mathbb{Z} \right\}. \tag{4.26}$$

Same as already pointed out for $\mathbb{R}^2$, note that 0 is a point in $\Lambda = \Lambda(a_1, a_2, \ldots, a_n)$, and that the neighborhood of every lattice point looks like the neighborhood of every other lattice point. We will therefore focus on 0 and its neighborhood.

Voronoi Domains and Brillouin Zones

A standard tool in the study of lattices is the *Voronoi diagram*, which assigns to each point $p \in \Lambda$ the set of points $x \in \mathbb{R}^n$ for which p is the closest lattice point or, if there is a tie, p is among the closest lattice points. This set is a convex polyhedron and commonly referred to as the *Voronoi domain* of p. We are interested in short- as well as long-range interactions between the points, which motivates us to generalize this concept.

Perpendicular bisectors. Following Fejes Toth [Tóth, 1976; Tóth, 1979], we define the *i-th Voronoi domain* of 0 as the set of points $x \in \mathbb{R}^n$ for which 0 is among the i nearest lattice points, denoting this domain by $\mathrm{Vor}^i(0)$. We write $\mathrm{Vor}(0) = \mathrm{Vor}^1(0)$ for the ordinary Voronoi domain.

There are at least two rather different ways to construct these domains; see Figure 4.9 for an illustration of the first. Recall that the *perpendicular bisector* of $p \neq q$ is the hyperplane of points at equal distance from both: $\|x - p\| = \|x - q\|$. Drawing all perpendicular bisectors defined by 0 and $p \in \Lambda \setminus \{0\}$, we get an arrangement of countably many hyperplanes in $\mathbb{R}^n$. The hyperplanes decompose $\mathbb{R}^n$ into *chambers*, which are maximal closed sets so that no two points lie on opposite sides of any of the

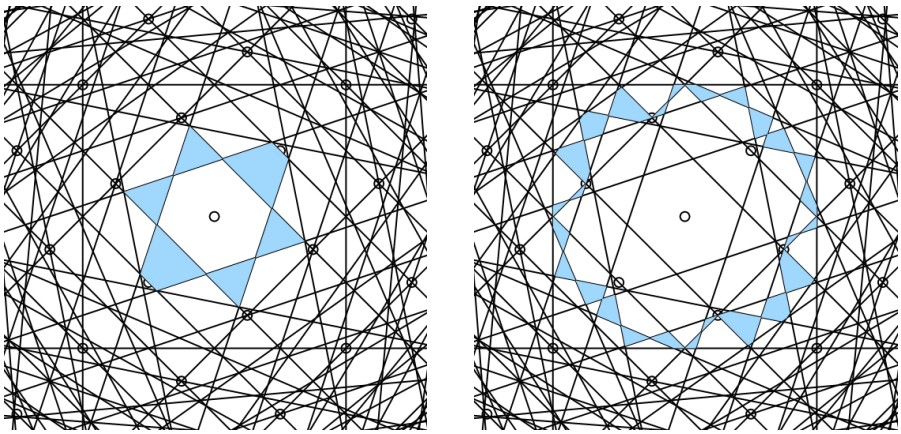

Figure 4.9: Drawing all bisectors defined by 0 and other points in the lattice, we get the i-th Brillouin zone of 0 as the closure of the points separated from 0 by $i-1$ of the bisectors. We highlight the 2-nd Brillouin zone on the *left* and the 6-th Brillouin zone on the *right*. Related to this concept is the i-th Voronoi domain of 0, which is the union of the first i Brillouin zones or, equivalently, the closure of the points separated from 0 by $i-1$ or fewer lines.

hyperplanes. For example $\mathrm{Vor}(0)$ is the unique chamber that contains 0. Every other chamber is separated from 0 by at least one hyperplane, and $\mathrm{Vor}^i(0)$ is the union of all chambers separated from 0 by at most $i-1$ hyperplanes.

The generalized Voronoi domains are not necessarily convex, but they satisfy a related weaker condition. A set $A \subseteq \mathbb{R}^n$ is *star-convex* if there exists a point $a \in A$ such that for every $x \in A$ the entire line segment connecting a to x is contained in A. The *kernel* of A is the set of such points a, which is a subset of A.

Lemma 16 (Star-convexity)**.** *Let Λ be a lattice in $\mathbb{R}^n$. For each $i \geq 1$, $\mathrm{Vor}^i(0)$ is bounded and star-convex, and 0 lies in the interior of its kernel.*

PROOF. Because Λ is a lattice, there is a real number $R = R(i)$ such that every ball of radius R contains i or more lattice points in its interior. It follows that no point $x \in \mathrm{Vor}^i(0)$ can be at distance R or further from 0. In other words, $\mathrm{Vor}^i(0)$ is bounded. It is star-convex because $x \in \mathrm{Vor}^i(0)$ implies that all points on the line segment connecting x to 0 belong to $\mathrm{Vor}^i(0)$. Indeed, if x is separated by at most $i-1$ bisectors from 0 then so is any point on this line segment. This also proves that 0 belongs to the kernel of $\mathrm{Vor}^i(0)$. But this is still true if we substitute any point of the first Voronoi domain for 0, so the

entire $\mathrm{Vor}(0)$ belongs to the kernel, which implies that 0 belongs to the interior of the kernel, as claimed. ◰

It is often convenient to consider the difference between two contiguous domains rather than individual domains. Following the French physicist Léin Brillouin [Brillouin, 1930], we therefore define $Z_i(0)$ as the closure of $\mathrm{Vor}^i(0) \setminus \mathrm{Vor}^{i-1}(0)$, calling it the *$i$-th Brillouin zone* centered at 0. Setting $\mathrm{Vor}^0(0) = \emptyset$, the first zone is $Z_1(0) = \mathrm{Vor}(0)$.

Zone invariants. Fixing i, we note that the i-th Brillouin zones of different lattice points have disjoint interiors, and the collection of all i-th zones covers $\mathbb{R}^n$. Incidentally, this is the *degree-i Voronoi diagram* as defined in [Edelsbrunner and Seidel, 1986]. Since any two i-th zones are translates of each other, and because there are equally many i-th zones as there are j-th zones — namely one for each lattice point — it must be that all Brillouin zones have the same volume. This result was mentioned already by Bieberbach [Bieberbach., 1939]. We formalize this insight and generalize it to measures beyond the n-dimensional volume. Recall that a function $\mu\colon \mathbb{R}^n \to \mathbb{R}$ is *integrable* if

$$\mu[\mathcal{S}] = \int_{x\in\mathcal{S}} \mu(x)\,\mathrm{d}x \tag{4.27}$$

is well defined for every Borel set $\mathcal{S} \subseteq \mathbb{R}^n$. It is *$\Lambda$-periodic* if $\mu(x) = \mu(x+p)$ for every $x \in \mathbb{R}^n$ and every $p \in \Lambda$. For example, if μ is identical 1, then it is obviously periodic and $\mu[\mathcal{S}]$ is the n-dimensional volume of $\mathcal{S}$. We prove that every Brillouin zone has the same measure, no matter what center or index.

Theorem 9 (Zone Invariants)**.** *Let Λ be a lattice in $\mathbb{R}^n$ and $\mu\colon \mathbb{R}^n \to \mathbb{R}$ be a Λ-periodic integrable function. Then $\mu[Z_i(p)] = \mu[Z_j(q)]$ for all $i, j \geq 1$ and all $p, q \in \Lambda$.*

PROOF. In a lattice, every point looks like every other point: $\Lambda = \Lambda + p$ for every $p \in \Lambda$. For a point $p \in \Lambda$, we have $Z_i(p) = Z_i(0) + p$, and because μ is Λ-periodic, $\mu[Z_i(p)] = \mu[Z_i(0)]$ for every $i \geq 1$. By transitivity,

$$\mu[Z_i(p)] = \mu[Z_i(q)], \tag{4.28}$$

for all $p, q \in \Lambda$ and all $i \geq 1$. To extend this relation to Brillouin zones with different indices, we consider the closed ball with radius $R > 0$ centered at the origin, denoted

by $B(0,R)$. Counting the lattice points in the ball with $m(R) = \operatorname{card}(B(0,R) \cap \Lambda)$, we write $\Omega_i(R)$ for the union of the i-th zones centered at these $m(R)$ points. Letting w_i be the maximum distance of a point $x \in Z_i(0)$ from 0, we note that the symmetric difference between $B(0,R)$ and $\Omega_i(R)$ is contained inside the annulus of points at distance at most w_i on either side of the sphere that bounds $B(0,R)$. With increasing R, the volume of this annulus grows asymptotically slower than the volume of the ball. Hence,

$$\mu[Z_i(0)] = \frac{\mu[\Omega_i(R)]}{m(R)} = \lim_{R\to\infty} \frac{\mu[B(0,R)]}{m(R)}. \tag{4.29}$$

The right-hand side converges to a finite value that is independent of i. It follows that the measure of any i-th zone is the same as the measure of any j-th zone. The claimed relation thus follows from (4.28) and (4.29). ◻

EXAMPLE 1. Fixing a non-negative integer j, set $\mu(x) = 1$ if x is covered by j or more balls, and set $\mu(x) = 0$ otherwise. Clearly, μ is a periodic integrable function, so Theorem 9 implies that the volume of points covered by at least j balls is the same within every Brillouin zone. For $j = 0$, this formalizes our informal argument that all zones have the same n-dimensional volume.

EXAMPLE 2. Let μ have Dirac deltas at the lattice points. More concretely, let $\epsilon > 0$ be sufficiently small and set

$$\mu(x) = \max_{p\in\Lambda} \left\{ 0, \tfrac{(n+1)(\epsilon - \|x-p\|)}{\nu_n \epsilon^{n+1}} \right\}, \tag{4.30}$$

in which ν_n is the n-dimensional volume of the unit ball. Clearly, μ is a periodic integrable function and $\mu[\mathrm{Vor}(0)] = 1$. Theorem 9 implies that the measure of every zone is 1. Interpreting this measure as counting lattice points, we get exactly one lattice point per zone, provided we take appropriate fractions if the points are shared.

Iterative Construction

The second way of constructing the generalized Voronoi domains proceeds in rounds of invasions and relocations of conquered real-estate. We remark that Sibson used the same “area-stealing” idea to construct interpolations based on Voronoi diagrams [Sibson, 1980].

Invasion and relocation. We construct the 2-nd Brillouin zone centered at 0 by letting the Voronoi neighbors invade $\mathrm{Vor}(0)$ and divide up the real-estate. Each obtained region belongs to an ordered pair, $(0, p)$, in which 0 and p are the 1-st and 2-nd lattice points from any point in the region. Translating the region to the Voronoi domain of $-p$, we get $Z_2(0)$ as the union of these regions; see Figure 4.10.

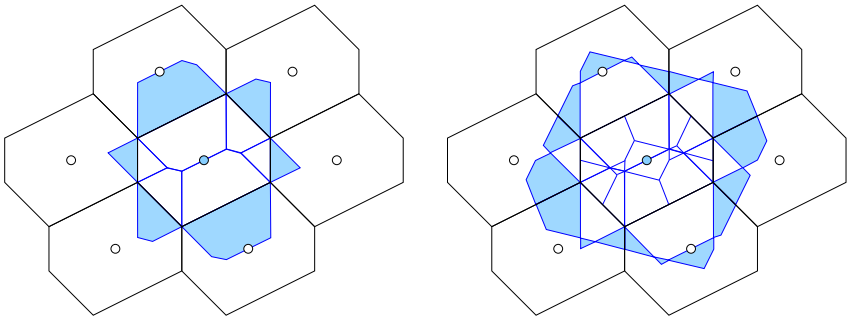

Figure 4.10: *Left:* We decompose the first Voronoi domain of 0 according to the second nearest lattice point, and assemble the 2-nd Brillouin zone by moving each piece to the reflection of the corresponding point. *Right:* We refine the decomposition according to the third nearest lattice point, and assemble the 3-rd Brillouin zone by moving each piece to the reflection of the corresponding point.

We can iterate. Specifically, we further decompose each region by letting the surrounding regions invade and divide up the real-estate, as before. Each region in this decomposition belongs to an ordered triplet, $(0, p, q)$, in which $0, p, q$ are the 1-st, 2-nd, 3-rd lattice points from any point in the region. Translating the region to the Voronoi domain of $-q$, we get $Z_3(0)$ as the union of these regions, as before; see again Figure 4.10.

Piecewise translations. We formalize the iterative construction by proving that there is a piecewise translation from $\mathrm{Vor}(0)$ to $Z_i(0)$ for every i. To describe this map, let x be a point in $\mathrm{Vor}(0)$. Ordering the lattice points in increasing distance from x, we get $\|x - p_1\| \leq \|x - p_2\| \leq \ldots \leq \|x - p_i\| \leq \ldots$. Most of these inequalities are strict, and ties are broken arbitrarily. For $i \geq 1$, we define $f_i \colon \mathrm{Vor}(0) \to Z_i(0)$ by mapping x to $f_i(x) = x - p_i$. We will show that f_i is *almost* a bijection. To express this, we let $V_i^\circ \subseteq \mathrm{Vor}(0)$ be the set of points x in $\mathrm{Vor}(0)$ for which the 1-st and i-th lattice points are unique: $\|x - p_1\| < \|x - p_2\|$ and $\|x - p_{i-1}\| < \|x - p_i\| < \|x - p_{i+1}\|$. Similarly, we

let $Z_i^\circ \subseteq Z_i(0)$ be the set of points in the i-th Brillouin zone for which the 1-st and i-th lattice points are unique. Note that V_i° is contained in the interior of $\mathrm{Vor}(0)$ and contains almost all points of the Voronoi domain. Similarly, Z_i° is contained in the interior of $Z_i(0)$ and contains almost all points of the i-th Brillouin zone.

Lemma 17 (Bijection)**.** *For each $i \geq 1$, the restriction of the function f_i to $V_i^\circ \subseteq \mathrm{Vor}(0)$ and $Z_i^\circ \subseteq Z_i(0)$ is a bijection.*

PROOF. First we show that the restriction of f_i is well defined. Recall that 0 and p_i are the unique 1-st and i-th lattice points from x. Since $f_i(x) = x - p_i$, this implies that $0 - p_i = -p_i$ and $p_i - p_i = 0$ are the unique 1-st and i-th lattice points from $f_i(x)$. It follows that $f_i(x)$ belongs to the interior of $\mathrm{Vor}(-p_i)$ as well as to the interior of $Z_i(0)$, and thus to Z_i°.

To prove that the restriction is injective, let $p_i, p_i' \in \Lambda$ be the i-th lattice points from $x, x' \in V_i^\circ$. If $p_i = p_i'$, then $f_i(x) - f_i(x') = x - x'$, so that $x \neq x'$ implies $f_i(x) \neq f_i(x')$. Otherwise, if $p_i \neq p_i'$, we have $f_i(x) \neq f_i(x')$ because the two points lie in the interiors of two different 1-st Voronoi domains.

To prove that f_i is surjective, we start with a point y in Z_i°, and let $p \in \Lambda$ such that $y \in \mathrm{Vor}(-p)$. Define $x = y + p$. Since $-p$ and 0 are the unique 1-st and i-th lattice points from y, this implies that $-p + p = 0$ and $0 + p = p$ are the unique 1-st and i-th lattice points from x. Hence, x belongs to V_i° and $f_i(x) = y$. ◻

It is not difficult to see that the functions f_i can be used to give a second proof of Theorem 9. Indeed, the restriction of f_i to V_i° and Z_i° is a bijection that consists of finitely many translations. Each translation maps a connected piece of V_i° to a connected piece of Z_i°. By the periodicity of μ, the measure of these two pieces is the same. Since the pieces are pairwise disjoint and cover almost all of $\mathrm{Vor}(0)$ and of $Z_i(0)$, this implies that $\mu[\mathrm{Vor}(0)] = \mu[Z_i(0)]$. We get the relation in Theorem 9 by transitivity.

Configurations of balls

We call a set of closed balls in $\mathbb{R}^n$ a *configuration of balls* or, equivalently, a *configuration of spheres* if we want to emphasize how the boundaries of the balls decompose space. We are interested in the case in which all balls have the same radius and the

centers are placed periodically in $\mathbb{R}^n$. Letting $B(p,r) = B(0,r) + p$ be the closed ball with radius $r > 0$ centered at $p \in \mathbb{R}^n$, we write

$$\mathcal{B}(\Lambda, r) = \{B(p,r) \mid p \in \Lambda\} \tag{4.31}$$

for the configuration of balls defined by the lattice and the radius. In this subsection, we fix Λ as well as r and write $\mathcal{B} = \mathcal{B}(\Lambda, r)$.

Multiple covering. For each $i \geq 0$, let $\mathbb{B}_i \subseteq \mathbb{R}^n$ be the set of points that are covered by at least i of the balls in $\mathcal{B}$. For finite r, there is a minimum index, m, such that $\mathbb{B}_i = \emptyset$ iff $i \geq m$. Clearly, $\emptyset = \mathbb{B}_m \subseteq \ldots \subseteq \mathbb{B}_1 \subseteq \mathbb{B}_0 = \mathbb{R}^n$. To assess the relative size of these sets, we let φ_i be the probability that a randomly selected point in $\mathbb{R}^n$ is contained in at least i of the balls. More formally,

$$\varphi_i(\Lambda, r) = \lim_{R \to \infty} \frac{\mathrm{vol}[\mathbb{B}_i \cap B(0,R)]}{\mathrm{vol}[B(0,R)]} = \frac{\mathrm{vol}[\mathbb{B}_i \cap \mathrm{Vor}(0)]}{\mathrm{vol}[\mathrm{Vor}(0)]}, \tag{4.32}$$

in which we get the right-hand side because $\mathbb{B}_i$ intersects every Voronoi domain in the same way. The inclusions among the $\mathbb{B}_i$ imply $0 = \varphi_m \leq \ldots \leq \varphi_1 \leq \varphi_0 = 1$. Observe also that $\varphi_i - \varphi_{i+1}$ is the probability that a randomly selected point lies in exactly i balls of $\mathcal{B}$.

Probability in terms of volume. We generalize (4.32) by considering the intersections of $B(0,r)$ with the generalized Voronoi domains: $D_i(r) = B(0,r) \cap \mathrm{Vor}^i(0)$, for $i \geq 0$, noting that $D_0(r) = \mathrm{Vor}^0(0) = \emptyset$. Continuing the convention of dropping the fixed radius from the notation, we write $D_i = D_i(r)$.

Lemma 18 (Probability)**.** *For each $i \geq 1$, the probability that a randomly selected point in $\mathbb{R}^n$ belongs to at least i balls in $\mathcal{B}$ is*

$$\varphi_i = \frac{\mathrm{vol}[D_i] - \mathrm{vol}[D_{i-1}]}{\mathrm{vol}[\mathrm{Vor}(0)]}. \tag{4.33}$$

PROOF. Let x be a point in $\mathrm{Vor}(0)$. We prove the claimed relation by showing that the point $y = f_i(x)$ belongs to $D_i \setminus D_{i-1}$ iff x is covered by at least i balls; see Figure 4.11. This implies (4.33). We now prove the two directions of the claimed equivalence.

"$\Longrightarrow$". By construction of the function, $y = f_i(x)$ belongs to $Z_i(0)$. If it furthermore belongs to $B(0,r)$ and thus to $D_i \setminus D_{i-1}$, then 0 is the i-th lattice point from y and its

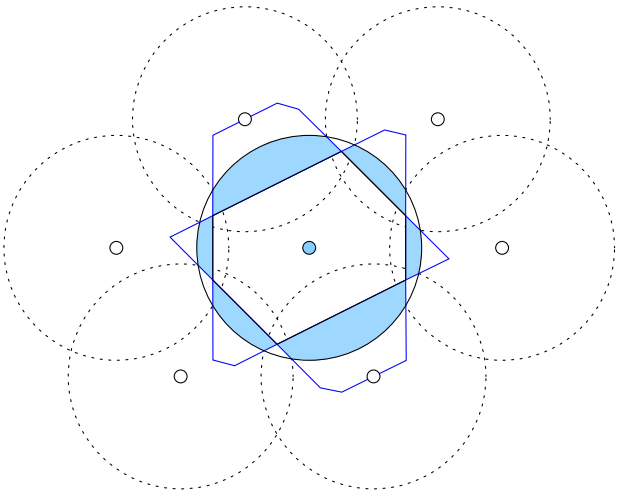

Figure 4.11: The probability that a randomly selected point is covered by at least two disks is the normalized area of the intersection between the disk centered at 0 and the 2-nd Brillouin zone of 0. Indeed, we can move the pieces of this intersection back into the first Voronoi domain so that they decompose the portion covered by at least two disks, the one centered at 0 and the other centered at a neighboring lattice point.

ball covers y. Hence, y is covered by at least i balls, which implies that x is covered by at least i balls.

"$\Longleftarrow$". If x is covered by at least i balls, then so is $y = f_i(x)$. We have $y \in Z_i(0)$ by definition, and $y \in B(0, r)$ because 0 is the i-th lattice point from y. Hence $y \in D_i \setminus D_{i-1}$. □

4.4.2 Measures of density

Given a lattice configuration of balls, the classic notion of *density* is the expected number of balls that contain a randomly selected point:

$$\delta(\Lambda, r) = \sum_{i \geq 1} \varphi_i = \frac{\mathrm{vol}[B(0, r)]}{\mathrm{vol}[\mathrm{Vor}(0)]}, \tag{4.34}$$

in which the ratio on the right-hand side is clear and also follows from Lemma 18. We introduce variants of this classic notion that penalize for overlapping balls and prove that for a fixed lattice they are unimodal functions of the radius.

Soft densities

In this subsection, we introduce a family of soft densities and relate them to volumes of balls and generalized Voronoi domains.

Two definitions. Let $\Lambda \subseteq \mathbb{R}^n$ be a lattice and $r > 0$ be a radius. For each $j \geq 1$, we define the *j-th soft density* of $\mathcal{B} = \mathcal{B}(\Lambda, r)$ as

$$\delta_j(\Lambda, r) = \sum_{i=1}^{j} \varphi_i - \sum_{i=j+1}^{\infty} \varphi_i. \tag{4.35}$$

We have $\delta_1 \leq \delta_2 \leq \ldots \leq \delta$, and $\delta_j = \delta$ iff the configuration does not have any $j+1$ overlapping balls.

From the point of view of the applications motivating the work described in this section, the most interesting soft density is the first: $\delta_1(\Lambda, r) = \varphi_1 - \varphi_2 - \varphi_3 - \ldots$. It favors configurations of balls with only minor overlap. Nonetheless, there are lattices for which the configuration that maximizes the 1-st soft density has triplets of overlapping balls. To avoid the complications caused by triple intersections, we introduce the *1-st simplified soft density*:

$$\delta_{1\mathrm{s}}(\Lambda, r) = \sum_{i=1}^{\infty} (3 - 2i)\varphi_i, \tag{4.36}$$

noting that $\delta_{1\mathrm{s}} \leq \delta_1$ agree on the first two terms and differ only in the weight given to overlaps of three or more balls. We will see shortly that $\delta_{1\mathrm{s}}$ is easier to compute than δ_1.

Density in terms of volume. Recall that (4.34) writes the classic notion of density as the normalized volume of a ball. We generalize this relation to soft densities, unsimplified and simplified.

Lemma 19 (Soft Density)**.** *Let $j \geq 1$. The j-th soft density and the 1-st simplified soft density of the configuration of balls defined by a lattice Λ and a radius r are*

$$\delta_j = \frac{2\mathrm{vol}[D_j] - \mathrm{vol}[B(0,r)]}{\mathrm{vol}[\mathrm{Vor}(0)]}, \tag{4.37}$$

$$\delta_{1\mathrm{s}} = \frac{\mathrm{vol}[B(0,r)]}{\mathrm{vol}[\mathrm{Vor}(0)]} - \sum_{0 \neq p \in \Lambda} \frac{\mathrm{vol}[B(0,r) \cap B(p,r)]}{\mathrm{vol}[\mathrm{Vor}(0)]}. \tag{4.38}$$

PROOF. We first prove the relation for the unsimplified soft densities. Writing the two normalized volumes on the right-hand side of (4.37) in terms of probabilities, we get

$$\frac{\mathrm{vol}[D_j]}{\mathrm{vol}[\mathrm{Vor}(0)]} = \sum_{i=1}^{j} \varphi_i, \tag{4.39}$$

$$\frac{\mathrm{vol}[B(0,r)]}{\mathrm{vol}[\mathrm{Vor}(0)]} = \sum_{i=1}^{\infty} \varphi_i. \tag{4.40}$$

Taking the first sum twice and subtracting the second sum, we match the definition of the j-th soft measure in (4.35).

Second, we prove the relation for the simplified soft density. Equation (4.40) writes the first normalized volume in (4.38) in terms of probabilities. To do the same for the second normalized volume, we note that the common intersection of $B(0,r)$ and $k-1$ other balls is accounted for $k-1$ times. Recall that $B(0,r) \cap \mathbb{B}_k$ is the subset of the ball covered by at least $k-1$ other balls. The second normalized volume in (4.38) can therefore be rewritten as

$$\mathrm{V}_{\mathrm{Lunes}} = \sum_{k=2}^{\infty} \frac{\mathrm{vol}[B(0,r) \cap \mathbb{B}_k]}{\mathrm{vol}[\mathrm{Vor}(0)]} = \sum_{k=2}^{\infty} \sum_{i=1}^{\infty} \frac{\mathrm{vol}[Z_i(0) \cap B(0,r) \cap \mathbb{B}_k]}{\mathrm{vol}[\mathrm{Vor}(0)]}, \tag{4.41}$$

in which we get the second line by decomposing the ball into its intersections with the Brillouin zones. To write the double-sum in terms of probabilities, we note that the indicator function of $\mathbb{B}_k$ is Λ-periodic. Hence, Theorem 9 implies that

$$\frac{\mathrm{vol}[Z_i(0) \cap \mathbb{B}_k]}{\mathrm{vol}[\mathrm{Vor}(0)]} = \varphi_k \tag{4.42}$$

for all choices of $i \geq 1$ and $k \geq 0$. Recall now that for every point $x \in Z_i(0)$, the origin is the i-th lattice point from x. For $1 \leq i \leq k$, 0 is among the first k lattice points. Hence, if x is contained in k or more balls, then it is also contained in $B(0,r)$. For $k \leq i$, $x \in Z_i(0)$ is contained in $B(0,r)$ iff it is contained in i or more balls. Hence,

$$\frac{\mathrm{vol}[Z_i(0) \cap B(0,r) \cap \mathbb{B}_k]}{\mathrm{vol}[\mathrm{Vor}(0)]} = \begin{cases} \varphi_k & \text{for } 1 \leq i \leq k \\ \varphi_i & \text{for } k \leq i, \end{cases} \tag{4.43}$$

in which we get the first line from (4.42) and the second line from (4.33). Starting with (4.38), we use (4.40) to rewrite the first sum and combine (4.41) with (4.43) to rewrite the second sum to get

$$\delta_{1\mathrm{s}} = \sum_{i=1}^{\infty} \varphi_i - \sum_{k=2}^{\infty} \left(k\varphi_k + \sum_{i=k+1}^{\infty} \varphi_i \right) = \sum_{i=1}^{\infty} (3-2i)\varphi_i. \tag{4.44}$$

Simple rearrangements lead to the right-hand side, which matches the definition of the 1-st simplified density in (4.36). ◰

Derivatives

In this subsection, we fix the lattice but vary the radius. It is therefore convenient to write $\mathcal{B}(r) = \mathcal{B}(\Lambda, r)$, $\delta_j(r) = \delta_j(\Lambda, r)$, etc. We are interested in the radius at which a soft density attains its maximum.

Derivative of probability. Since all density measures in this section are linear combinations of probabilities, we focus on the functions $\varphi_i \colon \mathbb{R}_+ \to \mathbb{R}$. Remembering that $\varphi_i(r)$ is the normalized volume of $B(0,r) \cap Z_i(0)$, we introduce radii $r_i < R_i$ such that this intersection is empty iff $r < r_i$ and equal to $Z_i(0)$ iff $R_i \leq r$. Specifically, r_i is the supremum of the radii for which every ball contains fewer than i lattice points, and R_i is the supremum of the radii for which there exists a center such that the ball contains fewer than i lattice points. For example, r_2 is the packing radius of Λ, and R_1 is the covering radius of Λ. Within the interval $[r_i, R_i]$, φ_i increases monotonically from 0 to 1. When we increase the radius, the volume of $B(0,r) \cap Z_i(0)$ grows where the sphere $\partial B(0,r)$ lies inside $Z_i(0)$. To streamline the notation, we write $S_i(r) = \partial B(0,r) \cap \mathrm{Vor}^i(0)$, and $\mathrm{area}[S_i(r)]$ for its $(n-1)$-dimensional volume. Recalling that the i-th Brillouin zone is $Z_i(0) = \mathrm{Vor}^i(0) \setminus \mathrm{Vor}^{i-1}(0)$, we therefore get

$$\frac{\partial \varphi_i}{\partial r}(r) = \frac{\mathrm{area}[S_i(r)] - \mathrm{area}[S_{i-1}(r)]}{\mathrm{vol}[\mathrm{Vor}(0)]} \tag{4.45}$$

for the derivative of the probability that a randomly selected point lies in at least i balls.

Derivative of soft density. Recall the definition of the soft density in (4.35) and that of the simplified soft density in (4.36). Accordingly, their derivatives are

$$\frac{\partial \delta_j}{\partial r}(r) = \sum_{i=1}^{j} \frac{\partial \varphi_i}{\partial r}(r) - \sum_{i=j+1}^{\infty} \frac{\partial \varphi_i}{\partial r}(r), \tag{4.46}$$

$$\frac{\partial \delta_{1\mathrm{s}}}{\partial r}(r) = \sum_{i=1}^{\infty} (3-2i) \frac{\partial \varphi_i}{\partial r}(r), \tag{4.47}$$

for every integer $j \geq 1$ and every $r \in \mathbb{R}_+$. These derivatives can also be written in terms of areas.

Lemma 20 (Soft Density Derivative)**.** *Let $j \geq 1$. The derivatives of the j-th soft density and of the 1-st simplified soft density of the configuration defined by a lattice $\Lambda \in \mathbb{R}^n$ and a radius $r > 0$ are*

$$\frac{\partial \delta_j}{\partial r}(r) = \frac{2\mathrm{area}[S_j(r)] - \mathrm{area}[\partial B(0,r)]}{\mathrm{vol}[\mathrm{Vor}(0)]}, \tag{4.48}$$

$$\frac{\partial \delta_{1\mathrm{s}}}{\partial r}(r) = \frac{\mathrm{area}[\partial B(0,r)]}{\mathrm{vol}[\mathrm{Vor}(0)]} - \sum_{0 \neq p \in \Lambda} \frac{2\mathrm{area}[\partial B(0,r) \cap B(p,r)]}{\mathrm{vol}[\mathrm{Vor}(0)]}. \tag{4.49}$$

PROOF. Using (4.45), we write both sums on the right-hand side of (4.46) as telescoping sums. Almost all terms cancel, and we get

$$\sum_{i=1}^{j} \frac{\partial \varphi_i}{\partial r}(r) = \frac{\mathrm{area}[S_j(r)]}{\mathrm{vol}[\mathrm{Vor}(0)]}, \tag{4.50}$$

$$\sum_{i=j+1}^{\infty} \frac{\partial \varphi_i}{\partial r}(r) = \frac{\mathrm{area}[\partial B(0,r)] - \mathrm{area}[S_j(r)]}{\mathrm{vol}[\mathrm{Vor}(0)]}. \tag{4.51}$$

Subtracting (4.51) from (4.50), we get (4.48). Alternatively, we would start with (4.37) and get (4.48) directly. We prefer the latter, geometric argument to prove (4.49). Indeed, the first term on the right-hand side of (4.49) is the derivative of the first term on the right-hand side of (4.38). Similarly, each term in the sum of (4.49) is the derivative of the corresponding term in the sum of (4.38). Here we get a factor 2 because

$$\partial[B(0,r) \cap B(p,r)] = [\partial B(0,r) \cap B(p,r)] \ \cup [B(0,r) \cap \partial B(p,r)]. \tag{4.52}$$

The two spherical caps on the right-hand side have the same area, so the sum of the areas is twice the area of the first cap. ◻

Equilibrium

In this subsection, we prove that the soft density of the ball configuration defined by a fixed lattice is a unimodal function of the radius. This property holds for the unsimplified as well as the simplified soft densities.

Fraction versus area. For the proof of unimodality, it will be important that the generalized Voronoi domains centered at 0 are star-convex and contain 0 in the interiors of their kernels; see Lemma 16. To see why this is important, we grow a sphere

with center 0. As the radius increases, the fraction of this sphere inside $\mathrm{Vor}^j(0)$ decreases monotonically from 1 to 0. By complementarity, the fraction of the sphere outside $\mathrm{Vor}^j(0)$ increases monotonically from 0 to 1. Plotting the difference between these two fractions as a function of the radius, we get two flat intervals, as shown in Figure 4.12, with a monotonically decreasing segment in between. This segment crosses the zero-line exactly once, at the *equilibrium radius*, which we denote by ϱ_j.

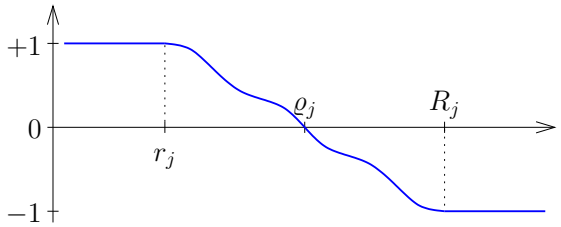

Figure 4.12: The graph of the difference between the fraction of the sphere inside $\mathrm{Vor}^j(0)$ and the complementary fraction outside $\mathrm{Vor}^j(0)$.

Recall that a real-valued function is unimodal if it increases until it attains its maximum, after which it decreases. More formally, we call a differentiable function $f\colon \mathbb{R}_+ \to \mathbb{R}$ *unimodal* if there exists $\varrho \in \mathbb{R}_+$ such that

$$\frac{\partial f}{\partial r}(r) \begin{cases} > 0 & \text{for } r < \varrho, \\ = 0 & \text{for } r = \varrho, \\ < 0 & \text{for } r > \varrho. \end{cases} \tag{4.53}$$

It follows that the integral of the difference of fractions, as sketched in Figure 4.12, is unimodal with equilibrium radius ϱ_j. However, according to (4.48), the derivative of the j-th soft density is the difference between the *normalized areas* of the sphere inside and outside $\mathrm{Vor}^j(0)$, and not the difference between the *fractions*.

Unimodality. The j-th soft density is unimodal with equilibrium radius ϱ_j nonetheless, but this requires a proof.

Lemma 21 (Unimodality)**.** *Let Λ be a lattice in $\mathbb{R}^n$. For each $j \geq 1$, the j-th soft density function of Λ is unimodal, and it attains its maximum at the equilibrium radius of Λ, which satisfies $r_j < \varrho_j < R_j$.*

PROOF. We begin by proving that the fraction of the sphere inside the first j rings is monotonically decreasing. Write

$$F(r) = \frac{\text{area}[S_j(r)]}{\text{area}[\partial B(0,r)]} \tag{4.54}$$

for the fraction and consider radii $r_j \leq r < R \leq R_j$. Associate each point $x \in \partial B(0,r)$ with the point $y = \frac{R}{r}x \in \partial B(0,R)$. Since $\text{Vor}^j(0)$ is star-convex, with 0 in its kernel, $y \in S_j(R)$ implies that $x \in S_j(r)$. Hence, $F(R) \leq F(r)$. To see that the inequality is strict, we use the fact that 0 lies in the interior of the kernel of $\text{Vor}^j(0)$. We can therefore find a non-empty open arc in $S_j(r)$ such that none of the associated points in $\partial B(0,R)$ belongs to $S_j(R)$. This implies that $F(R) < F(r)$. The difference between the normalized areas inside and outside $\text{Vor}^j(0)$ is

$$\Delta(r) = \frac{2\text{area}[S_j(r)] - \text{area}[\partial B(0,r)]}{\text{vol}[\text{Vor}(0)]} = \frac{\text{area}[\partial B(0,r)]}{\text{vol}[\text{Vor}(0)]} \cdot (2F(r) - 1), \tag{4.55}$$

This difference has the same sign as $2F(r) - 1$. Hence,

$$\Delta(r) \begin{cases} > 0 & \text{for } r < \varrho_j, \\ = 0 & \text{for } r = \varrho_j, \\ < 0 & \text{for } r > \varrho_j. \end{cases} \tag{4.56}$$

It follows that δ_j is unimodal and that it attains its maximum at $r = \varrho_j$. We have $r_j < \varrho_j < R_j$ because $2F(r_j) - 1 = 1$ and $2F(R_j) - 1 = -1$. □

REMARK 1. It is not difficult to adapt the proof of Lemma 21 to show that the following parametrized version of the soft density is also unimodal:

$$\delta_{j,C} = \sum_{i=1}^{j} \varphi_i - \tfrac{1}{C-1} \sum_{i=j+1}^{\infty} \varphi_i, \tag{4.57}$$

in which $C > 1$ is a constant. Its equilibrium radius is defined by having a fraction of $1/C$ of the sphere inside $\text{Vor}^j(0)$.

REMARK 2. The proof of Lemma 21 can also be adapted to show that the 1-st simplified soft density is unimodal. To see that $\delta_{1\text{s}}$ is unimodal, we re-normalize by multiplying with $\text{vol}[\text{Vor}(0)]/\text{area}[\partial B(0,r)]$. The first term on the right-hand side of (4.49) becomes identical 1, and the sum becomes strictly increasing. Hence, there is a unique radius at which the difference vanishes. This is the radius at which $\delta_{1\text{s}}$ attains its maximum.

Counterexamples to unimodality. We have chosen our measures of density carefully so that they are unimodal. Many other choices are not unimodal, and some surprisingly so. Consider, for example, $\psi_i \colon \mathbb{R}_+ \to \mathbb{R}$ defined by mapping r to the probability that a randomly selected point is contained in exactly i balls: $\psi_i = \varphi_i - \varphi_{i+1}$. For lattices in $\mathbb{R}^2$, ψ_1 is unimodal, and this was exploited in [Edelsbrunner *et al.*, 2015] to show that the hexagonal lattice provides the maximizing lattice configuration. But already in $\mathbb{R}^3$, ψ_1 is not necessarily unimodal, as we now show. Let

$$a_1 = \begin{bmatrix} 1 \\ 0 \\ 0 \end{bmatrix}, \; a_2 = \begin{bmatrix} 0 \\ 4 \\ 0 \end{bmatrix}, \; a_3 = \begin{bmatrix} 0 \\ 0 \\ 4 \end{bmatrix}. \tag{4.58}$$

The packing radius of the thus defined lattice $\Lambda \subseteq \mathbb{R}^3$ is 0.5. Increasing the radius from 0.0 to 1.0, the probability grows monotonically from $\psi_1(0.0) = 0$ to $\psi_1(1.0) = \frac{\pi}{2}$. Let $D_*(r)$

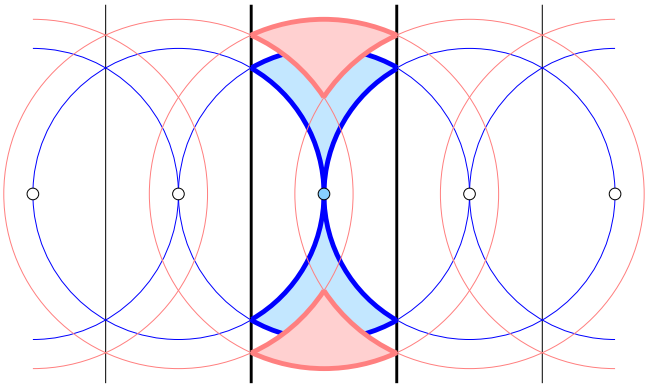

Figure 4.13: Front view of a row of unit spheres and, superimposed, of the same row of slightly enlarged spheres. The shaded sets $D_*(r)$ are contained in the 1-st Voronoi domain of 0.

be the set of points in $B(0,r)$ that are not contained in any other balls (i.e. $2D_1(r) - D_2(r)$). The boundary of $D_*(r)$ consists of points on $\partial B(0,r)$ and of points on other spheres in the configuration. We then write $\partial D_*(r) = S_0(r) \cup S(r)$, with $S_0(r) \subseteq \partial B(0,r)$ and $S(r) \subseteq B(0,r) \backslash \partial B(0,r)$; see Figure 4.13. For $r = 1.0$, Archimedes' theorem implies that the two have the same area. Writing $f(r) = \mathrm{vol}[D_*(r)]$, the derivative vanishes:

$$\frac{\partial f}{\partial r}(1.0) = \mathrm{area}[S_0(1.0)] - \mathrm{area}[S(1.0)] = 0. \tag{4.59}$$

Indeed, if we increase r moderately beyond 1.0, we keep getting constant volume and vanishing derivative. More precisely, we get $f(r) = \frac{\pi}{2}$ for $1.0 \leq r \leq 2.0$, with smaller val-

ues for all other radii. In summary, $\psi_1(r) = f(r)/\mathrm{vol}[\mathrm{Vor}(0)]$ has an interval of maxima, which contradicts unimodality.

Extending this example to four and higher dimensions, it is possible to get functions $\psi_1 \colon \mathbb{R}_+ \to \mathbb{R}$ with multiple local maxima separated from each other by valleys of lower probability.

4.4.3 Optimality in $\mathbb{R}^3$

This section presents the case analysis we use to prove the following Theorem,

Theorem 10 (Main Result)**.** *Among the lattices in the diagonal family in $\mathbb{R}^3$, the FCC lattice with balls of radius $1.090\ldots$ times the packing radius maximizes the soft density at $\delta_1 = 0.844\ldots$.*

As a warm-up exercise, we compute the 1-st soft density of the equilibrium configurations of the FCC lattice in $\mathbb{R}^3$.

FCC lattice. We generate the face centered cubic lattice with the vectors

$$a_1 = \begin{bmatrix} 4/3 \\ 1/3 \\ 1/3 \end{bmatrix},\ a_2 = \begin{bmatrix} 1/3 \\ 4/3 \\ 1/3 \end{bmatrix},\ a_3 = \begin{bmatrix} 1/3 \\ 1/3 \\ 4/3 \end{bmatrix}. \tag{4.60}$$

The packing radius is half the minimum distance between the points, which is $r = \frac{\sqrt{2}}{2}$. The volume of the Voronoi domain is also the volume of the parallelepiped spanned by the generating vectors:

$$\mathrm{vol}[\mathrm{Vor}(0)] = \det \begin{bmatrix} 4/3 & 1/3 & 1/3 \\ 1/3 & 4/3 & 1/3 \\ 1/3 & 1/3 & 4/3 \end{bmatrix} = 2. \tag{4.61}$$

The equilibrium radius is $\varrho = \frac{12}{11} r = \frac{6\sqrt{2}}{11}$. Indeed, at this radius a sphere intersects the neighboring balls in twelve equal and non-intersecting caps, each one twenty-fourth of the area of the sphere. The caps are in the direction of the vectors $\pm a_i$ and $a_i - a_j$, for $i, j \in \{1, 2, 3\}$, and have area

$$\mathrm{A}_{\mathrm{Cap}} = 2\pi\varrho(\varrho - r) = \tfrac{24\pi r^2}{11^2} = 0.311\ldots. \tag{4.62}$$

The volume of a ball is

$$\mathrm{V}_{\mathrm{Ball}} = \mathrm{vol}[B(0,\varrho)] = \tfrac{4\pi}{3}\varrho^3 = \tfrac{16\cdot 12^2\pi r^3}{11^3} = 1.922\ldots. \tag{4.63}$$

The volume of the cone over a cap is one twenty-fourth of this. The boundary of the cap is a circle which spans a disk, and the volume of the cone over this disk is

$$\mathrm{V}_{\mathrm{Cone}} = (\varrho^2 - r^2)\tfrac{r\pi}{3} = \tfrac{23\pi r^3}{3\cdot 11^2} = 0.070\ldots. \tag{4.64}$$

Referring to the difference between a cone over the cap and the cone over the disk as a segment of the ball, we note that its volume is $\mathrm{V}_{\mathrm{Sgmt}} = \frac{1}{24}\mathrm{V}_{\mathrm{Ball}} - \mathrm{V}_{\mathrm{Cone}}$. To finally compute the 1-st soft density, we get φ_1 as the normalized volume of the ball minus twelve segments, φ_2 as the normalized volume of twelve segments, and the 1-st soft density as the difference:

$$\varphi_1 = \tfrac{1}{2}(\tfrac{1}{2}\mathrm{V}_{\mathrm{Ball}} + 12\mathrm{V}_{\mathrm{Cone}}) = \tfrac{1082\pi r^3}{11^3} = \tfrac{541\sqrt{2}\pi}{2\cdot 11^3} = 0.902\ldots, \tag{4.65}$$

$$\varphi_2 = \tfrac{1}{2}(\tfrac{1}{2}\mathrm{V}_{\mathrm{Ball}} - 12\mathrm{V}_{\mathrm{Cone}}) = \tfrac{70\pi r^3}{11^3} = \tfrac{35\sqrt{2}\pi}{2\cdot 11^3} = 0.058\ldots, \tag{4.66}$$

$$\delta_1 = \varphi_1 - \varphi_2 = \tfrac{92\pi r^3}{11^2} = \tfrac{23\sqrt{2}\pi}{11^2} = 0.844\ldots. \tag{4.67}$$

Since there are no triple intersections, this is also the 1-st simplified soft density: $\delta_1 = \delta_{1\mathrm{s}}$. By comparison, the 1-st soft density of the BCC lattice is $0.832\ldots$.

1-parameter family of lattices. We consider the *diagonal family* of lattices introduced in [Edelsbrunner and Kerber, 2011]. Recall that each lattice in this family is obtained by compressing or stretching the integer lattice, $\mathbb{Z}^3$, along the diagonal direction. Writing u_1, u_2, u_3 for the unit coordinate vectors, which span $\mathbb{Z}^3$, and $\mathbf{1} = u_1 + u_2 + u_3$, we define

$$u_i(\varepsilon) = u_i + \tfrac{\varepsilon-1}{3}\cdot\mathbf{1}, \tag{4.68}$$

for $1 \le i \le 3$, and we let Λ_ε be the lattice generated by these vectors. Note that $\langle u_i(\varepsilon), \mathbf{1}\rangle = 1 + (\varepsilon - 1)$, which shows that for $\varepsilon = 0$, all three vectors are orthogonal to $\mathbf{1}$ and therefore not linearly independent. We get a lattice for every $\varepsilon > 0$, and particularly interesting examples are the BCC lattice at $\varepsilon = \frac{1}{2}$, the integer lattice at $\varepsilon = 1$, and the FCC lattice at $\varepsilon = 2$.

For $\varepsilon = 1$, the Voronoi domain is the unit cube, $\mathrm{Vor}(0) = [-\frac{1}{2}, \frac{1}{2}]^3$, which has volume 1. More generally, the Voronoi domain of Λ_ε has volume ε, namely the same

volume as the parallelotope defined by $u_1(\varepsilon)$, $u_2(\varepsilon)$, $u_3(\varepsilon)$. As observed already in [Edelsbrunner and Kerber, 2012], the Voronoi domains for parameters $0 < \varepsilon < 1$ are all combinatorially equivalent, being bounded by eight hexagons and six rectangles. Similarly, the Voronoi domains for $1 < \varepsilon < \infty$ are combinatorially equivalent, being bounded by twelve rhombi; see Figure 4.14. This combinatorial predictability of

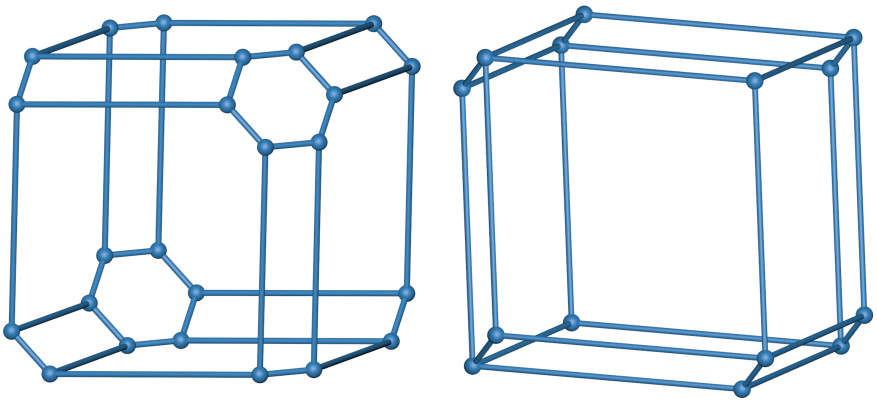

Figure 4.14: The Voronoi domains of Λ_ε, for ε slightly smaller than 1 on the *left*, and for ε slightly larger than 1 on the *right*.

the Voronoi domain enables the detailed analysis in [Edelsbrunner and Kerber, 2011; Iglesias-Ham *et al.*, 2014] as well as in this section. Given a value of the parameter ε and a radius r, we need to determine which faces, edges, and vertices of $\mathrm{Vor}(0)$ intersect $B(0,r)$. Fixing ε, we call r a *critical radius* if there is a face, edge, or vertex of $\mathrm{Vor}(0)$ that touches $B(0,r)$ but is disjoint of its interior. Because of the symmetry of the configuration, there are very few critical radii. For $0 < \varepsilon < 1$, these have already been determined in Section 4.2 (also in [Iglesias-Ham *et al.*, 2014]). With reference to Figure 4.14, they are:

$$f_1(\varepsilon) = \sqrt{(\varepsilon^2+2)/12}, \tag{4.69}$$

$$f_2(\varepsilon) = \sqrt{(2\varepsilon^2+1)/6}, \tag{4.70}$$

$$f_3(\varepsilon) = \sqrt{3}\varepsilon/2, \tag{4.71}$$

$$e_1(\varepsilon) = (\varepsilon^2+2)/(3\sqrt{2}), \tag{4.72}$$

$$e_2(\varepsilon) = \sqrt{(\varepsilon^2+2)(2\varepsilon^2+1)}/(2\sqrt{3}), \tag{4.73}$$

$$v_1(\varepsilon) = \sqrt{8\varepsilon^4+11\varepsilon^2+8}/6, \tag{4.74}$$

corresponding to the 6 square-like hexagons, the 6 rectangles, the 2 small hexagons,

the 18 long edges, the 18 short edges, and the 24 vertices of the polytope on the left in Figure 4.14. Similarly for $1 < \varepsilon < \infty$, we have six critical radii:

$$f_1(\varepsilon) = \sqrt{(\varepsilon^2 + 2)/12}, \tag{4.75}$$

$$f_4(\varepsilon) = \sqrt{2}/2, \tag{4.76}$$

$$e_3(\varepsilon) = \sqrt{6}/3, \tag{4.77}$$

$$e_4(\varepsilon) = (\varepsilon^2 + 2)/\sqrt{12\varepsilon^2 + 6}, \tag{4.78}$$

$$v_2(\varepsilon) = (\varepsilon^2 + 2)/(2\sqrt{3}\varepsilon), \tag{4.79}$$

$$v_3(\varepsilon) = \sqrt{\varepsilon^2 + 8}/(2\sqrt{3}), \tag{4.80}$$

corresponding to the 6 square-like rhombi, the 6 narrow rhombi, the 6 short edges, the 18 long edges, the 8 degree-3 vertices, and 6 degree-4 vertices of the polytope on the right in Figure 4.14. See Appendix D.1 for details.

Soft density at equilibrium. Given a lattice Λ_ε in the diagonal family, we write $\delta_1(\varepsilon) = \max_{r>0} \delta_1(\Lambda_\varepsilon, r)$ for the maximum soft density, and $\delta_{1\mathrm{s}}(\varepsilon) = \max_{r>0} \delta_{1\mathrm{s}}(\Lambda_\varepsilon, r)$ for the maximum simplified soft density. As argued in the preceding sections, the maxima are obtained for the respective equilibrium radii. To compute the maximum soft density of every lattice Λ_ε, we divide $\mathbb{R}_+$ into 12 intervals such that within every interval the expressions and the order of the critical and equilibrium radii are constant. Table 4.1 summarizes the pertinent information for all 12 intervals. Note that in Cases I to IX, the equilibrium radius precedes the critical radii that belong to edges and vertices of the Voronoi domains. Equivalently, the equilibrium configuration contains pairwise but no triplewise overlaps among the balls. In these cases, the soft density equals the simplified soft density: $\delta_1(\varepsilon) = \delta_{1\mathrm{s}}(\varepsilon)$. Indeed, we do all computations for the simplified soft density, which by construction considers only pairwise intersections, and we will find that the FCC lattice maximizes this measure. The equilibrium configuration has triple intersections only for lattices with values of ε larger than that of the FCC lattice, and to prove that the FCC lattice also maximizes the unsimplified soft density, we will finally bound the soft density of these equilibrium configurations from above. To do the computations for the simplified density, we determine the number and type of the spherical caps, and we determine the equilibrium radius, $\varrho = \varrho_1$, at which these caps amount to half the surface area. Note that the number and type of the caps is the same

Case	Critical and Equilibrium Radii	Interval
I	$f_3 \leq \varrho \leq f_1 \leq f_2 \leq e_2 \leq e_1 \leq v_1$	$(0.000\ldots, 0.239\ldots]$
II	$f_3 \leq f_1 \leq \varrho \leq f_2 \leq e_2 \leq e_1 \leq v_1$	$[0.239\ldots, 0.500\ldots]$
III	$f_1 \leq f_3 \leq \varrho \leq f_2 \leq e_1 \leq e_2 \leq v_1$	$[0.500\ldots, 0.617\ldots]$
IV	$f_1 \leq \varrho \leq f_3 \leq f_2 \leq e_1 \leq e_2 \leq v_1$	$[0.617\ldots, 0.632\ldots]$
V	$f_1 \leq \varrho \leq f_2 \leq f_3 \leq e_1 \leq e_2 \leq v_1$	$[0.632\ldots, 0.664\ldots]$
VI	$f_1 \leq \varrho \leq f_2 \leq e_1 \leq f_3 \leq e_2 \leq v_1$	$[0.664\ldots, 1.000\ldots]$
VII	$f_1 \leq \varrho \leq f_4 \leq e_4 \leq e_3 \leq v_2 \leq v_3$	$[1.000\ldots, 1.471\ldots]$
VIII	$f_1 \leq f_4 \leq \varrho \leq e_4 \leq e_3 \leq v_2 \leq v_3$	$[1.471\ldots, 2.000\ldots]$
IX	$f_4 \leq f_1 \leq \varrho \leq e_3 \leq e_4 \leq v_2 \leq v_3$	$[2.000\ldots, 2.342\ldots]$
X	$f_4 \leq f_1 \leq e_3 \leq \varrho \leq e_4 \leq v_2 \leq v_3$	$[2.342\ldots, 2.449\ldots]$
XI	$f_4 \leq e_3 \leq f_1 \leq \varrho \leq e_4 \leq v_2 \leq v_3$	$[2.449\ldots, 2.576\ldots]$
XII	$f_4 \leq e_3 \leq \varrho \leq f_1 \leq e_4 \leq v_2 \leq v_3$	$[2.576\ldots, \infty)$

Table 4.1: The order of the equilibrium radius among the critical radii. Within each of the twelve intervals dividing the positive number line, the order is independent of the parameter ε. Precise expressions for the interval endpoints can be found in Appendix D.

in Cases II and III, in Cases IV to VII, and — because we ignore triple overlaps for the time being — in Cases VIII to XI. The twelve cases thus consolidate to five, which we discuss in sequence.

Case I. Here we have 2 caps, both with critical radius $f_3(\varepsilon)$. At the equilibrium radius, each of the caps covers one quarter of the sphere. Accordingly, the equilibrium radius and the soft density are

$$\varrho(\varepsilon) = \sqrt{3}\varepsilon, \tag{4.81}$$

$$\delta_1(\varepsilon) = \delta_{1\mathrm{s}}(\varepsilon) = 3\sqrt{3}\pi\varepsilon^2/2. \tag{4.82}$$

The derivative of δ_1 is positive in the entire interval, as can be seen in Figure 4.15.

Cases II and III. Here we have 8 caps, 2 with critical radius $f_3(\varepsilon)$ and 6 with critical radius $f_1(\varepsilon)$. At the equilibrium, these caps cover half the sphere. The equilibrium

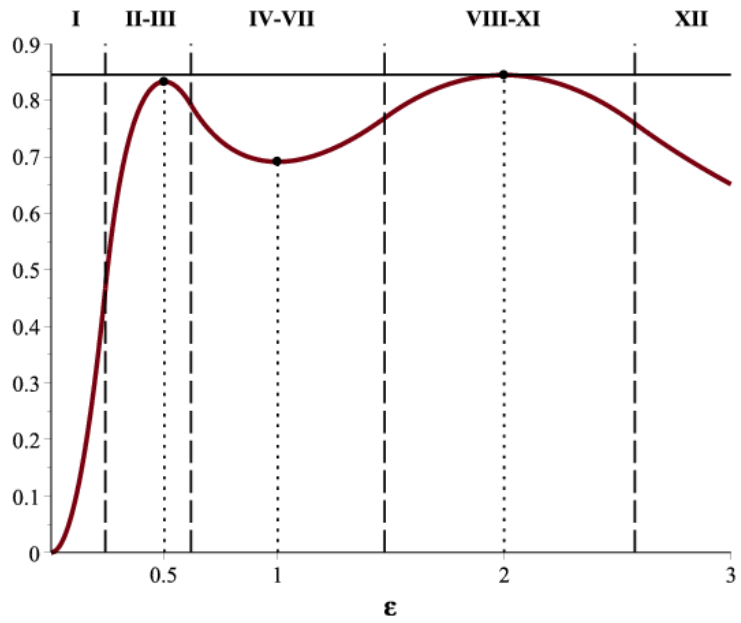

Figure 4.15: The graph of the maximum simplified soft density, $\delta_{1\mathrm{s}}$, as a function of ε, which parametrizes the lattices in the diagonal family. From 0 to $2.342\ldots$, this is identical to the graph of the maximum soft density, δ_1.

radius and the corresponding soft density are

$$\varrho(\varepsilon) = \tfrac{\varepsilon\sqrt{3}+\sqrt{3\varepsilon^2+6}}{7}, \tag{4.83}$$

$$\delta_1(\varepsilon) = \delta_{1\mathrm{s}}(\varepsilon) = \tfrac{\pi[27\sqrt{3}\varepsilon(11\varepsilon^2-8)+(26-95\varepsilon^2)\sqrt{3\varepsilon^2+6}]}{882\varepsilon}. \tag{4.84}$$

The derivative vanishes at $\varepsilon = \frac{1}{2}$, and the second derivative is negative throughout the entire open interval. It follows that δ_1 is concave over the interval, with maximum at $\varepsilon = \frac{1}{2}$, which corresponds to the BCC lattice; see Figure 4.15.

Cases IV to VII. Here we have 6 caps, all with critical radius $f_1(\varepsilon)$. The corresponding equilibrium radius and the corresponding soft density are

$$\varrho(\varepsilon) = \tfrac{\sqrt{3\varepsilon^2+6}}{5}, \tag{4.85}$$

$$\delta_1(\varepsilon) = \delta_{1\mathrm{s}}(\varepsilon) = \tfrac{11\pi\sqrt{(3\varepsilon^2+6)^3}}{1350\varepsilon}. \tag{4.86}$$

The derivative vanishes at $\varepsilon = 1$, and the second derivative is positive throughout the entire open interval. It follows that δ_1 is convex over the interval, with minimum at $\varepsilon = 1$, which corresponds to the integer lattice; see Figure 4.15.

Cases VIII to XI. Here we have 12 caps, 6 each with critical radii $f_1(\varepsilon)$ and $f_4(\varepsilon)$. Ignoring intersections among these caps, we compute the equilibrium radius such that

the total area of the 12 caps equals half the sphere. The equilibrium radius and the corresponding simplified soft density are

$$\varrho(\varepsilon) = \tfrac{\sqrt{3\varepsilon^2+6}+3\sqrt{2}}{11}, \tag{4.87}$$

$$\delta_{1\mathrm{s}}(\varepsilon) = \tfrac{\pi[324\sqrt{2}\varepsilon^2-882\sqrt{2}+(478-85\varepsilon^2)\sqrt{3\varepsilon^2+6}]}{2178\varepsilon}. \tag{4.88}$$

The derivative vanishes at $\varepsilon = 2$, and the second derivative is negative throughout the entire open interval. It follows that δ_1 is concave, with maximum at $\varepsilon = 2$, which corresponds to the FCC lattice; see Figure 4.15.

Case XII. Here we have 6 caps, all with critical radius $f_4(\varepsilon)$. Ignoring intersections among these caps, the equilibrium radius and the corresponding simplified soft density are

$$\varrho(\varepsilon) = \tfrac{3\sqrt{2}}{5}, \tag{4.89}$$

$$\delta_{1\mathrm{s}}(\varepsilon) = \tfrac{11\sqrt{2}\pi}{25\varepsilon}. \tag{4.90}$$

The derivative of $\delta_{1\mathrm{s}}$ is negative throughout the interval.

The above case analysis is summarized in Figure 4.15, which shows the maximum simplified soft density as a function of ε. We see that there are two local maxima separated by a local minimum, with

$$\delta_{1\mathrm{s}}(0.5) = 0.832\ldots, \tag{4.91}$$

$$\delta_{1\mathrm{s}}(1.0) = 0.691\ldots, \tag{4.92}$$

$$\delta_{1\mathrm{s}}(2.0) = 0.844\ldots, \tag{4.93}$$

corresponding to the BCC, the integer, and the FCC lattices, all members of the diagonal family. For $\varepsilon < 2.342\ldots$, the maximum is achieved without triple intersections, which implies that $\delta_1(\varepsilon) = \delta_{1\mathrm{s}}(\varepsilon)$. In particular, (4.91), (4.92), (4.93) remain valid after substituting δ_1 for $\delta_{1\mathrm{s}}$. This is consistent with Theorem 10, which claims that the FCC lattice maximizes the soft density, but it is not quite a proof yet. Indeed, we still need information on the behavior of δ_1 for $\varepsilon > 2.342\ldots$. We will now fill this gap and thus complete the proof of Theorem 10. The main new idea is another measure of density, which we will show majorizes the maximum soft density.

Extrapolated soft density. Consider the FCC lattice, at $\varepsilon = 2$, as described at the beginning of this section. At the equilibrium, the ball centered at the origin intersects 12 other balls whose centers lie in three planes. Specifically, 3 of the 12 centers satisfy $\langle p, \mathbf{1}\rangle = -2$, 6 centers satisfy $\langle p, \mathbf{1}\rangle = 0$, and 3 centers satisfy $\langle p, \mathbf{1}\rangle = 2$. As ε increases, these three planes move apart until the ball at 0 intersects only the 6 balls in the middle plane at equilibrium. For the simplified soft density, this happens for $\varepsilon > 2.576\ldots$, and for the unsimplified soft density it happens a little later, for $\varepsilon > 2.62\ldots$. Within a plane orthogonal to the diagonal, the lattice points do not move, which implies that for all ε larger than some threshold, all equilibrium configurations are the same: a ball surrounded by six others forming a regular hexagon around 0. This corresponds to Case XII. It follows that for each radius r, there are a threshold $\varepsilon_0(r)$ and a constant $C(r)$, such that the soft density has the form

$$\delta_1(\Lambda_\varepsilon, r) = \tfrac{C(r)}{\varepsilon} \tag{4.94}$$

for all $\varepsilon > \varepsilon_0(r)$. Similarly, the equilibrium radius remains constant beyond this threshold, and the maximum soft density satisfies $\delta_1(\varepsilon) = C/\varepsilon$, in which $C = C(\varrho(\varepsilon))$ for large enough ε. Since we define the constant for the unsimplified soft density, it is slightly larger than it would be for the simplified soft density given in (4.90), namely $1.96 > 1.95 \approx 11\sqrt{2}\pi/25$; see Appendix D.4 for details. We define the *extrapolated soft density* as

$$\delta_{1\mathrm{x}}(\Lambda_\varepsilon, r) = \tfrac{C(r)}{\varepsilon}, \tag{4.95}$$

but now for all $\varepsilon > 0$. Similarly $\delta_{1\mathrm{x}}(\varepsilon) = C/\varepsilon$ is the maximum extrapolated soft density. While we define $\delta_{1\mathrm{x}}$ for all positive ε, we are really only interested in $\varepsilon \geq 2.342\ldots$ — the range in which the equilibrium configuration contains triple intersections among the balls. At that parameter value, we have $\delta_{1\mathrm{x}}(2.342\ldots) = 1.96\ldots/2.342\ldots = 0.837\ldots$, which is smaller than $\delta_1(2) = 0.844\ldots$; see Appendix D.4 for the details necessary to see that this inequality is preserved if we use the precise numbers.

Majorization. It remains to prove that the maximum extrapolated soft density majorizes the maximum soft density, which in turn majorizes the maximum simplified soft density.

Lemma 22 (Majorization)**.** *We have*

$$\delta_{1\mathrm{s}}(\varepsilon) \leq \delta_1(\varepsilon) \leq \delta_{1\mathrm{x}}(\varepsilon) \tag{4.96}$$

for all $\varepsilon > 0$*.*

PROOF. We first prove the left inequality. Recall from (4.35) and (4.36) that for a given lattice and a given radius, we have

$$\delta_1(\Lambda, r) = \varphi_1 - \varphi_2 - \varphi_3 - \varphi_4 - \dots, \tag{4.97}$$

$$\delta_{1\mathrm{s}}(\Lambda, r) = \varphi_1 - \varphi_2 - 3\varphi_3 - 5\varphi_4 - \dots. \tag{4.98}$$

This implies that $\delta_{1\mathrm{s}}(\Lambda, r) \leq \delta_1(\Lambda, r)$ for all lattices and all radii. To extend this inequality to the corresponding maxima, we write $\varrho_{1\mathrm{s}}$ for the equilibrium radius of Λ_ε under the simplified soft density. Then

$$\delta_{1\mathrm{s}}(\varepsilon) = \delta_{1\mathrm{s}}(\Lambda_\varepsilon, \varrho_{1\mathrm{s}}) \leq \delta_1(\Lambda_\varepsilon, \varrho_{1\mathrm{s}}) \leq \delta_1(\varepsilon), \tag{4.99}$$

in which the last inequality follows by definition of $\delta_1(\varepsilon)$ as the maximum soft density of Λ_ε.

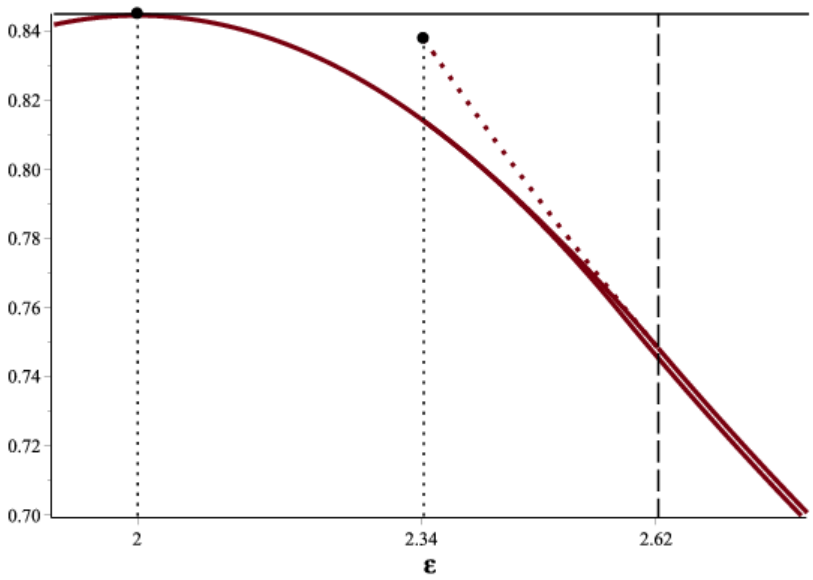

Figure 4.16: A part of the simplified soft density function, with maximum at $\varepsilon = 2$. On the right and slightly above the graph of $\delta_{1\mathrm{s}}$, we see the graph of the soft density function, δ_1, with the dotted extrapolated portion ending at the point $(2.342\dots, 0.837\dots)$.

Second, we prove the right inequality. For a given lattice, Λ_ε, and a given radius, r, we have $\delta_1(\Lambda_\varepsilon, r) \leq \delta_{1\mathrm{x}}(\Lambda_\varepsilon, r)$, simply because the latter accounts for a subset of

the balls that enter the computation of the soft density. Let now $\varrho_1 = \varrho_1(\varepsilon)$ be the equilibrium radius of Λ_ε under the soft density. Then

$$\delta_1(\varepsilon) = \delta_1(\Lambda_\varepsilon, \varrho_1) \leq \delta_{1\mathrm{x}}(\Lambda_\varepsilon, \varrho_1) \leq \delta_{1\mathrm{x}}(\varepsilon), \tag{4.100}$$

in which the last inequality follows by the definition of $\delta_{1\mathrm{x}}(\varepsilon)$ as the maximum extrapolated soft density of Λ_ε. ◻

The two inequalities are illustrated in Figure 4.16. Together with $\delta_{1\mathrm{x}}(2.342\ldots) < \delta_1(2)$, they imply that the FCC lattice at $\varepsilon = 2$ is the unique maximum of δ_1 over the entire diagonal family of lattices. This completes the proof of Theorem 10.

4.5 Discussion

The chapter has covered three main results in the area of the soft sphere packing. In a first approach we analyzed the problem of densest sphere packings while allowing some overlap among the spheres. We see our contributions as a first step towards an interesting and important research direction, given the numerous applications of spheres with overlap in the natural sciences. For example, our analysis of the distance-based overlap measure showing that the FCC lattice is optimal independent of the amount of overlap, and hence independent of the scaling of the spheres, lays the theoretical foundations for [Uhler and Wright., 2013], i.e., for analyzing the spatial organization of chromosomes in the cell nucleus as a sphere arrangement. A major restriction of our approach is our focus on a one-dimensional sub-lattice, the diagonally distorted lattices. Can we hope for an analysis of more general lattice families? This question should probably first be considered in $2D$, given the extremely involved proof of optimality already for the classical packing problem in $3D$.

In a second approach, we proof that the 12-hour clock configuration of disks in the plane maximizes the probability that a random point lies in exactly one of the disks. This is a different criteria that favors configurations between packing and covering that can be formulated, and it would be interesting to decide which one fits the biological data about DNA organization within the nucleus best.

As we know now and as discussed in the introduction of the section, the 12-hour clock configuration is also optimal among all configurations of congruent disks in the

plane [Blind and Blind., 1986]. Then we are left with another concrete mathematical question related to this approach:

- What is the optimal lattice configuration of balls in $\mathbb{R}^3$?

To appreciate the difficulty of the second question, we note that the FCC lattice gives the densest packing [Gauss, 1831], while the BCC lattice gives the sparsest covering [Bambah, 1954]. Does one of them also maximize the probability that a random point lies inside exactly one ball?

In a third approach we extend the results to 3D. The main contributions are the definition of soft density of a lattice sphere configuration and the proof that among the 3-dimensional lattices in the diagonal family introduced in [Edelsbrunner and Kerber, 2011], the 1-st soft density is maximized at the FCC lattice. A key step in the proof of optimality is the unimodality of the soft density for any given lattice. Indeed, unimodality holds for all $j \geq 1$ and all dimensions $n \geq 1$.

Optimal lattices. A difficult question is the determination of the lattices that maximize the j-th soft density. For $j = 1$ and $n = 2$ dimensions, the optimal configuration has been determined in [Balázs, 1973], but for $j \geq 2$, we do not have a proof that the hexagonal lattice provides the optimum. In $n = 3$ dimensions, there are no results beyond what we proved in this chapter, namely that the FCC lattice gives the optimum among the lattices in the diagonal family introduced in [Edelsbrunner and Kerber, 2011].

- Does the FCC lattice give the maximum 1-st soft density among all lattices in $\mathbb{R}^3$?
- What about values of j larger than 1 and dimensions n larger than 3?
- Does the FCC lattice maximize the probability that a random point belongs to exactly one ball of the configuration?

Short of proving that the FCC lattice maximizes δ_1 among all lattices in $\mathbb{R}^3$, it might be possible to use Csikós' formula for the volume derivative [Csikós., 2001] to at least show that the FCC lattice furnishes a local maximum.

Nonlattice configurations. The notion of soft density can be extended to nonlattice configurations of balls: within a region $\Omega \subseteq \mathbb{R}^n$, we compute the probability, φ_i, that a randomly selected point belongs to at least i balls, we set $\delta_j = \varphi_1 + \ldots + \varphi_j - \varphi_{j+1} - \ldots$, we increase Ω, and we finally take the limit. Fixing the centers and growing the balls, we get again a function of the radius, but it is not necessarily unimodal. Indeed, we can define the generalized Voronoi domains of a point p in the configuration as before. Extending Lemma 19 and using the star-convexity of the $\mathrm{Vor}^j(p)$, we can show that the difference between the volume of $B(p, r)$ inside and outside $\mathrm{Vor}^j(p)$ is a unimodal function of r. However, the sum of these unimodal functions over different points in the configuration is not necessarily unimodal. This lack of global unimodality is likely to make progress on soft packing for nonlattice configurations difficult to come by.

5 Applications

In this chapter, we describe the first steps into connecting the theoretical results developed in this thesis with applications. In particular, we represent arrangements of spherical grains by order-2 Voronoi diagrams and show its deformation after shearing. The persistence diagrams of the sequence of arrangements show new information contained in the order-2 Voronoi diagrams that do not appear in the order-1 Voronoi diagrams.

5.1 Prior work and results

Previous studies [Francois *et al.*, 2013], [Klumov *et al.*, 2014] and [Hanifpour *et al.*, 2015], give steps into relating geometrical and topological changes in arrangements of hard spheres with crystallization processes. As a follow-up, [Saadatfar *et al.*, 2017] uses persistent homology to describe different stages in partially crystallized packings. Additionally, it uses simulations to describe the topological changes occurring during the melting of crystals. In particular, persistent homology produces maps of the topological configurations of the spheres, which show the formation of tetrahedral and octahedral pores that are basic components of crystals.

Following [Saadatfar *et al.*, 2017], we use arrangements of spheres from physical simulations. The starting point in these simulations are arrangements of spheres with centers in the FCC lattice or the HCP configuration. When considering arrangements of spheres it is known that the best packing is obtained by the FCC lattice, and that the HCP configuration leads to the same packing density [Hales *et al.*, 2017; Gauss, 1831]. Both the FCC lattice and the HCP configurations can be obtained by stacking shifted versions of the hexagonal lattice on top of each other (See Fig. 5.1). The

first two layers in both cases are the same (a-b). If we repeat them we obtain the HCP configuration (c), while adding the alternative 3rd layer and repeating the triple leads to the FCC arrangement (d). Although using variations of the same construction mechanism we can obtain other sphere arrangements with optimal packing density, the FCC and HCP configurations are more common in nature.

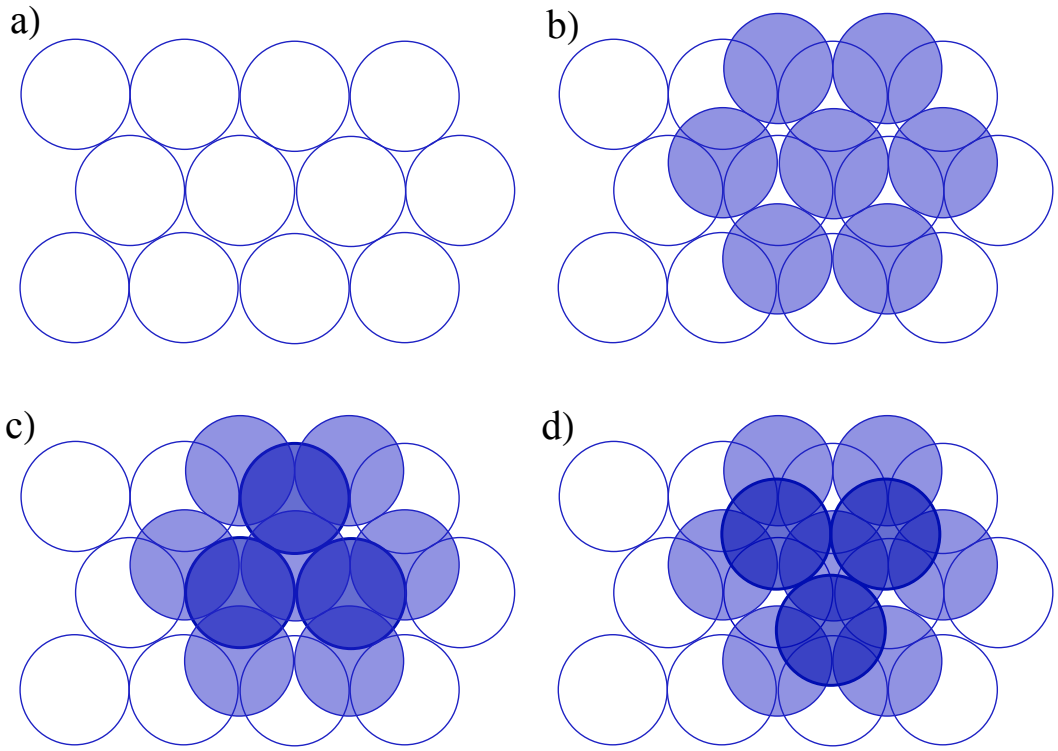

Figure 5.1: FCC and HCP ball configurations built by stacking hexagonal grids on top of each other. a) hexagonal grid at level 0 b) hexagonal grids at levels 0-1 c) levels 0-1-0 for an HCP configuration. Here the 3rd level coincides with the positions at level 0, d) levels 0-1-2 for an FCC configuration.

In this chapter, we show that higher-order representations, in particular the order-2 Voronoi diagrams, contain relevant information that is not present in the commonly used order-1 diagrams. This serves as a first step into exploring the potentials of the k-fold volume formulas as well as other more complex Voronoi decompositions in applications. More precisely: we compute order-2 diagrams from a sequence of arrangements of approximately 2420 spheres, provide two algorithms to compute filtration values representing the growth of the 2-fold region, and compute one of them together with the respective persistence diagrams. We observe that there is new in-

formation in the 0-th and 1-st homology compared to using order-1 Voronoi diagrams. This new information may be found associated with steps in the crystallization and/or melting process of grain arrangements.

Outline. Section 5.2 provides background on persistent homology. Section 5.3 shows a description of the used data, followed by details into the computation of the diagrams and the filtration values in section 5.4. Section 5.5 shows the experimental results, comparing them with the results obtained with the order-1 Voronoi diagram. Section 5.6 concludes the chapter.

5.2 Persistent homology

Persistent homology allows to describe our data from a topological point of view. In this section, we recall basic definitions used in this context for easy reference. Complete literature in the subject can be found in [Munkres, 1984] for general background on homology groups and [Edelsbrunner and Harer, 2010] for background on persistent homology.

Homology. Homology is an algebraic way to describe the connectivity of a topological space. Topological invariants captured are for instance the number of connected components (β_0), the number of holes (β_1) and the number of cavities (β_2). Often, all of them are referred as holes in dimensions zero, one, two or higher. Below, we summarize the main concepts related with its computation.

We need an algebraic structure that contains the building blocks whose union represents the shape of interest. Usually, a simplicial complex K is used, and the building blocks are vertices, edges, triangles, tetrahedra and perhaps higher dimensional simplices. A p-chain is in this context a subset of the p-dimensional simplices. The *sum* of two p-chains is another p-chain, which is the symmetric difference between the two sets of simplices. The boundary of a p-simplex is the set of its $(p-1)$- facets, and the boundary of a p-chain, is the sum of the boundaries of its simplices. A p-cycle, is then a p-chain whose boundary is empty. We restrict ourselves to $\mathbb{Z}/2\mathbb{Z}$ (modulo-2 arithmetic) for simplicity.

A special type of p-cycle comes from the boundary of a $(p+1)$-dimensional chain. This follows from the fact that the boundary of a boundary is always empty. Adding two cycles gives a cycle, as well as adding two boundaries gives another boundary. Therefore, we can call Z_p to the group of p-cycles and B_p to the group of p-boundaries, which leads to the quotient $H_p = Z_p/B_p$. In this way the collection of cycles are partitioned in equivalence classes and two cycles are said to be homologous if their difference is a boundary. The idea is to be able to distinguish between cycles that bound different topological features. For instance, different cycles surrounding the same 1-dimensional hole will be in the same equivalence class, two vertices in the same connected component will be in the same class and so on. In particular, H_0 represents the equivalence class of the 0-cycles and its rank is the betti number β_0, which is the number of connected components of the simplicial complex. H_1 is the equivalence class of the 1-cycles and its rank is the betti number β_1 or number of loops. Lastly, the rank of H_2 is the betti number β_2, or number of voids. We stop at β_2 because in $\mathbb{R}^3$ no other betti numbers are non-zero.

Filtration. The homology of a particular shape depends on the scale that we use to look at the data. At too fine a resolution, a collection of points may look like a large number of independent components, while looking at a lower resolution may reveal more global information of the given shape. Deciding what is the correct scale is not an easy task, depends on the application, on the data, and even on personal perspective. Ideally, we would like to look at all scales observing the shape changes, to decide later in a more impartial way what are the relevant features.

A filtration is a sequence of topological spaces, each contained in the next. As we represent our shape with a simplicial complex, this translates into a sequence of subcomplexes, each a subcomplex of the next, and ending with the full triangulation:

$$\emptyset = K_0 \subseteq K_1 \subseteq \ldots \subseteq K_n = K.$$

Each subcomplex will show the shape of interest in one particular level of detail. In order to construct it, we need to assign to every simplex a real number $f(\sigma)$, which determines from which time on the simplex belongs to the subcomplex. The ordered sequence of simplices is then called a filter, if every simplex is preceded by its faces.

This is $f(\sigma) \leq f(\tau)$ if $\sigma \subseteq \tau$. We order by dimension if $f(\sigma) = f(\tau)$ so all prefixes are complexes. Fixing a filter value α, every simplex with $f(\sigma) \leq \alpha$ belongs to K_α.

Persistence diagrams. Using the filtration for a simplicial complex, we can compute the betti numbers for different levels of detail. As we increase α, these numbers change, showing holes that appear and dissapear for different dimensions. For every hole, one can quantify the lifespan by the difference in α from the time it first appears (*birth*) and the time it dissapears (*death*). The death- birth values are called the persistence of the hole and its used to describe the homology of the data in a scale-invariant way.

The collection of (birth, death) intervals are visualized in different ways. *Barcodes* representations use a *bar* for every interval and they are clustered by dimension. The length of the bar shows the importance or *persistence* of the homology class. More widely used are the persistence diagrams, where every interval is represented by a point in $\mathbb{R}^2$. All the points will lie above the diagonal and the larger the distance to the diagonal the larger its persistence.

5.3 Description of the data

The data described in this section belongs to the experiments performed in [Saadatfar *et al.*, 2017]. Using a computer simulation, a collection of equal-sized spheres were placed once with centers in the FCC lattice (2420 spheres) and another time with centers in the HCP configuration (1960 spheres). The top layers are then set in motion at a constant shear rate and 50 time steps are recorded for computations (See Figure 5.2). The full data consist of 4 different simulation sequences, showing the shearing of arrangements of balls until the packing becomes disordered. This setup represents perfectly crystalline layers of grains that are modified to represent the process of melting of a granular crystal. Each sphere is given in terms of its x, y, z coordinates and its radius.

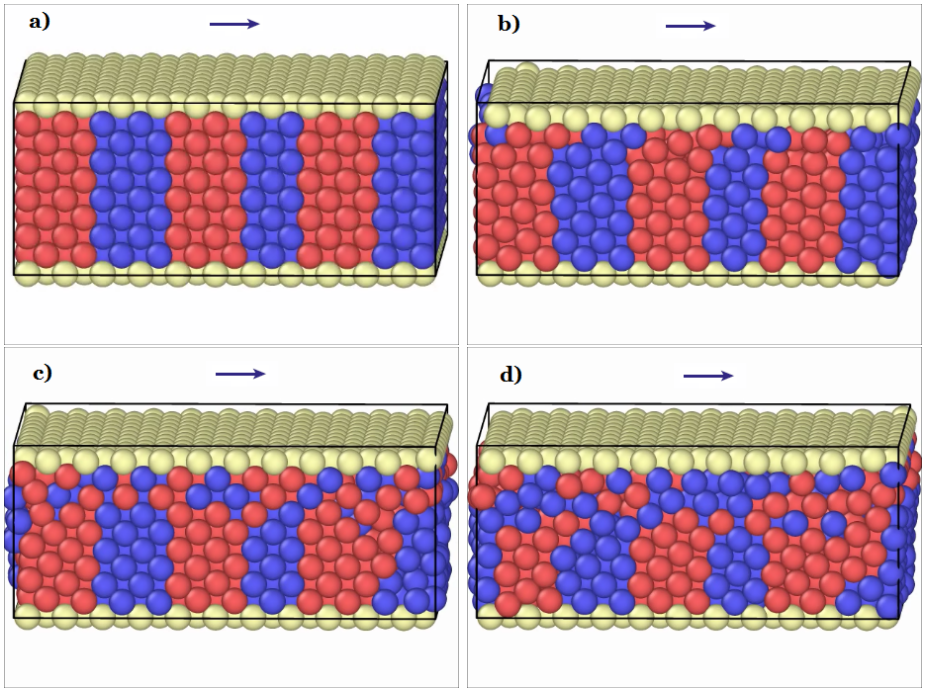

Figure 5.2: Snapshots of the computer simulated packings as it gets disordered.

5.4 Computational details

In this section, we describe details about the computation of the order-2 diagrams and the filtration values obtained from them. Optimizations towards efficiency are left for future work.

5.4.1 Computing the order-2 Voronoi diagram

As described in Chapter 3, the order-k Voronoi diagram can be obtained from the (weighted) order-1 Voronoi diagram of k-fold averages of points. In particular, for $k = 2$, the averages are built from all pairs of balls but not all of them result in a non empty Voronoi domain. Following the same criteria used for $\mathbb{R}^2$ by [Lee, 1982], we find the pairs with non-empty intersection from the order-1 Voronoi diagram. By construction, any two points in the same domain of the order-2 diagram have the same two closest points. Therefore, the corresponding pairs can be obtained from each order-1 Voronoi domain (all with the same closest point) and its immediate neighbors (the second closest points).

Below we enumerate the main steps in terms of the dual Delaunay triangulation:

1. Represent every sphere as a weighted point with weight equal to the squared radius (set *B*).
2. Compute the weighted order-1 Delaunay triangulation of *B*.
3. Traverse all edges and build from the respective pair of vertices an average ball (set $\overline{B}$).
4. Compute the weighted order-1 Delaunay triangulation of $\overline{B}$.

The triangulations are computed with the 3D CGAL weighted Delaunay triangulation software [CGAL]. The worst case complexity is quadratic in the number of points. Although the number of possible pairs is also a quadratic term, in our examples we observe that the number of vertices in the order-2 triangulation (or equivalently the number of edges in the order-1 triangulation) is linear in the number of spheres ($\approx$ 6-7 times the number of vertices in its order-1 version). Indeed, in reasonably dense packings, it is impossible to have superlinear Delaunay triangulations.

5.4.2 Computing the filtration values

In this subsection, we describe the details for computing both the filtration of the growing average balls and the filtration of the growing k-fold volume. Although related, the two filtrations are not the same. In fact, the k-folds show larger or equal filtration values. In the last subsection, we give more details about the relationship.

Filtration of growing average balls

In general, the filtration values represent the moment where the growing average balls meet its dual Voronoi cell using the power distance. The computations are done following the standard method for a weighted alpha shape [Edelsbrunner and Mücke, 1994]. Below, we include a pseudocode with the details about its computation (See Algorithm 1).

The main steps of the algorithm can be described as follows. As input we receive the collection of cells from the weighted Delaunay triangulation. Traversing first over all tetrahedra, we assign the squared radius of its orthogonal sphere, r_σ^2, as the filtration

Algorithm 1 Average balls filtration

1: **procedure** ORDER2FILTRATION($\{\tetrahedron\}$, $\{\triangle\}$, $\{\diagdown\}$, $\{\bullet\}$)

2: **for each** $\sigma \in \{\tetrahedron\}$ **do** ▷ over all tetrahedra

3: $f_{\overline{B}}(\sigma) \leftarrow r_\sigma^2$ ▷ power distance to the weighted circumcenter

4: **end for**

5: **for each** $\sigma \in \{\triangle\}$ **do** ▷ over all triangles

6: **if** *attached* **then**

7: $f_{\overline{B}}(\sigma) \leftarrow f_{\overline{B}}(\tau)$ ▷ τ is the $\tetrahedron$ that $\triangle$ is attached to

8: **else**

9: $f_{\overline{B}}(\sigma) \leftarrow r_\sigma^2$ ▷ from its smallest orthogonal sphere

10: **end if**

11: **end for**

12: **for each** $\sigma \in \{\diagdown\}$ **do** ▷ over all edges

13: **if** *attached* **then**

14: $f_{\overline{B}}(\sigma) \leftarrow \min\{f_{\overline{B}}(\tau)\}$ ▷ τ is the $\triangle$ or $\tetrahedron$ that $\diagdown$ is attached to

15: **else**

16: $f_{\overline{B}}(\sigma) \leftarrow r_\sigma^2$ ▷ from its smallest orthogonal sphere

17: **end if**

18: **end for**

19: **for each** $\sigma \in \{\bullet\}$ **do** ▷ over all vertices

20: **if** *attached* **then**

21: $f_{\overline{B}}(\sigma) \leftarrow \min\{f_{\overline{B}}(\tau)\}$ ▷ τ is the $\diagdown$, $\triangle$ or $\tetrahedron$ that $\bullet$ is attached to

22: **else**

23: $f_{\overline{B}}(\sigma) \leftarrow -\textit{weight}$ ▷ negative squared radius of the average ball or distance from the weighted point to its center

24: **end if**

25: **end for**

26: **end procedure**

value. This is equivalent to the weighted distance from any of the weighted points of the cell to its orthocenter, which coincides with its dual Voronoi cell.

In the case of lower dimensional cells, it is often used the term *attached*. The attachment property for a cell σ, relates to its dual Voronoi cell $\gamma(\sigma)$. A cell is *attached* when the smallest circumsphere of the balls involved in σ is not empty. In other words, the first meeting point of the growing balls involved in σ and the affine space of its dual, do not lie in the interior of $\gamma(\sigma)$. In these cases, the first meeting point of the balls and $\gamma(\sigma)$ coincides with the first meeting point of at least one cofacet of σ and therefore share the same filtration value. It is said then that its meeting point (or filtration value), is attached to the one for the respective cofacet. Notice that a 2-dimensional Delaunay cell has only two cofacets and can be attached to at most one, while lower dimensional cells can be attached to several cofacets. The argument for the 2-dimensional cells is the same as in 2D, and follows from the property that full dimensional Delaunay cells have empty circumspheres.

The triangles, edges and vertices are then traversed and the attachment property is also verified. If the cell is not attached then the filtration value is the weighted distance from any of its balls to its weighted circumcenter. This is equivalent to the squared radius of its smallest orthogonal sphere. Otherwise it takes the minimum filtration value from the cofacets that it is attached to. Notice that for unattached vertices, the ball center lies in its dual Voronoi domain and therefore when the ball shows as a point, it coincides with its filtration value. This is the weighted distance from the ball to its center, which is minus the weight value of the point. Equivalently, the smallest orthogonal ball is the negative ball with the same center and same radius. The weight is also its squared radius but negative for this type of ball.

Filtration of growing 2-folds

The 2-folds filtration is computed in a similar way as the one for the average balls. In this case, the growing shapes are pairwise intersections of balls associated to vertices. The filtration value of a cell coincides with the radius at which all involved 2-folds touch their dual Voronoi cell. See details in the pseudocode provided in Algorithm 2.

Recall from section 2.4 that every cell $\gamma(\sigma)$ of V_k is associated with the subset

Algorithm 2 2-folds filtration (f_{2F}: filtration value for 2-fold)

procedure ORDER2FILTRATION({△}, {△}, {＼}, {•})
  for each $\sigma \in$ {△} **do** ▷ over all tetrahedra
    $f_{2F}(\sigma) \leftarrow \max\{\pi_{a_1}(\mathsf{wc}), \pi_{a_2}(\mathsf{wc})\}$ ▷ wc is the weighted circumcenter of σ
  end for
  for each $\sigma \in$ {△} **do** ▷ over all triangles
    if *attached* **then**
      $f_{2F}(\sigma) \leftarrow f_{2F}(\tau)$ ▷ τ is the △ that △ is attached to
    else
      $f_{2F}(\sigma) \leftarrow \max\{\pi_{a_1}(\mathsf{wkc}), \pi_{a_2}(\mathsf{wkc})\}$
    end if
  end for
  for each $\sigma \in$ {＼} **do** ▷ over all edges
    if *attached* **then**
      $f_{2F}(\sigma) \leftarrow \min\{f_{2F}(\tau)\}$ ▷ τ is the △ or △ that ＼ is attached to
    else
      $f_{2F}(\sigma) \leftarrow \max\{\pi_{a_1}(\mathsf{wkc}), \pi_{a_2}(\mathsf{wkc})\}$
    end if
  end for
  for each $\sigma \in$ {•} **do** ▷ over all vertices
    if *attached* **then**
      $f_{2F}(\sigma) \leftarrow \min\{f_{2F}(\tau)\}$ ▷ τ is the ＼, △ or △ that • is attached to
    else
      $f_{2F}(\sigma) \leftarrow \pi_{a_1}(\mathsf{wc})$ ▷ a_1 and a_2 are at the same distance to wc
    end if
  end for
end procedure

$Q_\gamma \subseteq \mathcal{B}$ of balls that are among the k closest for at least one Voronoi domain containing γ. Assuming general position, we have

$$k \leq \operatorname{card} Q_\gamma \leq k + n. \tag{5.1}$$

For $k = 2$, this means that the number of balls associated with γ is at least 2 and at most 5. However the upper bound is relaxed when we deal with balls in non-general position.

Lets observe this property from another perspective. Consider the level-2 from the hyperplane arrangement of the original balls represented in $\mathbb{R}^4$ (Recall in section 2.3). The projection of the chambers that it bounds from above into $\mathbb{R}^3$ corresponds with the order-2 Voronoi diagram. The cells from the order-2 diagram are a subset of the ones in the level-2 in the arrangement. For every point p in the interior of γ, its corresponding point in the arrangement must lie below up to $k - 1$ hyperplanes and at least $n + 1 - \dim \gamma$ hyperplanes which all meet at γ (the later number is exact with general position assumptions). This means that the point p is closer to the ball represented with the hyperplane above and at equal distance to the at least $4 - \dim \gamma$ meeting at γ. Notice that when considering the distances from the involved balls in σ to a point in the interior of $\gamma(\sigma)$ there are only two possible values, the distance from the hyperplanes meeting at γ, (4 - $\dim \gamma$)-times, and the smaller distance from the hyperplane above γ, at most 1 time. Likewise, every pair of balls, a_1, a_2, from the vertices of σ have the same distances to p, so either the two balls are among the hyperplanes meeting at γ with equal distance, or one of them corresponds to the closer ball.

Another property that needs to be explained is the attachment for a 2-fold filtration. In this case, the smallest circumsphere of the balls involved in σ is a sphere with the 4 - $\dim \gamma$ balls on its boundary, which forces its center, **wkc**, to be in the affine space $A(\gamma(\sigma))$. In order for σ to be unattached, this sphere must be empty except for at most one ball which must be in its interior. This interior ball, if exists, is the one in σ with smaller distance to $\gamma(\sigma)$. Notice, that the referred closest point in $\gamma(\sigma)$, **wkc**, is not necessarily **wc**, the weighted circumcenter of the respective average balls. As a matter of fact, **wkc** corresponds to the center of the minimum enclosing ball for the balls involved in σ. The cell is not attached also when **wkc** lies in the interior of its dual Voronoi cell, i.e. no other balls are closer to it than the ones in σ.

REMARK 3. When the original set of balls are not in general position, the number of balls at the same distance to $A(\gamma(\sigma))$ is larger than 4 - $\dim\gamma$. Any subset of size 4 - $\dim\gamma$ of them will provide the same information (lie in the same affine space). However, when we observe only the pairs involved in one subsimplex product of a subdivision of a Delaunay cell, we need to verify that we get a big enough sample to determine attachment correctly.

The general steps of the algorithm can be then described as follows. Traversing over all tetrahedra we assign the maximum weighted distance from the balls in σ to its weighted circumcenter, $\gamma(\sigma)$. It is enough to consider the distances from the 2 balls, a_1 and a_2, associated with one of the vertices in σ. The moment when the farthest away ball touches $\gamma(\sigma)$ is when all pairwise intersections touch the dual Voronoi cell. Next, we traverse in order the triangles, edges and last the vertices, verifying the attachment property to assign the correct filtration value. In the case of the vertices, the meeting point of the two involved balls is the midpoint, to which both a_1 and a_2 have the same distance. Notice that with a similar argument than for the average balls, the triangles can only be attached to one of its neighbor cofacets, while the lower dimensional cells can be attached to several of them.

Filtration values for k-folds. The filtration for the k-folds can be computed in a similar way. In this case, every cell σ will have $4 - \dim\gamma$ balls with same distance to $\gamma(\sigma)$ and $\ell < k$ balls at closer distance. Similarly, for a cell to be unattached, the smallest circumsphere of the balls in σ, which have the $4 - \dim\gamma$ balls in its boundary, will have to be empty except for the ℓ balls that must be in its interior. Every vertex will have associated k balls and therefore the filtration values when unattached will be of the form $\max\{\pi_{a_1}(\text{wkc}), \ldots, \pi_{a_k}(\text{wkc})\}$. For a vertex, **wkc** is the center of the minimum enclosing ball of its k balls, which should not contain any other point in its interior.

On the correctness of the filtration. For the function defined in this section to serve as a correct filtration, we need to verify that when fixing a filter value α and collecting all simplices with value at most α we get a complete subcomplex. This is the case because every simplex have smaller filtration value than its facets. Observe that when a cell is attached it shares the same value with its smallest cofacet. When it is unattached, the

smallest circumsphere of the balls in σ have a center in the interior of $\gamma(\sigma)$. Likewise, the smallest circumsphere of an unattached cofacet τ, has a center in the interior of $\gamma(\tau)$ (when τ is attached it has a larger value). Also, $\gamma(\tau)$ is on the boundary of $\gamma(\sigma)$ and the balls from σ are a subset of the balls in τ. Being the filtration value the maximum distance to the closest point, and knowing it lies in the interior of $\gamma(\sigma)$, we conclude that the distance to $\gamma(\tau)$ can only be larger.

5.4.3 Containment of k-folds and its average balls.

In this subsection, we compare both filtrations by observing their behavior while growing the original collection of balls.

The filtration values for the average balls are always larger or equal than the ones from the k-folds. This follows from the observation that the k-folds are contained into the respective average balls. The following result about the union and common intersection of a set of balls follows from the Weighted Distance Lemma in section 3.3.

Lemma 23 (Double Containment Lemma)**.** *Let B_0 be a convex combination of balls B_1 to B_k in $\mathbb{R}^n$. Then*

$$\bigcap_{i=1}^{k} B_i \subseteq B_0 \subseteq \bigcup_{i=1}^{k} B_i \tag{5.2}$$

Proof. We prove the first containment relation by showing that $x \in \bigcap_i B_i$ implies $x \in B_0$. Indeed, if x is inside all balls, then all k weighted distances are non-positive. This implies that the weighed average is non-positive and that x is inside B_0. We prove the second containment relation by showing that $x \notin \bigcup_i B_i$ implies $x \notin B_0$. Indeed, if x is outside all balls, then all k weighted distances are positive. This implies that the weighted average is positive and that x is outside B_0. □

Given a ball $B_i = B(x_i, r_i)$, we let B_i^α be the ball with the same center and with squared radius $r_i^2 + \alpha^2$. Write $\mathcal{B}^\alpha = \{B_i^\alpha \mid B_i \in \mathcal{B}\}$ and $\mathbb{U}_k^\alpha = \mathbb{U}_k(\mathcal{B}^\alpha)$. We choose this particular growth model because it leaves the Voronoi diagrams and Delaunay complexes invariant.

Lemma 24 (Constant Diagram Lemma)**.** *Let $\mathcal{B}$ be a finite set of balls in $\mathbb{R}^n$, $j < k$ two integers, and $\alpha^2 \in \mathbb{R}$. Then*

$$V_{j,k}(\mathcal{B}^\alpha) = V_{j,k}(\mathcal{B}), \tag{5.3}$$

$$D_{j,k}(\mathcal{B}^\alpha) = D_{j,k}(\mathcal{B}). \tag{5.4}$$

The proof is straightforward and omitted.

Fixing k and varying α^2 from $-\infty$ to ∞, we get the two filtrations of the order-k Delaunay complex: the complexes $R_k(\mathcal{B}^\alpha)$ for the growing k-folds and the complexes $R(\mathcal{B}_k^\alpha)$ for the growing average balls.

Lemma 25 (Growth Relation Lemma)**.** *Let $\mathcal{B}$ be a finite set of balls in $\mathbb{R}^n$, k an integer, and $\alpha^2 \in \mathbb{R}$. Then*

$$R_k(\mathcal{B}^\alpha) \subseteq R(\mathcal{B}_k^\alpha). \tag{5.5}$$

Proof. The claimed relation follows from the first containment in the Double Containment Lemma, namely that the average contains the common intersection of the balls. □

REMARK 5. The homotopy of the k-folds at a particular radius can come delayed compared with its average balls. An example showing that $R_k(\mathcal{B}^\alpha)$ and $R(\mathcal{B}_k^\alpha)$ do not necessarily have the same homotopy type consists of unit disks B_1, B_2, B_3 centered at the points $(-1.1, 0), (0, 0), (1.1, 0)$. We have non-empty $B_1 \cap B_2$ and $B_2 \cap B_3$. However, $(B_1 \cap B_2) \cap (B_2 \cap B_3) = \emptyset$, while $(\frac{1}{2}B_1 + \frac{1}{2}B_2) \cap (\frac{1}{2}B_2 + \frac{1}{2}B_3) \neq \emptyset$ (See figure 5.3).

5.5 Experiments

In this section, we compute the persistence diagrams for dimensions 0, 1, and 2 from the order-2 Voronoi diagrams. We use the filtration of the average balls and compare with the existing results that use the order-1 Voronoi diagrams.

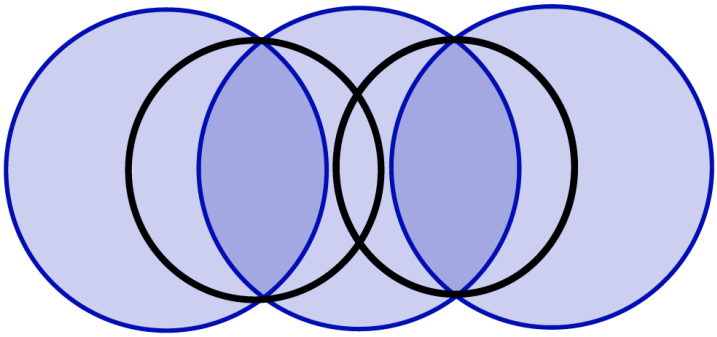

Figure 5.3: Representation of three collinear balls (with larger size), having two connected components in its 2-fold area, while the respective average balls, represented by the two smaller circles, have only one connected component.

5.5.1 Computing the persistence diagrams

We are going to identify the four sequences of simulated arrangements by the configuration of its starting point (FCC lattice or HCP configuration) and the friction parameter used (1, or 0.1). Once a filtration is computed, we use the *phat* library [Bauer *et al.*, 2016] to obtain the persistence pairs. The visualization is done using the maple software [MAPLE].

The persistence diagram is treated as a 2D histogram with bin size 0.005. We count as m, the number of pairs lying in the window of values for every bin. A color code is used then to represent the multiplicity ranging from RGB (0,1,1) as light blue for small values and RGB (1,0,1) as pink for maximal multiplicity. The values are represented in a log scale to show the fine details of the diagram. More precisely, every bin stores the value $log(log(m+1)+1)$ divided by the maximum bin value per arrangement.

In figure 5.4 we show the differences between the persistence diagrams of H_1 using the order-1 and order-2 Voronoi diagrams at three different time steps. See the appearance of a new concentration spot above the diagonal which would be worth to study. Figure 5.5 shows a similar comparison but this time using the H_2 homology. There, although there are also differences its relevance is less clear. Additionally, we compare the plots for H_0 at one particular time steps for illustration in figure 5.6. Not surprisingly, the H_0 persistence diagram using the order-1 Voronoi diagram shows no interesting information, while its order-2 case shows concentration spots possibly about relevant pairs of beads within the arrangement.

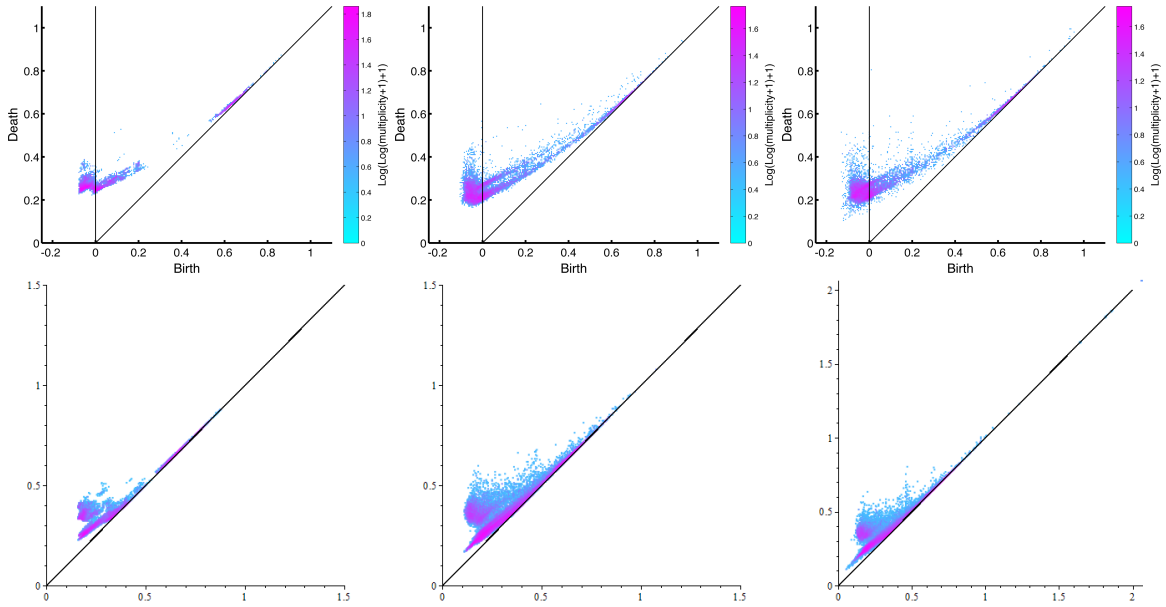

Figure 5.4: H_1 for the sequence FCC-0.1 at time steps 2,18 and 47. Top row uses the order-1 Voronoi diagram and the bottom row the order-2 Voronoi diagram with the filtration of average balls.

5.6 Discussion

In this chapter, we present the first steps into describing arrangements of beads using higher-order Voronoi diagrams. The experiments show there is new information to be analyzed when using order-2 Voronoi diagrams respect with its order-1 versions. However, we find more questions than answers which we would like to explore further in the future. Some of the clear open tasks from a theoretical point of view are:

1. Can we obtain a correct implementation of the k-folds filtration for comparison?
2. Can we bound the distance between both filtrations to know precisely how good of an approximation of the k-folds diagram is the one using the average balls?
3. Can we get a better approximation to the k-folds filtration than the one using average balls?
4. Can we design a Poset diagram that partitions the space in more meaningful regions than the Voronoi regions?

Related to the applications we also wonder:

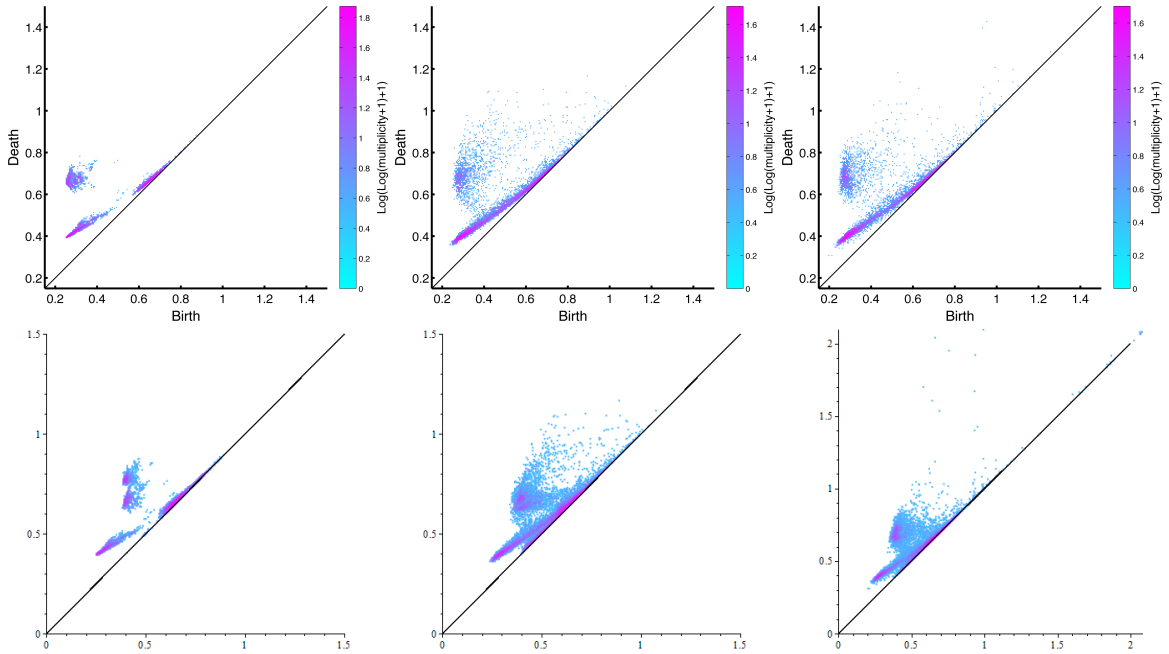

Figure 5.5: H_2 for the sequence FCC-0.1 at time steps 2,18 and 47. Top row uses the order-1 Voronoi diagram and the bottom row the order-2 Voronoi diagram with the filtration of average balls.

1. What are the key structures within the sphere arrangement that produce the concentration points in the persistence diagrams?

2. Are the new concentration points revealing any physical property of the melting of crystals? Can we use the same method to investigate other processes?

3. Do real arrangements of balls resemble optimal soft packing configurations after being subject to external deformation?

   1.1. Can we find a suitable and feasible measure of similarity between an arrangement of balls and a particular lattice, e.g FCC or BCC?

   1.2. Can we correlate the amount of overlap in an arrangement of balls in real data with an optimal soft lattice, i.e. FCC for small overlap and BCC for larger values?

4. Does the 2-fold volume of overlapping spheres in real data say something about the force transmission in the whole system?

5. Could order-3 Voronoi domains be associated with region of interaction of pores?

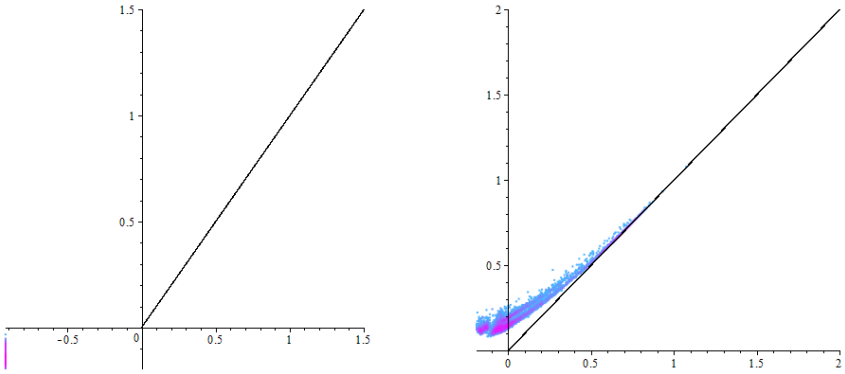

Figure 5.6: H_0 for the sequence FCC-0.1 at time step 18. Left plot uses the order-1 Voronoi diagram and the right plot the order-2 Voronoi diagram with the filtration of average balls.

These are only the first clear questions that remain open at this point. We believe that there must be other application areas where higher-order Voronoi diagrams can also be used to better understand physical or biological processes.

6 Conclusions

We have expanded on the knowledge of α-shapes and union of balls as a first contribution of this thesis. In this respect, we provided formulas for the computation of k-fold coverings from the order-k diagram and the *Level*-k complex. As a next step, it is necessary to find efficient implementations in order to explore its potential in real applications.

We also contribute the theoretical description of the *poset diagrams*, a generalization which contains the order-k and degree-k diagrams as special cases. Poset diagrams allows for more flexible designs to partition the space, which could be advantageous in particular applications.

While sphere packing and covering are well-studied areas, our contributions on the *Soft/Relaxed* sphere packings lie in a less explored area in-between. We have learnt in the process about the very few other existing results. Our findings focus on the soft disk packing of spheres with centers lying on lattice configurations, while the more interesting 3D cases focus only on an interesting subfamily of lattices. Our optimization criteria are only intuitive propositions, and its occurrence on real data is yet to be explored.

We are enthusiastic about the apparent new information found in order-2 Voronoi diagrams using persistent homology. In the future, we plan to further explore the potentials of higher-order diagrams for 3D arrangements of spheres from a topological point of view.

Bibliography

[Aurenhammer, 1990] Franz Aurenhammer, "A new duality result concerning Voronoi diagrams," Discrete & Computational Geometry, **5**(3):243–254, 1990.

[Aurenhammer, 1991] Franz Aurenhammer, "Voronoi Diagrams&Mdash;a Survey of a Fundamental Geometric Data Structure," ACM Comput. Surveys, **23**(3):345–405, 1991.

[Aurenhammer and Schwarzkopf, 1992] Franz Aurenhammer and Otfried Schwarzkopf, "A simple on-line randomized incremental algorithm for computing higher order Voronoi diagrams," International Journal of Computational Geometry & Applications, **2**(4):363–381, 1992.

[Balázs, 1973] J. Balázs, "Über ein Kreisüberdeckungsproblem," Acta Math. Acad. Sci. Hung., **24**:377–382, 1973.

[Bambah, 1954] R.P. Bambah, "On lattice coverings by spheres," Proc. Natl. Inst. Sci. India, **20**:25–52, 1954.

[Bauer *et al.*, 2016] Ulrich Bauer, Michael Kerber, Jan Reininghaus, and Hubert Wagner, "Phat – Persistent Homology Algorithms Toolbox," *Journal of Symbolic Computation*, 78:76–90, 2016.

[Bezdek and Lángi, 2015] K. Bezdek and Z. Lángi, "Density bounds for outer parallel domains of unit ball packings," Proc. Steklov Inst. Math., **288**:209–225, 2015.

[Bieberbach., 1939] L. Bieberbach., "Über die Inhaltsgleichheit der Brillouinschen Zonen.," Monatsh. Math. Phys., **48**:509–515, 1939.

[Blind and Blind., 1986] G. Blind and R. Blind., "Ein Kreisüberdeckungsproblem," Studia Sci. Math. Hung., **21**:35–57, 1986.

[Bock *et al.*, 2010] Martin Bock, Amit Kumar Tyagi, Jan-Ulrich Kreft, and Wolfgang Alt, "Generalized Voronoi Tessellation as a Model of Two-dimensional Cell Tissue Dynamics," Bulletin of Mathematical Biology, **72**, number=7, pages=1696–1731, issn=1522-9602, 2010.

[Borsuk, 1948] Karol Borsuk, "On the imbedding of systems of compacta in simplicial complexes," Fundamenta Mathematicae, **35**(1):217–234, 1948.

[Brillouin, 1930] L. Brillouin, "Les électrons dans les métaux et le classement des ondes de de Broglie correspondantes.," **C.R. 191**:292–294, 1930.

[CGAL] CGAL, *Computational Geometry Algorithms Library*, CGAL Editorial Board, 4.8.1 edition.

[Chen, 1996] Beifang Chen, "The Incidence Algebra of Polyhedra over the Minkowski Algebra," Advances in Mathematics, **118**(2):337 – 365, 1996.

[Conway and Sloane, 1999] J. H. Conway and N. J. A. Sloane, Sphere Packings, Lattices and Groups., Third edition, Springer-Verlag, New York, New York, NY, USA, 1999.

[Cremer and Cremer, 2010] T. Cremer and M. Cremer, "Chromosome territories," Cold Spring Harbor Perspectives in Biology, 2010.

[Cremer *et al.*, 2000] T. Cremer, G. Kreth, H. Koester, R. H. A. Fink, R. Heintzmann, M. Cremer, I. Solovei, D. Zink, and C. Cremer, "Chromosome Territories, Interchromatin Domain Compartment, and Nuclear Matrix: An Integrated View of the Functional Nuclear Architecture," Critical Reviews in Eukaryotic Gene Expression, **10**(2):179–212, 2000.

[Csikós., 2001] B. Csikós., "On the volume of flowers in space forms.," Geometriae Dedicata, **86**:59–79, 2001.

[de Berg *et al.*, 1997] Mark de Berg, Marc van Kreveld, Mark Overmars, and Otfried Schwarzkopf, Computational Geometry: Algorithms and Applications, Springer-Verlag New York, Inc., Secaucus, NJ, USA, 1997.

[DeVries and Baylor, 1997] S. H. DeVries and D. A. Baylor, "Mosaic arrangement of ganglion cell receptive fields in rabbit retina," Journal of Neurophysiology, **78**:2048–2060, 1997.

[Dixon *et al.*, 2012] JR Dixon, S Selvaraj, F Yue, A Kim, Y Li, Y Shen, M Hu, JS Liu, and B Ren, "Topological domains in mammalian genomes identified by analysis of chromatin interactions," Nature, **485**(5):376–380, 2012.

[Edelsbrunner, 1987] Herbert Edelsbrunner, Algorithms in Combinatorial Geometry, Springer-Verlag New York, Inc., New York, NY, USA, 1987.

[Edelsbrunner, 1995a] Herbert Edelsbrunner, "Algebraic decomposition of non-convex polyhedra," In *Proc 36th Annual IEEE Symposium on Foundations of Computer Science*, pages 248–257, 1995.

[Edelsbrunner, 1995b] Herbert Edelsbrunner, "The union of balls and its dual shape," Discrete & Computational Geometry, **13**(1):415–440, 1995.

[Edelsbrunner and Fu, 1994] Herbert Edelsbrunner and Ping Fu, "Measuring space filling diagrams and voids," Technical Report UIUC-BI-MB-94-01, Beckman Institute, Univ Illinois at Urbana-Champaign, Illinois, 1994.

[Edelsbrunner and Harer, 2010] Herbert Edelsbrunner and J. L. Harer, "Computational Topology. An Introduction.," American Mathematical Society*, Providence, Rhode Island*, 2010.

[Edelsbrunner and Iglesias-Ham, 2016] Herbert Edelsbrunner and Mabel Iglesias-Ham, "Multiple Covers with Balls II: Weighted Averages," Electronic Notes in Discrete Mathematics, **54**:169–174, 2016.

[Edelsbrunner and Iglesias-Ham, 2018a] Herbert Edelsbrunner and Mabel Iglesias-Ham, "Multiple Covers with Balls I: Inclusion-Exclusion," *Special Issue in Memoriam: Ferran Hurtado,* Journal of Computational Geometry: Theory and Applications*, CGTA*, **68**:119–133, 2018.

[Edelsbrunner and Iglesias-Ham, 2018b] Herbert Edelsbrunner and Mabel Iglesias-Ham, "On the Optimality of the FCC Lattice for Soft Sphere Packing," SIAM Journal on Discrete Mathematics, **32**(1):750–782, 2018.

[Edelsbrunner *et al.*, 2015] Herbert Edelsbrunner, Mabel Iglesias-Ham, and Vitaliy Kurlin, "Relaxed Disk Packing," Proceedings of the 27th Canadian Conference on Computational Geometry, pages 128–135, 2015.

[Edelsbrunner and Kerber, 2011] Herbert Edelsbrunner and Michael Kerber, "Covering and packing with spheres by diagonal distortion in R^n," *In: G. R. C. Calude, A. Salomaa (eds.)* Rainbow of Computer Science*, Springer Lecture Notes in Computer Science*, **6570**:20–35, 2011.

[Edelsbrunner and Kerber, 2012] Herbert Edelsbrunner and Michael Kerber, "Dual complexes of cubical subdivisions of $\mathbb{R}^n$.," Discrete Comput. Geom., **47**:393–414, 2012.

[Edelsbrunner and Mücke, 1994] Herbert Edelsbrunner and Ernst P. Mücke, "Three-dimensional Alpha Shapes," *ACM Trans. Graph.*, 13(1):43–72, 1994.

[Edelsbrunner and Seidel, 1986] Herbert Edelsbrunner and Raimund Seidel, "Voronoi diagrams and arrangements.," Discrete Comput. Geom., **1**:25–44, 1986.

[Feichtner and Sturmfels, 2005] Eva Maria Feichtner and Bernd Sturmfels, "Matroid polytopes, nested sets and Bergman fans.," *Portugaliae Mathematica. Nova Srie*, 62(4):437–468, 2005.

[Feller, 1968] William Feller, An Introduction to Probability Theory and Its Applications, volume **1**, Third Edition, John Wiley, New York, January 1968.

[Francois *et al.*, 2013] N. Francois, M. Saadatfar, R. Cruikshank, and A. Sheppard, "Geometrical Frustration in Amorphous and Partially Crystallized Packings of Spheres," *Phys. Rev. Lett.*, 111:148001, 2013.

[Gauss, 1831] C.F. Gauss, "Untersuchungen über die Eigenschaften der positiven ternären quadratischen Formen von Ludwig August Seeber," Göttingische Gelehrte Anzeigen *(1831), reprinted in* Werke II*, Königliche Gesellschaften der Wissenschaften*, pages 188–196, 1831.

[Hales *et al.*, 2017] Thomas Hales, MARK ADAMS, GERTRUD BAUER, TAT DAT DANG, JOHN HARRISON, LE TRUONG HOANG, CEZARY KALISZYK, VICTOR

MAGRON, SEAN MCLAUGHLIN, TAT THANG NGUYEN, and et al., "A Formal Proof of the Kepler Conjecture," *Forum of Mathematics, Pi*, 5:e2, 2017.

[Hanifpour *et al.*, 2015] M. Hanifpour, N. Francois, V. Robins, A. Kingston, S. M. Vaez Allaei, and M. Saadatfar, "Structural and mechanical features of the order-disorder transition in experimental hard-sphere packings," *Phys. Rev. E*, 91:062202, 2015.

[Iglesias-Ham *et al.*, 2014] Mabel Iglesias-Ham, Michael Kerber, and Caroline Uhler, "Sphere Packing with Limited Overlap," Proceedings of the 26th Canadian Conference on Computational Geometry, pages 155–161, 2014.

[Karklin and Simoncelli, 2011] Y. Karklin and E. P. Simoncelli, "Efficient coding of natural images with a population of noisy linear-nonlinear neurons," *NIPS*, **24**:999–1007, 2011.

[Kershner, 1939] R. Kershner, "The number of circles covering a set," Amer. J. Math., **61**:665–671, 1939.

[Klumov *et al.*, 2014] Boris A. Klumov, Yuliang Jin, and Hernn A. Makse, "Structural Properties of Dense Hard Sphere Packings," *The Journal of Physical Chemistry B*, 118(36):10761–10766, 2014.

[Kratky, 1978] K W Kratky, "The area of intersection of n equal circular disks," *Journal of Physics A: Mathematical and General*, **11**(6):1017–1024, 1978.

[Kreth *et al.*, 2001] G Kreth, P Edelmann, and C Cremer, "Towards a dynamical approach for the simulation of large scale, cancer correlated chromatin structures," Supplement of Italian Journal of Anatomy and Embryology, **106**(2 Suppl 1):21–30, 2001.

[Lee, 1982] D Lee, "On k-Nearest Neighbor Voronoi Diagrams in the Plane," 31:478 – 487, 1982.

[Leray, 1945] Jean Leray, "Sur la forme des espaces topologiques et sur les points fixes des représentations," Journal de Mathématiques Pures et Appliquées, **24**:95–167, 1945.

[MAPLE] MAPLE, *MAPLE 17*, Maplesoft, a division of Waterloo Maple Inc., Waterloo, Ontario.

[Munkres, 1984] J. R. Munkres, "Elements of Algebraic Topology," *Perseus, Cambridge, Massachusetts*, 1984.

[Naiman and Wynn, 1992] Daniel Q. Naiman and Henry P. Wynn, "Inclusion-exclusion-Bonferroni identities and inequalities for discrete tube-like problems via Euler characteristics," Annals of Statistics, **20**(1):43–76, 03 1992.

[Pedoe, 1988] Daniel Pedoe, Geometry, A Comprehensive Course., Dover Publications, New York, December 1988.

[Raj and Chen, 2011] A. Raj and Y. Chen, "The Wiring Economy Principle: Connectivity Determines Anatomy in the Human Brain," PLoS ONE, **6**, 2011.

[Richards, 1974] F.M. Richards, "The interpretation of protein structures: total volume, group volume distributions and packing density," J. Mol. Biol., **82**:1–14, 1974.

[Rivera-Alba *et al.*, 2011] M. Rivera-Alba, S. N. Vitaladevuni, Y. Mishchenko, Z. Lu, S. Takemura, L. Scheffer, I. A. Meinertzhagen, D. B. Chklovskii, and G. G. de Polavieja, "Wiring Economy and Volume Exclusion Determine Neuronal Placement in the Drosophila Brain," Current Biology, **21**:2000–2005, 2011.

[Saadatfar *et al.*, 2017] M. Saadatfar, H. Takeuchi, V. Robins, N. Francois, and Y. Hiraoka, "Pore configuration landscape of granular crystallization," *Nature Communications*, 2017.

[A.Õ<sc>stnikov.</sc>, 2009] A.Õ<sc>stnikov.</sc>, "<sc>Permutahedra, associahedra, and beyond</sc>," Internat. Math. Res. Notices, **6**:1026–1106, 2009.

[C.Õ<sc>adin.</sc>, 1981] C.Õ<sc>adin.</sc>, "<sc>The ground state for soft disks.</sc>," J. Stat. Physics, **26**:365–373, 1981.

[<sc>Schürmann and Vallentin</sc>, 2006] <sc>Achill Schürmann and Frank Vallentin</sc>, "<sc>Computational Approaches to Lattice Packing and Covering Problems</sc>," Discrete & Computational Geometry, **35**(1):73–116, 2006.

[SHAMOS AND HOEY, 1975] MICHAEL IAN SHAMOS AND DAN HOEY, "CLOSEST-POINT PROBLEMS," IN *Proceedings of the 16th Annual Symposium on Foundations of Computer Science*, FOCS '75, PAGES 151–162, WASHINGTON, DC, USA, 1975. IEEE COMPUTER SOCIETY.

[SIBSON, 1980] R. SIBSON, "A VECTOR IDENTITY FOR THE DIRICHLET TESSELLATION.," Math. Proc. Cambridge Phil. Soc., **87**:151–155, 1980.

[THUE, 1910] A. THUE, "ÜBER DIE DICHTESTE ZUSAMMENSTELLUNG VON KONGRUENTEN KREISEN IN EINER EBENE," Norske Vid. Selsk. Skr., **1**:1–9, 1910.

[TÓTH, 1976] G. FEJES TÓTH, "MULTIPLE PACKING AND COVERING OF THE PLANE WITH CIRCLES," Acta Mathematica Academiae Scientiarum Hungarica, **27**(1):135–140, 1976.

[TÓTH, 1979] G. FEJES TÓTH, "MULTIPLE PACKING AND COVERING OF SPHERES," Acta Mathematica Academiae Scientiarum Hungarica, **34**(1):165–176, 1979.

[TÓTH, 1953] L.FEJES TÓTH, "LAGERUNGEN IN DER EBENE, AUF DER KUGEL UND IM RAUM.," Grundlehren der mathematischen Wissenschaften,*Springer, Berlin, Germany*, **65**, 1953.

[TÓTH., 1964] L. FEJES TÓTH., Regular Figures., MACMILLAN, NEW YORK, NEW YORK, 1964.

[UHLER AND WRIGHT., 2013] C. UHLER AND S. J. WRIGHT., "PACKING ELLIPSOIDS WITH OVERLAP," SIAM Review, **55**:671–706, 2013.

[YAP AND DUBÉ, 1995] C YAP AND T DUBÉ, "THE EXACT COMPUTATION PARADIGM," IN Computing in Euclidean Geometry, PAGES 452–486. 2ND EDITION, EDS D-Z DU AND FK HWANG, WORLD SCIENTIFIC, 1995.

A Appendix - Maximizing the Relaxed Covering Quality

We next briefly analyze the relaxed covering quality and show that in this case the optimum is always attained by the optimal covering configuration. Similarly as for $\mathcal{O}_{\text{dist}}$, we use a linearized measure of the uncovered space $1-\mathcal{U}$. We define it as the largest diameter of a sphere which can be inscribed into the free-space, i.e.:

$$\mathcal{F}(\varepsilon, r) = \max\left(\frac{\max_{p\in\partial\text{Vor}(B_{\text{org}})}\|p\| - r}{r}, 0\right) \tag{A.1}$$

The $\max_{p\in\partial\text{Vor}(B_{\text{org}})}\|p\|$ has been computed in [Edelsbrunner and Kerber, 2011] for the 1-parameter family of lattices under consideration (it corresponds to the covering radius):

$$\max_{p\in\partial\text{Vor}(B_{\text{org}})}\|p\| = \begin{cases} \frac{\sqrt{n^2-1+(n^2+2)\varepsilon^2+(n^2-1)\varepsilon^4}}{\sqrt{12n}} & 0 \le \varepsilon \le 1, \\ \frac{\sqrt{n^2-1+\varepsilon^2}}{2\sqrt{n}} & 1 \le \varepsilon;\ n \text{ odd}, \\ \frac{\sqrt{n^2-2+\varepsilon^2+\frac{1}{\varepsilon^2}}}{2\sqrt{n}} & 1 \le \varepsilon;\ n \text{ even}. \end{cases} \tag{A.2}$$

Using these formulas we can show that the maximum density configuration does not depend on the amount of allowed free-space and is always attained by $\varepsilon = 1/\sqrt{n+1}$, which corresponds to the optimal covering lattice in the family for all $n \ge 2$ and over all lattices in dimension 2-5.

Theorem 11. *The lattice Λ_ε which minimizes the relaxed covering quality w.r.t. $\mathcal{F}$ is attained by $\varepsilon = 1/\sqrt{n+1}$ independent of the value of $\omega \in \mathbb{R}_{\ge 0}$.*

Proof. The proof is analogous to the proof of Theorem 6. The function $\delta(\varepsilon, r(\varepsilon, \omega))$ for $n = 3$ and $\omega = 0.5$ is shown in Figure 4.1 (right). □

B Appendix - Analyzing the 3D Voronoi Cell

In three dimensions, the symmetry between ε and $\frac{1}{\varepsilon}$ is lost, and we need to analyze both branches.

We first discuss the case $0 < \varepsilon \leq 1$: Imagine that r increases from 0 to ∞. Initially, the excess $\mathcal{E}$ is zero. When increasing the ball radius r, there are three possibilities w.r.t. the Voronoi cell $\mathrm{Vor}(B_{\mathrm{org}}) = \mathrm{Vor}(B_{\mathrm{org}})^{\varepsilon}$:

(i) We hit a bisector plane. From now on we have to add a spherical cap to the volume. There are a total of 14 bisector planes of three different types. Their distance to the origin and number of occurrences are:

$f_1(\varepsilon) = \sqrt{\frac{\varepsilon^2+2}{12}}$ (6 planes),
$f_2(\varepsilon) = \sqrt{\frac{2\varepsilon^2+1}{6}}$ (6 planes),
$f_3(\varepsilon) = \frac{\varepsilon\sqrt{3}}{2}$ (2 planes).

(ii) We hit a boundary edge of $\mathrm{Vor}(B_{\mathrm{org}})$, where two bisector planes are meeting. From now on, we have to subtract the volume of the intersection of the two spherical caps involved (because they are counted twice). There are a total of 36 trisector edges of two different types. Their distance to the origin, number of occurrences, and types of bisector planes between the 3 involved spheres are:

$e_1(\varepsilon) := \frac{\varepsilon^2+2}{3\sqrt{2}}$ (18 edges of type 1-1-2),
$e_2(\varepsilon) := \frac{\sqrt{(\varepsilon^2+2)(2\varepsilon^2+1)}}{2\sqrt{3}}$ (18 edges of type 1-2-3).

However, note that the volume of the cap intersection depends on the type of the bisector plane between the two spheres that are not centered at the origin. We get 5 different subtypes, four of them appearing 6 times, and one appearing 12 times in the polytope.

(iii) We hit a boundary vertex of $\mathrm{Vor}(B_{\mathrm{org}})$. All 24 boundary vertices have the same distance to the origin, namely the covering radius

$v_1(\varepsilon) := \frac{1}{6}\sqrt{8\varepsilon^4 + 11\varepsilon^2 + 8}$.

When r exceeds $v_1(\varepsilon)$ the whole Voronoi cell $\mathrm{Vor}(B_{\mathrm{org}})$ is covered, so the excess has volume $\mathrm{vol}[B_{\mathrm{org}}] - \varepsilon$.

Depending on the value of ε we have the following ordering of the critical radii:

$$\begin{aligned}
&f_3(\varepsilon) \le f_1(\varepsilon) \le f_2(\varepsilon) \le e_2(\varepsilon) \le e_1(\varepsilon) \le v_1(\varepsilon) && 0 \le \varepsilon \le 1/2,\\
&f_1(\varepsilon) \le f_3(\varepsilon) \le f_2(\varepsilon) \le e_1(\varepsilon) \le e_2(\varepsilon) \le v_1(\varepsilon) && 1/2 \le \varepsilon \le \sqrt{\tfrac{2}{5}},\\
&f_1(\varepsilon) \le f_2(\varepsilon) \le f_3(\varepsilon) \le e_1(\varepsilon) \le e_2(\varepsilon) \le v_1(\varepsilon) && \sqrt{\tfrac{2}{5}} \le \varepsilon \le \sqrt{\tfrac{19-\sqrt{297}}{4}},\\
&f_1(\varepsilon) \le f_2(\varepsilon) \le e_1(\varepsilon) \le f_3(\varepsilon) \le e_2(\varepsilon) \le v_1(\varepsilon) && \sqrt{\tfrac{19-\sqrt{297}}{4}} \le \varepsilon \le 1.
\end{aligned}$$

So $\mathcal{O}_{\mathrm{vol}}(\varepsilon, r)$ seen as a function in ε has 4 branches. In every branch, the interval which r falls into determines how many and which types of cap intersections have to be taken into account to compute the volume-based overlap.

For $\varepsilon > 1$, a similar analysis can be performed. However, there is one remarkable difference: The vertices of $\mathrm{Vor}(B_{\mathrm{org}})$ are no longer arranged in the same distance around the origin. More precisely, there are 8 vertices at distance $v_2(\varepsilon)$ and 6 vertices at distance $v_3(\varepsilon)$ with

$$v_2(\varepsilon) := \frac{\varepsilon^2 + 2}{2\sqrt{3}\varepsilon}, \qquad v_3(\varepsilon) := \frac{\sqrt{\varepsilon^2 + 8}}{2\sqrt{3}}.$$

Note that $v_2(\varepsilon) < v_3(\varepsilon)$ and $v_3(\varepsilon)$ is the covering radius. So for $\varepsilon > 1$ and $v_2(\varepsilon) < r < v_3(\varepsilon)$ we need to take into account also triple intersections of spherical caps.

C Appendix - 2D Proofs

In this appendix, we give detailed proofs of the three Arc Lemmas. As described in Section 4.3.3, the three lemmas add up to a proof of the Main Theorem stated in Section 4.3 of this thesis. We begin with a few relations that will be useful in all three proofs. Given a triangle with edges of lengths $\|a_1\|, \|a_2\|, \|a_3\|$ and angle γ opposite the edge a_3, the *law of cosines* implies

$$\|a_3\|^2 = \|a_1\|^2 + \|a_2\|^2 - 2\|a_1\|\|a_2\| \cos\gamma. \tag{C.1}$$

Assuming $\|a_1\| \leq \|a_2\| \leq \|a_3\|$, the angle γ is at least as large as each of the other two angles. From (C.1) together with $\|a_2\| \leq \|a_3\|$, we get $\cos\gamma \leq \frac{\|a_1\|}{2\|a_2\|}$. As justified by the Non-obtuse Generators Lemma, we may assume the triangle is non-obtuse, which implies

$$\arccos\tfrac{\|a_1\|}{2\|a_2\|} \leq \gamma \leq \tfrac{\pi}{2}. \tag{C.2}$$

The range of possible angles is largest for $\|a_1\| = \|a_2\|$ where we get $60^\circ \leq \gamma \leq 90^\circ$. Furthermore, we write the angles α_i of the arcs in the convex boundary of the partial disk in terms of the edge lengths and the radius:

$$\cos\tfrac{\alpha_1}{2} = \tfrac{\|a_1\|}{2\varrho}, \tag{C.3}$$

$$\cos\tfrac{\alpha_2}{2} = \tfrac{\|a_2\|}{2\varrho}, \tag{C.4}$$

$$\cos\tfrac{\alpha_3}{2} = \tfrac{\|a_3\|}{2\varrho}. \tag{C.5}$$

The first relation holds provided $\frac{\|a_1\|}{2} \leq \varrho < R_\Lambda$, and similar for the second and third relations. Finally, we note that scaling does not affect the density of a configuration. We can therefore set $\|a_2\| = 1$, which we will do to simplify computations.

Proof of the Two Arcs Lemma. Case 1 is defined by $\frac{\|a_1\|}{2} < \varrho_\Lambda \leq \frac{\|a_2\|}{2}$, which implies $\alpha_1 > 0$ and $\alpha_2 = \alpha_3 = 0$. Since $\sin\alpha_2 = \sin\alpha_3 = 0$, the probability at the equilibrium radius simplifies to

$$P_L(\varrho_\Lambda) = \tfrac{2\varrho_\Lambda^2}{\|a_1\|\|a_2\|\sin\gamma} \cdot \sin\alpha_1 \tag{C.6}$$

$$= \tfrac{\|a_1\|}{\|a_2\|\sin\gamma}, \tag{C.7}$$

where we get the second line by combining $\alpha_1 = \frac{\pi}{2}$ with (C.3) to imply $\varrho_\Lambda = \|a_1\|/\sqrt{2}$. For the remainder of this proof, we normalize by setting $\|a_2\| = 1$. To maximize the probability, we choose $\|a_1\|$ as large as possible and γ as small as possible. From $\|a_1\|/\sqrt{2} = \varrho_\Lambda \leq \frac{1}{2}$, we get $\|a_1\| \leq 1/\sqrt{2}$, and from $\|a_2\| \leq \|a_3\|$ we get $\gamma \geq \arccos\frac{1}{2\sqrt{2}}$. The two parameters can be optimized simultaneously, which gives

$$P_\Lambda(\varrho_\Lambda) = \frac{1}{\sqrt{2}\sin\left(\arccos\frac{1}{2\sqrt{2}}\right)} = 0.755\ldots. \tag{C.8}$$

Proof of the Four Arcs Lemma. Case 2 is defined by $\frac{\|a_2\|}{2} < \varrho_\Lambda \leq \frac{\|a_3\|}{2}$, which implies $\alpha_1 \geq \alpha_2 > 0$ and $\alpha_3 = 0$. The probability at the equilibrium radius is therefore

$$P_\Lambda(\varrho_\Lambda) = \tfrac{2\varrho_\Lambda^2}{\|a_1\|\|a_2\|\sin\gamma} \cdot (\sin\alpha_1 + \sin\alpha_2). \tag{C.9}$$

To get a handle on the maximum of this function, we first write the the sum of $\sin\alpha_1$ and $\sin\alpha_2$ and second the equilibrium radius in terms of other parameters. Using $\cos 2\alpha = \cos^2\alpha - \sin^2\alpha$ and $\cos^2\alpha + \sin^2\alpha = 1$, we get $\cos\alpha_2 = 2\cos^2\frac{\alpha_2}{2} - 1$, and since $\alpha_1 + \alpha_2 = \frac{\pi}{2}$, we have $\sin\alpha_1 = \cos\alpha_2$. Recalling (C.4), we get $\sin\alpha_1 = \|a_2\|^2/(2\varrho_\Lambda^2) - 1$, and recalling (C.3), we get $\sin\alpha_2 = \|a_1\|^2/(2\varrho_\Lambda^2) - 1$. Adding the two relations gives

$$\sin\alpha_1 + \sin\alpha_2 = \tfrac{\|a_1\|^2 + \|a_2\|^2}{2\varrho_\Lambda^2} - 2. \tag{C.10}$$

To find a substitution for the equilibrium radius, we begin with (C.4), use $\frac{\alpha_2}{2} = \frac{\pi}{4} - \frac{\alpha_1}{2}$, and finally apply $\cos(\alpha+\beta) = \cos\alpha\cos\beta - \sin\alpha\sin\beta$:

$$\tfrac{\|a_2\|}{2\varrho_\Lambda} = \cos\left(\tfrac{\pi}{4} - \tfrac{\alpha_1}{2}\right) \tag{C.11}$$

$$= \tfrac{1}{\sqrt{2}}\left(\cos\tfrac{\alpha_1}{2} + \sin\tfrac{\alpha_1}{2}\right). \tag{C.12}$$

Next, we substitute the two trigonometric functions using (C.3) and $\sin^2\alpha = 1 - \cos^2\alpha$. Simplifying the resulting relation and squaring it, we get

$$\varrho_\Lambda^2 = \tfrac{1}{2}\left(\|a_1\|^2 + \|a_2\|^2 - \sqrt{2}\|a_1\|\|a_2\|\right). \tag{C.13}$$

Plugging (C.10) and (C.13) into the equation for the probability and normalizing by setting $\|a_2\| = 1$, we get

$$P_\Lambda(\varrho_\Lambda) = \frac{2\sqrt{2}\|a_1\| - \|a_1\|^2 - 1}{\|a_1\| \sin\gamma} \tag{C.14}$$

$$= \frac{2\sqrt{2}\|a_1\| - \|a_1\|^2 - 1}{\|a_1\| \sqrt{1 - \left(\sqrt{2} - \frac{\|a_1\|^2+1}{2\|a_1\|}\right)^2}} \tag{C.15}$$

where we maximize to get the second line by choosing γ as small as possible. Specifically, γ is implicitly restricted by $\frac{\|a_2\|}{2} < \varrho_\Lambda \leq \frac{\|a_3\|}{2}$, so we can use $4\varrho_\Lambda^2 \leq \|a_3\|^2$ together with (C.1) and (C.13) to get

$$\cos\gamma \leq \sqrt{2} - \frac{\|a_1\|^2 + \|a_2\|^2}{2\|a_1\|\|a_2\|}. \tag{C.16}$$

Checking with the Maple software [MAPLE], we find that the right-hand-side of (C.15) increases in $[0, 1]$ attaining its maximum at $\|a_1\| = 1$. We therefore get $\gamma = \arccos\left(\sqrt{2} - 1\right)$ from (C.16), $\varrho_\Lambda^2 = 1 - 1/\sqrt{2}$ from (C.13), and

$$P_\Lambda(\varrho_\Lambda) = \sqrt{2\sqrt{2} - 2} = 0.910\ldots \tag{C.17}$$

from (C.15).

Proof of the Six Arcs Lemma. Case 3 is defined by $\frac{\|a_3\|}{2} < \varrho_\Lambda < R_\Lambda$, which implies $\alpha_1 \geq \alpha_2 \geq \alpha_3 > 0$. Starting with the expression for the probability given in the Equilibrium Area Lemma, we first express the $\sin\alpha_i$ in terms of the other parameters:

$$\sin\alpha_1 = \frac{\|a_1\|\sqrt{4\varrho_\Lambda^2 - \|a_1\|^2}}{2\varrho_\Lambda^2}, \tag{C.18}$$

$$\sin\alpha_2 = \frac{\|a_2\|\sqrt{4\varrho_\Lambda^2 - \|a_2\|^2}}{2\varrho_\Lambda^2}, \tag{C.19}$$

$$\sin\alpha_3 = 1 - \frac{\left[\|a_1\|\sqrt{4\varrho_\Lambda^2 - \|a_2\|^2} + \|a_2\|\sqrt{4\varrho_\Lambda^2 - \|a_2\|^2}\right]^2}{8\varrho_\Lambda^4}. \tag{C.20}$$

To get (C.18), we use $\sin 2\alpha = 2\sin\alpha\cos\alpha$ with $\alpha = \frac{\alpha_1}{2}$, together with (C.3). To get (C.19), we use the same trigonometric identity with $\alpha = \frac{\alpha_2}{2}$, together with (C.4). To get (C.20), we use the equilibrium condition together with $\sin\alpha_3 = \sin(\frac{\pi}{2} - \alpha_1 - \alpha_2) = \cos(\alpha_1 + \alpha_2) = 1 - 2\sin^2\frac{\alpha_1+\alpha_2}{2}$, and finally substitute $\sin(\alpha+\beta) = \sin\alpha\cos\beta + \sin\beta\cos\alpha$, with $\alpha = \frac{\alpha_1}{2}$ and $\beta = \frac{\alpha_2}{2}$.

To do the same for $\sin\gamma$, we take the cosine of both sides of the equilibrium condition, which is $\frac{\alpha_3}{2} = \frac{\pi}{4} - \frac{\alpha_1}{2} - \frac{\alpha_2}{2}$. Writing $c_i = \cos\frac{\alpha_i}{2}$ and $s_i = \sin\frac{\alpha_i}{2}$, for $i = 1, 2, 3$, and applying standard trigonometric identities, we get

$$c_3 = \tfrac{1}{\sqrt{2}}[c_1c_2 - s_1s_2 + s_1c_2 + c_1s_2]. \tag{C.21}$$

$$c_3^2 = \tfrac{1}{2} + (2c_1c_2^2 - c_1)\sqrt{1 - c_1^2} + (2c_1^2c_2 - c_2)\sqrt{1 - c_2^2}. \tag{C.22}$$

Using (C.3), (C.4), (C.5) and substituting $\|a_3\|^2$ using (C.1), we get the following relation after a few rearrangements:

$$\cos\gamma = \tfrac{\|a_1\|^2+\|a_2\|^2-2}{2\|a_1\|\|a_2\|} - \tfrac{\|a_2\|^2-2\varrho_\Lambda^2}{4\varrho_\Lambda^2\|a_2\|}\sqrt{4\varrho_\Lambda^2 - \|a_1\|^2} - \tfrac{\|a_1\|^2-2\varrho_\Lambda^2}{4\varrho_\Lambda^2\|a_1\|}\sqrt{4\varrho_\Lambda^2 - \|a_2\|^2}. \tag{C.23}$$

Using $\cos^2\gamma = 1 - \sin^2\gamma$, we can substitute $\sin\gamma$ in the formula for $P_\Lambda(\varrho_\Lambda)$. We thus arrived at a relation that gives the probability in terms of $\|a_1\|$, $\|a_2\|$, and ϱ_Λ only. While being lengthy, this relation is readily obtained by plugging (C.18), (C.19), (C.20), and (C.23) into (4.22). We therefore take the liberty to omit the formula here and refer the interested readers to the website of the author [1].

It remains to determine the parameters that maximize the probability. To simplify this task, we normalize by setting $\|a_2\| = 1$. The probability is thus a function of two variables, $\|a_1\|$ and ϱ_Λ. Using the Maple software, we compute the two partial derivatives, $\partial P_\Lambda/\partial\|a_1\|$ and $\partial P_\Lambda/\partial\varrho_\Lambda$. Setting both to zero, we get $\|a_1\| = 1$ matched up with three radius values:

$$\varrho_\Lambda = \tfrac{1}{2}\left(\sqrt{6} - \sqrt{2}\right) = 0.517\ldots, \tag{C.24}$$

$$\varrho_\Lambda = \tfrac{1}{2}\sqrt{C^{\frac{1}{3}} - 1 + C^{-\frac{1}{3}}} = 0.582\ldots, \tag{C.25}$$

$$\varrho_\Lambda = \tfrac{1}{2}\left(\sqrt{6} + \sqrt{2}\right) = 1.931\ldots, \tag{C.26}$$

with $C = 3 + 2\sqrt{2}$. Setting $\|a_1\| = \|a_2\| = 1$, the covering radius depends only on the angle γ, which ranges from $\frac{\pi}{3}$ to $\frac{\pi}{2}$. It is largest for $\gamma = \frac{\pi}{2}$, where $R_\Lambda = \sqrt{2}/2 = 0.707\ldots$. The radius we get at the third root is larger than that and can therefore be excluded. The maximum probability is attained at one of the two remaining roots or along the

[1] A Maple file with the main steps in the formulas related with this appendix is available at `http://mabelih9.wix.com/mabelhome#!publications/cee5`.

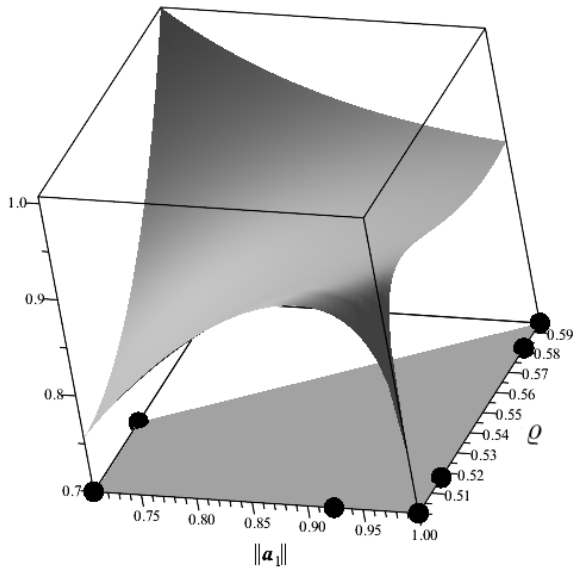

Figure C.1: The quadrangle in the plane defined by the length of a_1 and the radius is shaded. Along its boundary, we encounter three local minima (two corners and a point along the right edge) and three local maxima (a corner and a point each along the lower edge and the right edge).

boundary of the domain region that corresponds to Case 3. As illustrated in Figure C.1, we simplify the computation by taking a quadrangle that contains this region. The quadrangle is defined by

$$\frac{\sqrt{2}}{2} \leq \|a_1\| \leq 1 \tag{C.27}$$

$$\frac{1}{2} \leq \varrho \leq \frac{\|a_3\|}{2\sin\gamma_{max}}, \tag{C.28}$$

in which the first interval follows from the bounds that define Case 3, and the second interval is obtained by limiting the radius by the covering radius of the configuration in which a_1 and a_2 enclose its maximum angle. The maximum angle for Case 3, γ_{max}, corresponds to the minimal angle for Case 2 derived from (C.16). The upper boundary on ϱ is a convex curve and so we replace it with the straight line connecting its extremes.

We evaluate the probability at the four vertices and, using the Maple software, at the roots of the derivatives along the four edges. As shown in Figure C.1, we find three local minima alternating with three local maxima along the boundary of the quadrangle. The maximum and minimum in the interior of the right edge coincide with the roots in (C.24) and (C.25). Among the three local maxima, the probability is largest at (C.24), which is characterized by $\|a_1\| = \|a_2\| = 1$ and $\varrho_\Lambda = \frac{1}{2}\left(\sqrt{6}-\sqrt{2}\right) = 1/(2\cos\frac{\pi}{12})$. This

gives $P_\Lambda(\varrho_\Lambda) = 0.928\ldots$, as claimed in the Six Arcs Lemma. Indeed, plugging the values into the equilibrium condition of Case 3, we get $\|a_3\| = 1$, which shows that the probability is maximized by the regular hexagonal grid.

D Appendix - 3D Case Analysis

In this appendix, we present the computations needed in Section 4.4.3 to determine the maximum soft density as a function of ε, which parametrizes the lattices in the diagonal family. We begin with describing the critical radii of the faces of the Voronoi polytope and continue with finding the positions of the equilibrium radii among the critical radii.

D.1 Critical Radii

The critical radii listed in Section 4.4.3 correspond to the radii at which a growing ball centered at the origin touches different faces of the Voronoi domain; see Table D.1. For $\varepsilon \leq 1$, f_1 corresponds to the 6 square-like hexagons normal to the $\pm u_i(\varepsilon)$, f_2 to the 6 rectangles normal to the $\pm[u_i(\varepsilon) + u_j(\varepsilon)]$, f_3 to the 2 small hexagons normal to $\pm[u_1(\varepsilon)+u_2(\varepsilon)+u_3(\varepsilon)]$, e_1 to the 18 long edges parallel to the vectors $u_i(\varepsilon) \times u_j(\varepsilon)$, e_2 to the 18 short edges parallel to the vectors $u_i(\varepsilon) \times [u_1(\varepsilon)+u_2(\varepsilon)+u_3(\varepsilon)]$, and the covering radius, v_1, corresponding to the 24 vertices of the polytope on the left in Figure 4.14. For $\varepsilon \geq 1$, f_1 corresponds to the 6 square-like rhombi normal to the $\pm u_i(\varepsilon)$, f_4 to the 6 narrow rhombi normal to the $u_i(\varepsilon) - u_j(\varepsilon)$, e_3 to the 6 short edges parallel to the vectors $[u_i(\varepsilon) - u_j(\varepsilon)] \times [u_i(\varepsilon) - u_k(\varepsilon)]$ or, equivalently, parallel to the vector $u_1(\varepsilon)+u_2(\varepsilon)+u_3(\varepsilon)$, e_4 to the 18 long edges parallel to the vectors $u_i(\varepsilon) \times u_j(\varepsilon)$, v_2 to the 8 degree-3 vertices, and the covering radius, v_3, corresponding to the 6 degree-4 vertices of the polytope on the right in Figure 4.14 for $i, j \in \{1, 2, 3\}$ and $\ell, m \in \{2, 3\}$.

After ordering the critical radii, we are left with seven sequences, which we show in Table D.2.

radius	value	vectors
$f_1(\varepsilon)$	$\sqrt{(\varepsilon^2+2)/12}$	$[0, \pm u_i(\varepsilon)]$
$f_2(\varepsilon)$	$\sqrt{(2\varepsilon^2+1)/6}$	$\pm[0, u_i(\varepsilon)+u_j(\varepsilon)]$
$f_3(\varepsilon)$	$\sqrt{3}\varepsilon/2$	$\pm[0, \mathbf{1}(\varepsilon)]$
$e_1(\varepsilon)$	$(\varepsilon^2+2)/(3\sqrt{2})$	$[0, u_i(\varepsilon), -u_j(\varepsilon)]$
		$\pm[0, u_i(\varepsilon), u_i(\varepsilon)+u_j(\varepsilon)]$
$e_2(\varepsilon)$	$\sqrt{(\varepsilon^2+2)(2\varepsilon^2+1)}/(2\sqrt{3})$	$\pm[0, \mathbf{1}(\varepsilon), u_i(\varepsilon)]$
		$\pm[0, \mathbf{1}(\varepsilon), u_i(\varepsilon)+u_j(\varepsilon)]$
		$\pm[0, -u_i(\varepsilon), u_j(\varepsilon)+u_k(\varepsilon)]$
$v_1(\varepsilon)$	$\sqrt{8\varepsilon^4+11\varepsilon^2+8}/6$	$\pm[0, \mathbf{1}(\varepsilon), u_i(\varepsilon), u_i(\varepsilon)+u_j(\varepsilon)]$
		$\pm[0, -u_i(\varepsilon), u_j(\varepsilon)+u_k, u_j(\varepsilon)]$
$f_4(\varepsilon)$	$\sqrt{2}/2$	$u_i(\varepsilon) - u_j(\varepsilon)$
$e_3(\varepsilon)$	$\sqrt{6}/3$	$\pm[0, u_i(\varepsilon)-u_j(\varepsilon), u_i(\varepsilon)-u_k(\varepsilon)]$
$e_4(\varepsilon)$	$(\varepsilon^2+2)/\sqrt{12\varepsilon^2+6}$	$\pm[0, u_i(\varepsilon), u_j(\varepsilon)]$
		$\pm[0, u_i(\varepsilon), u_i(\varepsilon)-u_j(\varepsilon)]$
$v_2(\varepsilon)$	$(\varepsilon^2+2)/(2\sqrt{3}\varepsilon)$	$\pm[0, u_1(\varepsilon), u_2(\varepsilon), u_3(\varepsilon)]$
		$\pm[0, u_i(\varepsilon), u_i(\varepsilon)-u_j(\varepsilon), u_i(\varepsilon)-u_k(\varepsilon)]$
$v_3(\varepsilon)$	$\sqrt{\varepsilon^2+8}/(2\sqrt{3})$	$\pm[0, u_\ell(\varepsilon), u_1(\varepsilon)-u_m(\varepsilon), u_1]$
		$\pm[0, u_\ell(\varepsilon), u_1(\varepsilon)-u_m(\varepsilon), u_\ell(\varepsilon)-u_m(\varepsilon)]$
		$\pm[0, u_\ell(\varepsilon)+u_m(\varepsilon)-u_1, u_\ell(\varepsilon), u_m(\varepsilon)]$
		$\pm[0, u_\ell(\varepsilon)+u_m(\varepsilon)-u_1, u_\ell(\varepsilon), u_\ell(\varepsilon)-u_1(\varepsilon)]$
		$\pm[0, u_\ell(\varepsilon)+u_m(\varepsilon)-u_1, u_\ell(\varepsilon)-u_1(\varepsilon), u_m(\varepsilon)-u_1(\varepsilon)]$

Table D.1: The right column gives the centers of the spheres that define the corresponding critical radius, namely the minimum radius at which these spheres have a non-empty common intersection. Notice that although at radius v_3 only 8 vertices are met, they correspond to the circumcenter of 16 tetrahedra around the origin.

D.2 Position of Equilibrium Radius

Given a constant ordering of the critical radii over an interval of values ε, we find the equilibrium radius by searching in this sequence. At any one step, we consider a particular critical radius, and we compute the area of the sphere covered by the corresponding caps. If this is more than half of the sphere, then the search continues on the

Ordering	Interval
$f_3(\varepsilon) \le f_1(\varepsilon) \le f_2(\varepsilon) \le e_2(\varepsilon) \le e_1(\varepsilon) \le v_1(\varepsilon)$	$0.000\ldots \le \varepsilon \le 0.500\ldots$
$f_1(\varepsilon) \le f_3(\varepsilon) \le f_2(\varepsilon) \le e_1(\varepsilon) \le e_2(\varepsilon) \le v_1(\varepsilon)$	$0.500\ldots \le \varepsilon \le 0.632\ldots$
$f_1(\varepsilon) \le f_2(\varepsilon) \le f_3(\varepsilon) \le e_1(\varepsilon) \le e_2(\varepsilon) \le v_1(\varepsilon)$	$0.632\ldots \le \varepsilon \le 0.664\ldots$
$f_1(\varepsilon) \le f_2(\varepsilon) \le e_1(\varepsilon) \le f_3(\varepsilon) \le e_2(\varepsilon) \le v_1(\varepsilon)$	$0.664\ldots \le \varepsilon \le 1.000\ldots$
$f_1(\varepsilon) \le f_4(\varepsilon) \le e_4(\varepsilon) \le e_3(\varepsilon) \le v_2(\varepsilon) \le v_3(\varepsilon)$	$1.000\ldots \le \varepsilon \le 2.000\ldots$
$f_4(\varepsilon) \le f_1(\varepsilon) \le e_3(\varepsilon) \le e_4(\varepsilon) \le v_2(\varepsilon) \le v_3(\varepsilon)$	$2.000\ldots \le \varepsilon \le 2.449\ldots$
$f_4(\varepsilon) \le e_3(\varepsilon) \le f_1(\varepsilon) \le e_4(\varepsilon) \le v_2(\varepsilon) \le v_3(\varepsilon)$	$2.449\ldots \le \varepsilon$

Table D.2: Sequences of critical radii.

left, and if it is less than half, then the search continues on the right. It is also possible that it switches from more to less than half within the interval, in which case we divide the interval and search in the subintervals independently.

First sequence. Referring to the first two rows in Table 4.1, we note that for $0 < \varepsilon \le 0.5$, the sorted sequence of critical radii is $f_3(\varepsilon) \le f_1(\varepsilon) \le f_2(\varepsilon) \le e_2(\varepsilon) \le e_1(\varepsilon) \le v_1(\varepsilon)$. Recall that the first critical radius is the packing radius and thus precedes the equilibrium radius in all cases. We begin the search by testing the second critical radius. At radius $f_1(\varepsilon)$, the ball intersects two facets of the Voronoi domain, both at distance $f_3(\varepsilon)$ from the origin. We therefore get 2 caps, and using (4.69) and (4.71), we get their height and area as

$$h(\varepsilon) = f_1(\varepsilon) - f_3(\varepsilon) = \tfrac{\sqrt{3\varepsilon^2+6}}{6} - \tfrac{\varepsilon\sqrt{3}}{2}, \tag{D.1}$$

$$A(\varepsilon) = 2\pi f_1(\varepsilon) h(\varepsilon) = \tfrac{\pi(3\varepsilon^2+6) - 9\pi\varepsilon\sqrt{\varepsilon^2+2}}{18}. \tag{D.2}$$

The corresponding *area defect* is a normalized version of (4.49), namely the normalized area of the sphere minus twice the normalized area of the caps:

$$\Delta(\varepsilon) = \tfrac{4\pi f_1^2(\varepsilon) - 4A(\varepsilon)}{\varepsilon} = -\tfrac{\pi\varepsilon}{3} - \tfrac{2\pi}{3\varepsilon} + 2\pi\sqrt{\varepsilon^2+2}. \tag{D.3}$$

With the help of the Maple software [MAPLE], we find that the area defect is negative for $0 < \varepsilon < \sqrt{70}/35 = 0.239\ldots$ and positive in the complementary open interval; see Figure D.1, left graph in top row. We therefore divide the considered interval into two, namely into $(0, 0.239\ldots]$ corresponding to Case I and $[0.239\ldots, 0.5]$ corresponding to Case II; see Table 4.1. In Case I, the equilibrium radius lies between the first two critical

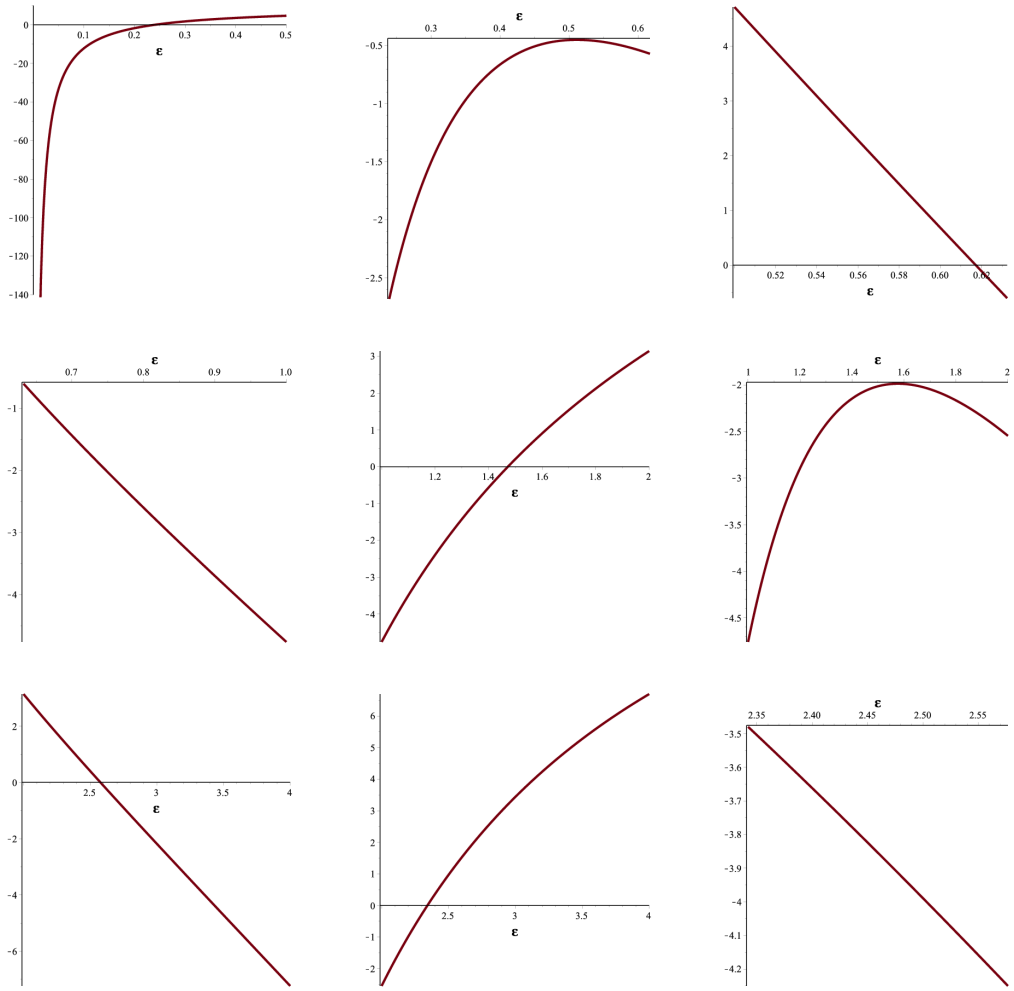

Figure D.1: The graphs of the area defect taken at strategic critical radii. *Top row* from *left* to *right*: at the second critical radius in the interval $(0.00, 0.50]$, at the third critical radius in $[0.239\ldots, 0.632\ldots]$, at the second critical radius in $[0.50, 0.632\ldots]$. *Middle row* from *left* to *right*: at the second critical radius in $[0.632\ldots, 1.00]$, at the second and third critical radii in $[1.00, 2.00]$. *Bottom row* from *left* to *right*: at the second and third critical radii in $[2.00, \infty)$, at the fourth critical radius in $[2.342\ldots, 2.576\ldots]$.

radii and the search is complete. In Case II, the equilibrium radius lies to the right of the second critical radius, and we continue the search by evaluating the area defect at the third critical radius, $f_2(\varepsilon)$. At this size, the ball intersects 6 additional facets of the Voronoi domain, all at distance $f_1(\varepsilon)$ from the origin. We thus deal with two types of caps and index their heights and areas by the subscript of the corresponding critical

radius:

$$h_3(\varepsilon) = f_2(\varepsilon) - f_3(\varepsilon) = \tfrac{\sqrt{12\varepsilon^2+6}}{6} - \tfrac{\varepsilon\sqrt{3}}{2}, \tag{D.4}$$

$$h_1(\varepsilon) = f_2(\varepsilon) - f_1(\varepsilon) = \tfrac{\sqrt{12\varepsilon^2+6}}{6} - \tfrac{\sqrt{3\varepsilon^2+6}}{6}, \tag{D.5}$$

$$A_3(\varepsilon) = 2\pi f_2(\varepsilon) h_3(\varepsilon) = \tfrac{\pi\sqrt{12\varepsilon^2+6}}{3}\,\tfrac{\sqrt{12\varepsilon^2+6}-3\sqrt{3}\varepsilon}{6}, \tag{D.6}$$

$$A_1(\varepsilon) = 2\pi f_2(\varepsilon) h_1(\varepsilon) = \tfrac{\pi\sqrt{12\varepsilon^2+6}}{3}\,\tfrac{\sqrt{12\varepsilon^2+6}-\sqrt{3\varepsilon^2+6}}{6}. \tag{D.7}$$

The corresponding area defect is

$$\begin{aligned}\Delta(\varepsilon) &= \tfrac{4\pi f_2^2(\varepsilon) - 4A_3(\varepsilon) - 12A_1(\varepsilon)}{\varepsilon} \\ &= -\tfrac{14\pi(2\varepsilon^2+1)}{3\varepsilon} + \tfrac{2\pi\sqrt{4\varepsilon^2+2}(\varepsilon+\sqrt{\varepsilon^2+2})}{\varepsilon},\end{aligned} \tag{D.8}$$

which is negative for every ε in the considered interval; see Figure D.1, middle graph in top row. It follows that in Case II, the equilibrium radius lies between the second and third critical radii.

Second sequence. For $0.5 \leq \varepsilon \leq \sqrt{2/5} = 0.632\ldots$, the sorted sequence of critical radii is $f_1(\varepsilon) \leq f_3(\varepsilon) \leq f_2(\varepsilon) \leq e_1(\varepsilon) \leq e_2(\varepsilon) \leq v_1(\varepsilon)$. As before, we begin the search at the second critical radius. The corresponding ball intersects 6 Voronoi facets, all at distance $f_1(\varepsilon)$ from the origin. Using (4.69) and (4.71), we get the height, cap area, and area defect as

$$h(\varepsilon) = f_3(\varepsilon) - f_1(\varepsilon) = \tfrac{\varepsilon\sqrt{3}}{2} - \tfrac{\sqrt{3\varepsilon^2+6}}{6}, \tag{D.9}$$

$$A(\varepsilon) = 2\pi f_3(\varepsilon) h(\varepsilon) = \tfrac{\pi\varepsilon(3\varepsilon-\sqrt{\varepsilon^2+2})}{2}, \tag{D.10}$$

$$\Delta(\varepsilon) = \tfrac{4\pi f_3^2(\varepsilon) - 12A(\varepsilon)}{\varepsilon} = -15\pi\varepsilon + 2\pi\sqrt{9\varepsilon^2+18}. \tag{D.11}$$

The latter is positive for $\varepsilon < 2\sqrt{42}/21 = 0.617\ldots$ and negative for values of ε larger than this bound; see Figure D.1, right graph in top row. We thus divide the considered interval into $[0.5, 0.617\ldots]$ corresponding to Case III and $[0.617\ldots, 0.632\ldots]$ corresponding to Case IV. In Case IV, the equilibrium radius lies between the first two critical radii and the search is complete. In Case III, we continue by evaluating the area defect at $f_2(\varepsilon)$, at which size the ball intersects 2 additional Voronoi facets at distance $f_3(\varepsilon)$ from the origin. The corresponding formulas for the height, cap area, and area defect are the same as (D.4) to (D.8). Again, the area defect is negative, which implies that the equilibrium radius is between $f_3(\varepsilon)$ and $f_2(\varepsilon)$; compare with Table 4.1.

Third sequence. For $0.632\ldots \leq \varepsilon \leq \sqrt{19-3\sqrt{33}}/2 = 0.664\ldots$, the sorted sequence of critical radii is $f_1(\varepsilon) \leq f_2(\varepsilon) \leq f_3(\varepsilon) \leq e_1(\varepsilon) \leq e_2(\varepsilon) \leq v_1(\varepsilon)$. Beginning the search at $f_2(\varepsilon)$, the ball intersects 6 Voronoi facets, all at distance $f_1(\varepsilon)$ from the origin. Using (4.69) and (4.70), we get

$$h(\varepsilon) = f_2(\varepsilon) - f_1(\varepsilon) = \tfrac{\sqrt{12\varepsilon^2+6}-\sqrt{3\varepsilon^2+6}}{6}, \tag{D.12}$$

$$A(\varepsilon) = 2\pi f_2(\varepsilon)h(\varepsilon) = \tfrac{\pi(4\varepsilon^2+2-\sqrt{2(2\varepsilon^2+1)(\varepsilon^2+2)})}{6}, \tag{D.13}$$

$$\Delta(\varepsilon) = \tfrac{4\pi f_2^2(\varepsilon)-12A(\varepsilon)}{\varepsilon} = \tfrac{2\pi(-10\varepsilon^2-5+\sqrt{12\varepsilon^2+6}\sqrt{3\varepsilon^2+6})}{3\varepsilon} \tag{D.14}$$

for the height, cap area, and area defect. The latter is negative for $\varepsilon > \sqrt{22}/8 \approx 0.59$ and therefore within the entire considered interval. In other words, in Case V the equilibrium radius lies between the first and the second critical radii; compare with Table 4.1.

Fourth sequence. For $0.664\ldots \leq \varepsilon \leq 1$, the sorted sequence of critical radii is $f_1(\varepsilon) \leq f_2(\varepsilon) \leq e_1(\varepsilon) \leq f_3(\varepsilon) \leq e_2(\varepsilon) \leq v_1(\varepsilon)$. Beginning the search at $f_2(\varepsilon)$, we get the same formulas for the height, cap area, and area defect as in (D.12) to (D.14). The area defect is negative in the entire interval; see Figure D.1, left graph in middle row. If follows that in Case VI the equilibrium radius lies between the first two critical radii; compare with Table 4.1.

Fifth sequence. For $1 \leq \varepsilon \leq 2$, the sorted sequence of critical radii is $f_1(\varepsilon) \leq f_4(\varepsilon) \leq e_4(\varepsilon) \leq e_3(\varepsilon) \leq v_2(\varepsilon) \leq v_3(\varepsilon)$. Beginning the search at $f_4(\varepsilon)$, the ball intersects 6 Voronoi facets, all at distance $f_1(\varepsilon)$ from the origin. Using (4.75) and (4.76), we get

$$h(\varepsilon) = f_4(\varepsilon) - f_1(\varepsilon) = \tfrac{\sqrt{2}}{2} - \tfrac{\sqrt{3\varepsilon^2+6}}{6}, \tag{D.15}$$

$$A(\varepsilon) = 2\pi f_4(\varepsilon)h(\varepsilon) = \tfrac{\sqrt{2}\pi}{6}\left(3\sqrt{2} - \sqrt{3\varepsilon^2+6}\right), \tag{D.16}$$

$$\Delta(\varepsilon) = \tfrac{4\pi f_4^2(\varepsilon)-12A(\varepsilon)}{\varepsilon} = \tfrac{2\pi\left(\sqrt{6\varepsilon^2+12}-5\right)}{\varepsilon} \tag{D.17}$$

for the height, cap area, and area defect. The latter is negative for $\varepsilon < \sqrt{13/6} = 1.471\ldots$ and positive for values of ε larger than this bound; see Figure D.1, middle graph in middle row. We thus divide the considered interval into $[1, 1.471\ldots]$ corresponding to Case VII and $[1.471\ldots, 2]$ corresponding to Case VIII. In Case VII, the equilibrium radius lies between the first two critical radii and the search is complete; compare

with Table 4.1. In Case VIII, we continue the search with $e_4(\varepsilon)$, at which size the ball intersects all 12 Voronoi facets, 6 each at distances $f_1(\varepsilon)$ and $f_4(\varepsilon)$ from the origin. The heights and areas of the two types of caps and the area defect are

$$h_1(\varepsilon) = e_4(\varepsilon) - f_1(\varepsilon) = \tfrac{\varepsilon^2+2}{\sqrt{6(2\varepsilon^2+1)}} - \tfrac{\sqrt{3\varepsilon^2+6}}{6}, \tag{D.18}$$

$$h_4(\varepsilon) = e_4(\varepsilon) - f_4(\varepsilon) = \tfrac{\varepsilon^2+2}{\sqrt{6(2\varepsilon^2+1)}} - \tfrac{\sqrt{2}}{2}, \tag{D.19}$$

$$A_1(\varepsilon) = 2\pi e_4(\varepsilon) h_1(\varepsilon) = \tfrac{\pi(\varepsilon^2+2)^2}{3(2\varepsilon^2+1)} - \tfrac{\pi(\varepsilon^2+2)\sqrt{\varepsilon^2+2}}{\sqrt{18(2\varepsilon^2+1)}}, \tag{D.20}$$

$$A_4(\varepsilon) = 2\pi e_4(\varepsilon) h_4(\varepsilon) = \tfrac{\pi(\varepsilon^2+2)^2}{3(2\varepsilon^2+1)} - \tfrac{\pi(\varepsilon^2+2)}{\sqrt{3(2\varepsilon^2+1)}}, \tag{D.21}$$

$$\begin{aligned}\Delta(\varepsilon) &= \tfrac{4\pi e_4^2(\varepsilon) - 12A_1(\varepsilon) - 12A_4(\varepsilon)}{\varepsilon} \\ &= \tfrac{2\sqrt{2}\pi(\varepsilon^2+2)(\sqrt{\varepsilon^2+2}+\sqrt{6})}{\varepsilon\sqrt{2\varepsilon^2+1}} - \tfrac{22\pi(\varepsilon^2+2)^2}{3\varepsilon(2\varepsilon^2+1)}.\end{aligned} \tag{D.22}$$

It is negative over the entire interval; see Figure D.1, right graph in middle row. It follows that in Case VIII, the equilibrium radius lies between the second and the third critical radii; compare with Table 4.1.

Sixth sequence. For $2 \le \varepsilon \le \sqrt{6} = 2.449\ldots$, the sorted sequence of critical radii is $f_4(\varepsilon) \le f_1(\varepsilon) \le e_3(\varepsilon) \le e_4(\varepsilon) \le v_2(\varepsilon) \le v_3(\varepsilon)$. Beginning the search at $f_1(\varepsilon)$, the ball intersects 6 Voronoi facets, all at distance $f_4(\varepsilon)$ from the origin. Using (4.75) and (4.76), we get

$$h(\varepsilon) = f_1(\varepsilon) - f_4(\varepsilon) = \tfrac{\sqrt{3\varepsilon^2+6}-3\sqrt{2}}{6}, \tag{D.23}$$

$$A(\varepsilon) = 2\pi f_1(\varepsilon) h(\varepsilon) = \tfrac{\pi(\varepsilon^2+2-\sqrt{6(\varepsilon^2+2)})}{6}, \tag{D.24}$$

$$\begin{aligned}\Delta(\varepsilon) &= \tfrac{4\pi f_1^2(\varepsilon) - 12A(\varepsilon)}{\varepsilon} \\ &= \tfrac{6\pi\sqrt{6(\varepsilon^2+2)} - 5\pi\varepsilon^2 - 10\pi}{3\varepsilon}\end{aligned} \tag{D.25}$$

for the height, cap area, and area defect. The latter is positive for all values of ε in the considered interval; see Figure D.1, left graph in bottom row. We thus continue the search with $e_3(\varepsilon)$, at which size the ball intersects 12 Voronoi facets, 6 each at distances $f_4(\varepsilon)$ and $f_1(\varepsilon)$ from the origin. The corresponding heights, cap areas, and area defect

are

$$h_1(\varepsilon) = e_3(\varepsilon) - f_1(\varepsilon) = \tfrac{2\sqrt{6}-\sqrt{3\varepsilon^2+6}}{6}, \tag{D.26}$$

$$h_4(\varepsilon) = e_3(\varepsilon) - f_4(\varepsilon) = \tfrac{2\sqrt{6}-3\sqrt{2}}{6}, \tag{D.27}$$

$$A_1(\varepsilon) = 2\pi e_3(\varepsilon) h_1(\varepsilon) = \tfrac{\pi(4-\sqrt{2\varepsilon^2+4})}{3}, \tag{D.28}$$

$$A_4(\varepsilon) = 2\pi e_3(\varepsilon) h_4(\varepsilon) = \tfrac{(4-2\sqrt{3})\pi}{3}, \tag{D.29}$$

$$\begin{aligned}\Delta(\varepsilon) &= \tfrac{4\pi e_3^2(\varepsilon) - 12A_1(\varepsilon) - 12A_4(\varepsilon)}{\varepsilon} \\ &= \tfrac{12\sqrt{2}\pi\sqrt{\varepsilon^2+2}+24\sqrt{3}\pi-88\pi}{3\varepsilon}.\end{aligned} \tag{D.30}$$

The latter is negative for $\varepsilon < \sqrt{278 - 132\sqrt{3}}/3 = 2.342\ldots$ and positive for values of ε larger than this bound; see Figure D.1, middle graph in bottom row. We thus divide the considered interval into $[2, 2.342\ldots]$ corresponding to Case IX and $[2.342\ldots, 2.449\ldots]$ corresponding to Case X. In Case IX, the equilibrium radius lies between the second and the third critical radii and the search is complete; see Table 4.1. In Case X, we continue the search with $e_4(\varepsilon)$, at which size the ball still intersects the same 12 Voronoi facets, but some of the corresponding caps overlap. As mentioned earlier, we ignore these overlaps by considering the simplified soft density. We get the same equations for the heights, cap areas, and area defect as above, (D.26) to (D.30), except that we substitute $e_4(\varepsilon)$ for $e_3(\varepsilon)$. We list the corresponding equations for completeness:

$$h_1(\varepsilon) = e_4(\varepsilon) - f_1(\varepsilon) = \tfrac{\varepsilon^2+2}{\sqrt{6(2\varepsilon^2+1)}} - \tfrac{\sqrt{3\varepsilon^2+6}}{6}, \tag{D.31}$$

$$h_4(\varepsilon) = e_4(\varepsilon) - f_4(\varepsilon) = \tfrac{\varepsilon^2+2}{\sqrt{6(2\varepsilon^2+1)}} - \tfrac{\sqrt{2}}{2}, \tag{D.32}$$

$$A_1(\varepsilon) = 2\pi e_4(\varepsilon) h_1(\varepsilon) = \tfrac{\pi(\varepsilon^2+2)^2}{3(2\varepsilon^2+1)} - \tfrac{\pi(\varepsilon^2+2)\sqrt{3\varepsilon^2+6}}{3\sqrt{6(2\varepsilon^2+1)}}, \tag{D.33}$$

$$A_4(\varepsilon) = 2\pi e_4(\varepsilon) h_4(\varepsilon) = \tfrac{\pi(\varepsilon^2+2)^2}{3(2\varepsilon^2+1)} - \tfrac{\pi(\varepsilon^2+2)}{\sqrt{3(2\varepsilon^2+1)}}, \tag{D.34}$$

$$\begin{aligned}\Delta(\varepsilon) &= \tfrac{4\pi e_4^2(\varepsilon) - 12A_1(\varepsilon) - 12A_4(\varepsilon)}{\varepsilon} \\ &= \tfrac{\pi(6\sqrt{2(\varepsilon^2+2)(2\varepsilon^2+1)}+12\sqrt{6\varepsilon^2+3}-22\varepsilon^2-44)(\varepsilon^2+2)}{3\varepsilon(2\varepsilon^2+1)}.\end{aligned} \tag{D.35}$$

The area defect is negative for all $\varepsilon > 0$, which covers the interval of interest; see Figure D.1, right graph in bottom row. It follows that in Case X, the equilibrium radius lies between $e_3(\varepsilon)$ and $e_4(\varepsilon)$; compare with Table 4.1.

Last sequence. For $2.449\ldots \leq \varepsilon < \infty$, the sorted sequence of critical radii is $f_4(\varepsilon) \leq e_3(\varepsilon) \leq f_1(\varepsilon) \leq e_4(\varepsilon) \leq v_2(\varepsilon) \leq v_3(\varepsilon)$. Beginning the search at $e_3(\varepsilon)$, the ball intersects

6 Voronoi facets, all at distance $f_4(\varepsilon)$ from the origin. Using (4.76) and (4.77), we get

$$h(\varepsilon) = e_3(\varepsilon) - f_4(\varepsilon) = \tfrac{2\sqrt{6}-3\sqrt{2}}{6}, \tag{D.36}$$

$$A(\varepsilon) = 2\pi e_3(\varepsilon) h(\varepsilon) = \tfrac{(4-2\sqrt{3})\pi}{3}, \tag{D.37}$$

$$\Delta(\varepsilon) = \tfrac{4\pi e_3^2(\varepsilon) - 12A(\varepsilon)}{\varepsilon} = \tfrac{8\pi(3\sqrt{3}-5)}{3\varepsilon} \tag{D.38}$$

for the height, cap area, and area defect. The latter is positive over the entire interval. We thus continue the search at $f_1(\varepsilon)$. Ignoring overlaps by considering the simplified soft density, we get the same formulas as in (D.23) to (D.25). The area defect is positive for $\varepsilon < \sqrt{166}/5 = 2.576\ldots$ and negative for ε exceeding this bound; see Figure D.1, left graph in bottom row. We thus divide the interval into $[2.449\ldots, 2.576\ldots]$ corresponding to Case XI and $[2.576\ldots, \infty)$ corresponding to Case XII. In Case XII, the equilibrium radius lies between $e_3(\varepsilon)$ and $f_1(\varepsilon)$ and the search is complete; compare with Table 4.1. In Case XI, we continue the search at $e_4(\varepsilon)$. Ignoring overlaps among the caps, we get the same formulas as in (D.31) to (D.35). The area defect is negative for all values of ε in the interval of interest; see Figure D.1, right graph in bottom row. It follows that the equilibrium radius in Case XI is between $f_1(\varepsilon)$ and $e_4(\varepsilon)$; compare with Table 4.1.

D.3 Maximum Soft Density

After identifying the position of the equilibrium radius among the critical radii in Appendix D.2, we now compute the equilibrium radius as well as the corresponding soft density. By construction, this is the maximum soft density for any given parameter ε and thus gives the graph displayed in Figure 4.15. We consider Cases I to XII in turn but consolidate the twelve cases to five.

Case I. Referring to Table 4.1, we recall that for all $\varepsilon \in (0, 0.239\ldots]$, the equilibrium radius lies between the first two critical radii: $f_3(\varepsilon) \leq \varrho(\varepsilon) \leq f_1(\varepsilon)$. We get an equation for the equilibrium radius by setting the area defect to zero. Note that the height, cap

area and area defect are

$$h_3(\varepsilon) = \varrho(\varepsilon) - f_3(\varepsilon) = \varrho(\varepsilon) - \tfrac{\sqrt{3}\varepsilon}{2}, \tag{D.39}$$

$$A_3(\varepsilon) = 2\pi\varrho(\varepsilon)h_3(\varepsilon) = 2\pi\varrho(\varepsilon)\left(\varrho(\varepsilon) - \tfrac{\sqrt{3}\varepsilon}{2}\right), \tag{D.40}$$

$$\Delta(\varepsilon) = \tfrac{4\pi\varrho^2(\varepsilon) - 4A_4(\varepsilon)}{\varepsilon} = \tfrac{4\pi\varrho(\varepsilon)[\sqrt{3}\varepsilon - \varrho(\varepsilon)]}{\varepsilon}. \tag{D.41}$$

Setting $\Delta(\varepsilon) = 0$, we get $\varrho(\varepsilon) = \sqrt{3}\varepsilon$; compare with (4.81). To get the soft density, we still need the volume of the cap, by which we mean the volume of the convex hull of the cap. Equivalently, it is the volume of the cone over the cap minus the volume of the cone of the disk spanned by the circle bounding the cap. The area of the disk is $2\pi h_3(\varepsilon)\varrho(\varepsilon) - \pi h_3^2(\varepsilon)$. The volume of the cap and the soft density are therefore

$$V_3(\varepsilon) = \tfrac{\pi[3h_3^2(\varepsilon)\varrho(\varepsilon) - h_3^3(\varepsilon)]}{3} \tag{D.42}$$

$$= \tfrac{\pi[\varepsilon\sqrt{3} - 2\varrho(\varepsilon)]^2[\varepsilon\sqrt{3} + 4\varrho(\varepsilon)]}{24}, \tag{D.43}$$

$$\delta_1(\varepsilon) = \tfrac{4\pi\varrho^3(\varepsilon) - 12V_3(\varepsilon)}{3\varepsilon} = \tfrac{3\sqrt{3}\pi\varepsilon^2}{2}; \tag{D.44}$$

compare with (4.82).

Cases II to III. Referring to Table 4.1, we note that for every $\varepsilon \in [0.239\ldots, 0.617\ldots]$ the ball with the equilibrium radius intersects the same 8 Voronoi facets. Indeed, we have $f_3(\varepsilon), f_1(\varepsilon) \leq \varrho(\varepsilon) \leq f_2(\varepsilon)$ throughout the interval. To get an equation for the equilibrium radius, we reuse the equation for A_3 and compute the height and area of the other type of cap and the area defect:

$$h_1(\varepsilon) = \varrho(\varepsilon) - f_1(\varepsilon) = \varrho(\varepsilon) - \tfrac{\sqrt{\varepsilon^2+2}}{2\sqrt{3}}, \tag{D.45}$$

$$A_1(\varepsilon) = 2\pi\varrho(\varepsilon)h_1(\varepsilon) = 2\pi\varrho(\varepsilon)\left(\varrho(\varepsilon) - \tfrac{\sqrt{\varepsilon^2+2}}{2\sqrt{3}}\right), \tag{D.46}$$

$$\Delta(\varepsilon) = \tfrac{4\pi\varrho^2(\varepsilon) - 4A_3(\varepsilon) - 12A_1(\varepsilon)}{\varepsilon} \tag{D.47}$$

$$= \tfrac{4\pi\varrho(\varepsilon)[\sqrt{3}\varepsilon - \sqrt{3\varepsilon^2+6} - 7\varrho(\varepsilon)]}{\varepsilon}. \tag{D.48}$$

Setting $\Delta(\varepsilon) = 0$ we get $\varrho(\varepsilon) = \left(\sqrt{3}\varepsilon + \sqrt{3\varepsilon^2+6}\right)/7$; compare with (4.83). As before, we continue by computing the volume of the cap and the soft density:

$$V_1(\varepsilon) = \tfrac{\pi[3h_1^2(\varepsilon)\varrho(\varepsilon) - h_1^3(\varepsilon)]}{3}$$

$$= \tfrac{\pi[-6\varrho(\varepsilon) + \sqrt{3\varepsilon^2+6}]^2[12\varrho(\varepsilon) + \sqrt{3\varepsilon^2+6}]}{648}, \tag{D.49}$$

$$\delta_1(\varepsilon) = \tfrac{4\pi\varrho^3(\varepsilon) - 12V_3(\varepsilon) - 36V_1(\varepsilon)}{3\varepsilon}$$

$$= -\tfrac{\pi[27\sqrt{3}\varepsilon(11\varepsilon^2 - 8) + (26 - 95\varepsilon^2)\sqrt{3\varepsilon^2+6}]}{882\varepsilon}; \tag{D.50}$$

compare with (4.84). The only root of the derivative is $\delta_1'(0.5) = 0$, with the second

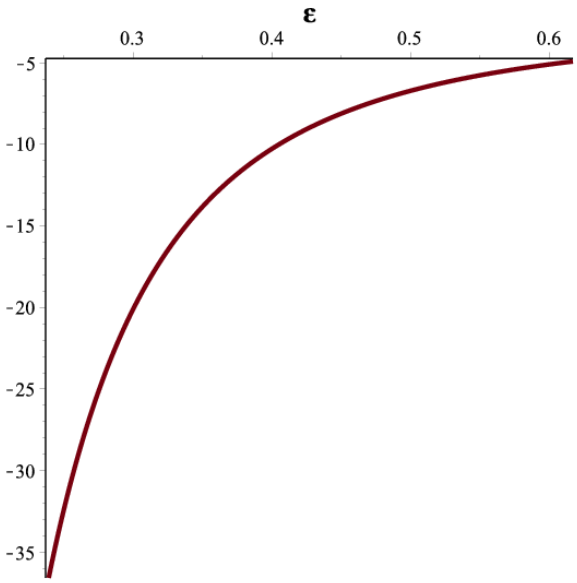

Figure D.2: The second derivative of the maximum soft density function within the interval $[0.239\ldots, 0.617\ldots]$.

derivative $\delta_1''(0.5) < 0$. We see in Figure D.2 that the second derivative is negative throughout the interval of interest, which implies that the maximum soft density is concave over $[0.239\ldots, 0.617\ldots]$; see Figure 4.15.

Cases IV to VII. Referring to Table 4.1, we note that for every $\varepsilon \in [0.617\ldots, 1.471\ldots]$ the ball with the equilibrium radius intersects the same 6 Voronoi facets: $f_1(\varepsilon) \leq \varrho(\varepsilon) \leq f_2(\varepsilon), f_3(\varepsilon), f_4(\varepsilon)$ throughout the interval. Reusing (D.46), the area defect is

$$\Delta(\varepsilon) = \tfrac{4\pi\varrho^2(\varepsilon) - 12A_1(\varepsilon)}{\varepsilon} = \tfrac{4\pi\varrho(\varepsilon)\sqrt{3\varepsilon^2+6} - 20\pi\varrho^2(\varepsilon)}{\varepsilon}. \tag{D.51}$$

Setting $\Delta(\varepsilon) = 0$, we get $\varrho(\varepsilon) = \sqrt{3\varepsilon^2 + 6}/5$; compare with (4.85). Reusing (D.49), the soft density is

$$\delta_1(\varepsilon) = \tfrac{4\pi\varrho^3(\varepsilon) - 36V_1(\varepsilon)}{3\varepsilon} = \tfrac{11\pi\sqrt{(3\varepsilon^2+6)^3}}{1350\varepsilon}; \tag{D.52}$$

compare with (4.86). The only root of the derivative is $\delta_1'(1) = 0$, with the second derivative $\delta_1''(1) > 0$. We see in Figure D.3 that the second derivative is positive throughout the interval of interest, which implies that the maximum soft density is convex over $[0.617\ldots, 1.471\ldots]$; see Figure 4.15.

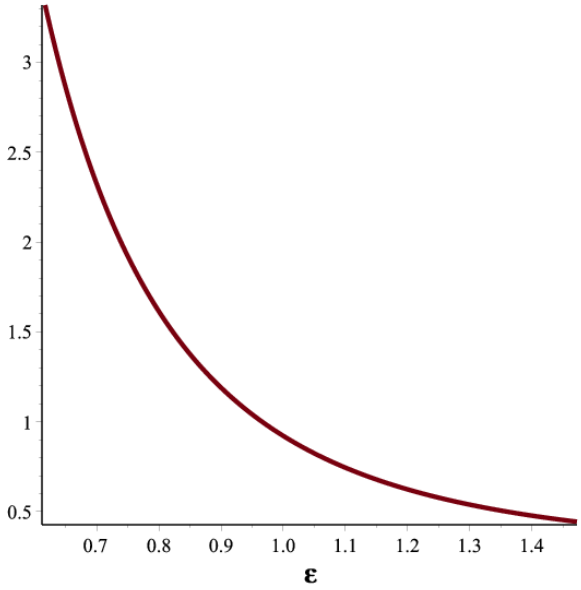

Figure D.3: The second derivative of the maximum soft density function within the interval $[0.617\ldots, 1.471\ldots]$.

Cases VIII to XI. Referring to Table 4.1, we note that for $\varepsilon \in [1.471\ldots, 2.576\ldots]$ the ball with the equilibrium radius intersects all 12 Voronoi facets: $f_1(\varepsilon), f_4(\varepsilon) \leq \varrho(\varepsilon)$. In Cases X and XI, there are overlaps among the corresponding caps, but we ignore them for the time being by considering the simplified soft density. We reuse (D.46) and compute the height and area of the remaining cap type and the area defect:

$$h_4(\varepsilon) = \varrho(\varepsilon) - f_4(\varepsilon) = \varrho(\varepsilon) - \tfrac{\sqrt{2}}{2}, \tag{D.53}$$

$$A_4(\varepsilon) = 2\pi\varrho(\varepsilon)h_4(\varepsilon) = 2\pi\varrho(\varepsilon)\left(\varrho(\varepsilon) - \tfrac{\sqrt{2}}{2}\right), \tag{D.54}$$

$$\begin{aligned}\Delta(\varepsilon) &= \tfrac{4\pi\varrho^2(\varepsilon) - 12A_1(\varepsilon) - 12A_4(\varepsilon)}{\varepsilon} \\ &= \tfrac{12\sqrt{2}\pi\varrho(\varepsilon) + 4\pi\varrho(\varepsilon)\sqrt{3\varepsilon^2+6} - 44\pi\varrho^2(\varepsilon)}{\varepsilon}.\end{aligned} \tag{D.55}$$

Setting $\Delta(\varepsilon) = 0$, we get $\varrho(\varepsilon) = \left(\sqrt{3\varepsilon^2+6} + 3\sqrt{2}\right)/11$; compare with (4.87). We continue by computing the cap volume and the simplified soft density:

$$\begin{aligned}V_4(\varepsilon) &= \tfrac{\pi(3\varrho(\varepsilon)h_4^2(\varepsilon) - h_4^3(\varepsilon))}{3} \\ &= \tfrac{\pi(\sqrt{2}-2\varrho(\varepsilon))^2(4\varrho(\varepsilon)+\sqrt{2})}{24},\end{aligned} \tag{D.56}$$

$$\begin{aligned}\delta_{1\mathrm{s}}(\varepsilon) &= \tfrac{4\pi\varrho^3(\varepsilon) - 36V_1(\varepsilon) - 36V_4(\varepsilon)}{3\varepsilon} \\ &= \tfrac{\pi[324\sqrt{2}\varepsilon^2 - 882\sqrt{2} + (478 - 85\varepsilon^2)\sqrt{3\varepsilon^2+6}]}{2178\varepsilon};\end{aligned} \tag{D.57}$$

compare with (4.88). The only root of the derivative is ${\delta_{1\mathrm{s}}}'(2) = 0$, with the second derivative ${\delta_{1\mathrm{s}}}''(2) < 0$. We see in Figure D.4 that the second derivative is negative

throughout the interval of interest, which implies that the maximum simplified soft density is concave over $[1.471\ldots, 2.576\ldots]$; see Figure 4.15. Interestingly, the second derivative does not go to 0 when ε approaches the endpoints, and we observe the same phenomenon in Figures D.2 and D.3. It follows that the second derivative of the maximum simplified soft density has discontinuities, namely at $\varepsilon = 0.239\ldots, 0.617\ldots, 1.471\ldots, 2.576\ldots$.

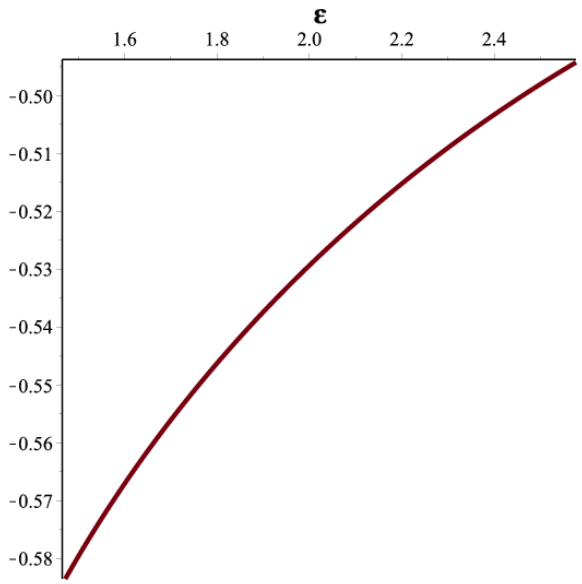

Figure D.4: The second derivative of the maximum soft density function within the interval $[1.471\ldots, 2.576\ldots]$.

Case XII. Referring to Table 4.1, we note that for $\varepsilon \in [2.576\ldots, \infty)$ the ball with the equilibrium radius intersects only 6 Voronoi facets: $f_4(\varepsilon) \leq \varrho(\varepsilon) \leq f_1(\varepsilon)$. Ignoring the overlaps among the corresponding caps, we consider the simplified soft density. Reusing (D.54), we get the area defect:

$$\Delta(\varepsilon) = \tfrac{4\pi\varrho^2(\varepsilon) - 12A_4(\varepsilon)}{\varepsilon} = \tfrac{12\sqrt{2}\pi\varrho(\varepsilon) - 20\pi\varrho^2(\varepsilon)}{\varepsilon}. \tag{D.58}$$

Setting $\Delta(\varepsilon) = 0$, we get $\varrho(\varepsilon) = 3\sqrt{2}/5$; compare with (4.89). Reusing (D.56), we get the simplified soft density:

$$\delta_{1\mathrm{s}}(\varepsilon) = \tfrac{4\pi\varrho^3(\varepsilon) - 36V_4(\varepsilon)}{3\varepsilon} = \tfrac{11\sqrt{2}\pi}{25\varepsilon}; \tag{D.59}$$

compare with (4.90).

D.4 Unsimplified Soft Density

Here we consider equilibrium configurations with triple intersections. In particular, we recompute the position of the equilibrium radius among the critical radii for the unsimplified soft density, the threshold for ε beyond which the equilibrium radius remains constant, and the constant C such that the unsimplified soft density has the form (4.94).

Position of the equilibrium radius. For $\varepsilon > 2.342\ldots$, the position of the equilibrium radius for the soft density may be different from that for the simplified soft density. The reason is that the formula for the area defect now includes a term involving triple intersections. Considering Case X, we begin the search at $e_4(\varepsilon)$, at which size the ball at the origin intersects 6 Voronoi facets at distance $f_4(\varepsilon)$, 6 Voronoi facets at distance $f_1(\varepsilon)$, and 6 Voronoi edges at distance $e_3(\varepsilon)$. Using the spherical area formula in [Edelsbrunner and Fu, 1994] as well as (D.33) and (D.34), we get

$$A_e(\varepsilon) = \tfrac{b_1(\varepsilon)+b_2(\varepsilon)}{6\varepsilon^2+3}, \tag{D.60}$$

$$\begin{aligned}\Delta(\varepsilon) &= \tfrac{4\pi e_4^2(\varepsilon)-12A_1(\varepsilon)-12A_4(\varepsilon)+12A_e(\varepsilon)}{\varepsilon} \\ &= \tfrac{2[6b_1(\varepsilon)+6b_2(\varepsilon)+\pi(\varepsilon^2+2)b_3(\varepsilon)]}{\varepsilon(6\varepsilon^2+3)}\end{aligned} \tag{D.61}$$

for the surface area of a single triple intersection and the area defect, in which

$$\begin{aligned}b_1(\varepsilon) &= (\varepsilon^2+2)^2\left(\pi - \arccos\tfrac{\varepsilon^4-8\varepsilon^2-2}{2(\varepsilon^2-1)^2}\right), \\ b_2(\varepsilon) &= -2(\varepsilon^2+2)\sqrt{6\varepsilon^2+3}\arccos\tfrac{\sqrt{2\varepsilon^2+1}}{\varepsilon^2-1}, \\ b_3(\varepsilon) &= 6\sqrt{6\varepsilon^2+3} + \sqrt{(12\varepsilon^2+6)(3\varepsilon^2+6)} - 11(\varepsilon^2+2)\end{aligned} \tag{D.62}$$

The area defect is negative for all $\varepsilon > 2.342\ldots$; see the left graph in Figure D.5. It follows that the equilibrium radius remains at the same position among the critical radii as for the simplified soft density. In Cases XI and XII, the expression for the area defect at $e_4(\varepsilon)$ is the same as above, which implies that the equilibrium radius is smaller than $e_4(\varepsilon)$. It remains to evaluate the area defect at $f_1(\varepsilon)$. Using (D.24), we get

$$A_f(\varepsilon) = c_1(\varepsilon) + c_2(\varepsilon), \tag{D.63}$$

$$\begin{aligned}\Delta(\varepsilon) &= \tfrac{4\pi f_1^2(\varepsilon)-12A_4(\varepsilon)+12A_f(\varepsilon)}{\varepsilon} \\ &= c_3(\varepsilon) + c_4(\varepsilon)\end{aligned} \tag{D.64}$$

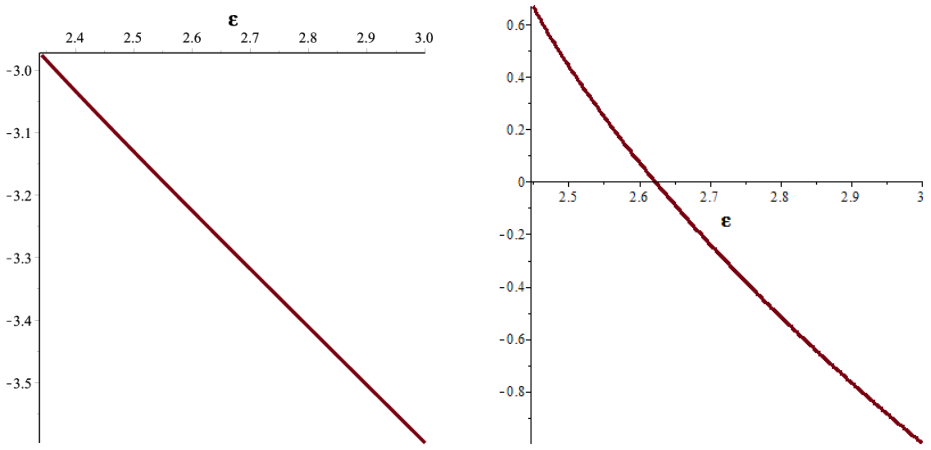

Figure D.5: Two graphs of the area defect for the soft density measure, at $e_4(\varepsilon)$ for $\varepsilon \in [2.342\ldots, 3]$ on the *left* and at $f_1(\varepsilon)$ for $\varepsilon \in [2.449\ldots, 3]$ on the *right*.

for the surface area of the triple intersection and the area defect at radius $f_1(\varepsilon)$, in which

$$\begin{aligned}
c_1(\varepsilon) &= -\tfrac{\varepsilon^2+2}{6} \arccos \tfrac{\varepsilon^2-10}{2\varepsilon^2-8}, \\
c_2(\varepsilon) &= \tfrac{2\pi+\pi\varepsilon^2}{6} - \tfrac{\sqrt{6\varepsilon^2+12}}{3} \arccos \tfrac{2}{\sqrt{2\varepsilon^2-8}}, \\
c_3(\varepsilon) &= \tfrac{2\pi+\pi\varepsilon^2}{3\varepsilon} - \tfrac{(2\varepsilon^2+4)}{\varepsilon} \arccos \tfrac{\varepsilon^2-10}{2\varepsilon^2-8}, \\
c_4(\varepsilon) &= \tfrac{2\sqrt{6\varepsilon^2+12}}{\varepsilon} \left[\pi - 2 \arccos \tfrac{2}{\sqrt{2\varepsilon^2-8}}\right].
\end{aligned}$$

As shown in Figure D.5 on the right, $\varepsilon = 2.622758110\ldots \approx 2.62$ separates positive from negative area defect. In other words, Cases XI and XII remain the same, except that the transition shifts from $2.576\ldots$ to $2.622\ldots$.

Maximum soft density. Cases X and XI corresponding to $\varepsilon \in [2.342\ldots, 2.62\ldots]$ have the same expression for the area defect. Reusing (D.46) and (D.54), we get

$$A_e(\varepsilon) = -2\varrho(\varepsilon)[d_1(\varepsilon) + d_2(\varepsilon) - \pi\varrho(\varepsilon)], \tag{D.65}$$

$$\begin{aligned}
\Delta(\varepsilon) &= \tfrac{4\pi\varrho^2(\varepsilon) - 12A_1(\varepsilon) - 12A_4(\varepsilon) + 12A_e(\varepsilon)}{\varepsilon} \\
&= \tfrac{4\varrho(\varepsilon)[-6d_1(\varepsilon) + d_3(\varepsilon) + d_4(\varepsilon) - 6d_2(\varepsilon)]}{\varepsilon},
\end{aligned} \tag{D.66}$$

for the area of the triple intersection and the area defect, in which

$$\begin{aligned}
d_1(\varepsilon) &= \sqrt{2}\arccos\tfrac{1}{\sqrt{6\varrho^2(\varepsilon)-3}},\\
d_2(\varepsilon) &= \varrho(\varepsilon)\arccos\tfrac{\varrho^2(\varepsilon)-1}{2\varrho^2(\varepsilon)-1},\\
d_3(\varepsilon) &= \pi\sqrt{3\varepsilon^2+6},\\
d_4(\varepsilon) &= 3\sqrt{2}\pi - 5\pi\varrho(\varepsilon).
\end{aligned}$$

Setting $\Delta(\varepsilon) = 0$, we do not succeed in finding a closed-form expression for $\varrho(\varepsilon)$, but we are able to sample its value at discrete parameters ε. Reusing (D.49) and (D.56), we get

$$V_e(\varepsilon) = \tfrac{[1-6\varrho^2(\varepsilon)]d_1(\varepsilon)+2d_5(\varepsilon)-4\varrho^2(\varepsilon)d_2(\varepsilon)}{6}, \tag{D.67}$$

$$\begin{aligned}
\delta_1(\varepsilon) &= \tfrac{4\pi\varrho^3(\varepsilon)-36V_1(\varepsilon)-36V_4(\varepsilon)+36V_e(\varepsilon)}{3\varepsilon}\\
&= -\tfrac{d_3(\varepsilon)d_7(\varepsilon)+d_1(\varepsilon)d_8(\varepsilon)+144\varrho^2(\varepsilon)d_2(\varepsilon)+6d_6(\varepsilon)}{18\varepsilon}
\end{aligned} \tag{D.68}$$

for the volume of a single triple intersection and the soft density, in which

$$\begin{aligned}
d_5(\varepsilon) &= \tfrac{6\pi\varrho^3(\varepsilon)+\sqrt{3\varrho^2(\varepsilon)-2}}{3},\\
d_6(\varepsilon) &= 20\pi\varrho^3(\varepsilon) + 3\sqrt{2}\pi[1-6\varrho^2(\varepsilon)] - 4\sqrt{3\varrho^2(\varepsilon)-2},\\
d_7(\varepsilon) &= \varepsilon^2 - 36\varrho^2(\varepsilon) + 2,\\
d_8(\varepsilon) &= 216\varrho^2(\varepsilon) - 36.
\end{aligned}$$

We use the ability to sample the equilibrium radius from (D.66) and plug these values into (D.68) to sketch the graph of $\delta_1(\varepsilon)$ in the interval $[2.342\ldots, 2.62\ldots]$, which falls of course between the graphs of the simplified and the extrapolated soft densities; see Figure 4.16.

Extrapolated soft density. In Case XII, the equilibrium radius is constant over the entire interval from $2.62\ldots$ to infinity. Reusing (D.54) and (D.65), we get

$$\begin{aligned}
\Delta(\varepsilon) &= \tfrac{4\pi\varrho^2(\varepsilon)-12A_4(\varepsilon)+12A_e(\varepsilon)}{\varepsilon}\\
&= \tfrac{4\varrho(\varepsilon)[\pi\varrho(\varepsilon)+3\sqrt{2}\pi-6d_1(\varepsilon)-6d_2(\varepsilon)]}{\varepsilon},
\end{aligned} \tag{D.69}$$

for the area defect. Setting $\Delta(\varepsilon) = 0$ and reusing (D.56) and (D.67), we get

$$\varrho(\varepsilon) = 0.8601773122\ldots, \tag{D.70}$$

$$\begin{aligned}\delta_1(\varepsilon) &= \tfrac{4\pi\varrho^3(\varepsilon) - 36V_4(\varepsilon) + 36V_e(\varepsilon)}{3\varepsilon} \\ &= \tfrac{[6 - 36\varrho^2(\varepsilon)]d_1(\varepsilon) - 24\varrho^2(\varepsilon)d_2(\varepsilon) + d_9(\varepsilon)}{3\varepsilon},\end{aligned} \tag{D.71}$$

in which

$$d_9(\varepsilon) = 4\sqrt{3\varrho^2(\varepsilon) - 2} + 4\pi\varrho^3(\varepsilon) + 3\sqrt{2}\pi[6\varrho^2(\varepsilon) - 1].$$

Plugging the constant equilibrium radius (D.70) into (D.71), we get $\delta_1(\varepsilon) = C/\varepsilon$, with $C = 1.962290082\ldots \approx 1.96$; see Figure 4.16. This gives $\delta_{1\mathrm{x}}(2.342\ldots) = 0.8378301951\ldots$, which is less than the soft density of the FCC lattice at equilibrium, as desired.